GEOLOGY OF LOWELL CRATER REGION ON THE MOON: ANALYSIS OF REMOTE SENSING DATA

Ph. D. THESIS

by
NEERAJ SRIVASTAVA

DEPARTMENT OF EARTH SCIENCES
INDIAN INSTITUTE OF TECHNOLOGY ROORKEE
ROORKEE-247 667 (INDIA)
APRIL, 2014

GEOLOGY OF LOWELL CRATER REGION ON THE MOON: ANALYSIS OF REMOTE SENSING DATA

A THESIS

Submitted in partial fulfilment of the requirements for the award of the degree of

DOCTOR OF PHILOSOPHY

in

APPLIED GEOLOGY

by

NEERAJ SRIVASTAVA

DEPARTMENT OF EARTH SCIENCES
INDIAN INSTITUTE OF TECHNOLOGY ROORKEE
ROORKEE-247 667 (INDIA)
APRIL, 2014

INDIAN INSTITUTE OF TECHNOLOGY ROORKEE
ROORKEE

CANDIDATE'S DECLARATION

I hereby certify that the work which is being presented in this thesis entitled "GEOLOGY OF LOWELL CRATER REGION ON THE MOON: ANALYSIS OF REMOTE SENSING DATA" in partial fulfilment of the requirements for the award of the Degree of Doctor of Philosophy and submitted in the Department of Earth Sciences of the Indian Institute of Technology Roorkee, Roorkee is an authentic record of my own work carried out during a period from July, 2010 to April, 2014 under the supervision of Dr. R. P. Gupta, Professor, Indian Institute of Technology Roorkee, Roorkee, and Dr. J. N. Goswami, Professor, Physical Research Laboratory, Ahmedabad.

The matter presented in the thesis has not been submitted by me for the award of any other degree of this or any other Institute.

(NEERAJ SRIVASTAVA)

This is to certify that the above statement made by the candidate is correct to the best of our knowledge.

(J.N. GOSWAMI)
Supervisor

(R.P. GUPTA)
Supervisor

Date: April , 2014

The Ph.D. Viva-Voce Examination of **Mr. Neeraj Srivastava**, Research Scholar, has been held on _____.

Signature of Supervisor's Signature of Chairman, SRC Signature of External Examiner

Head of the Department/Chairman, ODC

Dedicated to my late grandparents

Abstract

Study of geology of the Moon has been the centre stage of planetary science and exploration endeavors. It is the nearest celestial body to the Earth, and possibly, the Moon's existence is responsible for our own origin and survival. Further, importantly it has recorded the imprints of precious geological events the Earth would have witnessed during its geological history, traces of which are lost now due to the Earth's dynamic nature.

The Moon is imprinted with numerous meteoroid impact craters/basins (microns to several hundred kms in diameter) and dark lava plains known as mare. The impact structures expose subsurface rocks, enabling their study by robotic/manned missions or remote sensing techniques. The mare plains mostly formed between ~3-3.8 Ga, when the Moon was energetic. As the Moon cooled, intensity of volcanism reduced and only minor extrusive activities continued up to the Copernican era ~1 Ga. Interestingly, most of the mare is confined to the basins created by the mega-impact events. It is not clear whether there was any genetic relation of lunar volcanism to the impacts and the subject is debated.

The Orientale basin, located on the western limb of the Moon, is the youngest and the most well preserved mega sized multi-ring basin that formed ~3.8 Ga. The basin in only partly filled with basalts therefore it is an ideal location to simultaneously study impact cratering and volcanism and to decipher a relationship between the two, if it exists? Due to these peculiarities, the Orientale basin has been extensively studied providing a broad idea about the general geology and formation of its morphological and compositional facies. It is host to several complex impact craters that provide an opportunity to study the stratigraphic framework of the respective facie they sample. The Lowell crater (centred at ~13^{o}S, 103.4^{o}W; ~66 km in diameter) is one such post-Orientale crater that has formed in the ejecta of Orientale basin between the Outer Rook Ring (ORR) and the Cordillera ring (CR).

In this study, topographical, morphological, spectral reflectance, and crater count analysis have been carried out for the Lowell crater region on the northwestern parts of Orientale basin, which covers an area of ~198x198 km^{2}. The Lowell crater is unique since it intersects the ORR and it is the largest and the freshest post-Orientale impact crater in the

Montes Rook Formation (MRF). Therefore, its geology holds clues to the subsurface geology of the MRF. Though geologically important, this particular crater has largely remained un-explored.

High-resolution remote sensing data from state-of-the-art instruments aboard Chandrayaan-1 (2008; ISRO), Kaguya (2007; JAXA) and Lunar Reconnaissance Orbiter (2009; NASA) have been used in this study. Surface topography has been studied using Kaguya TC DTM, morphological analysis has been carried out using images from LRO (WAC and NAC), Kaguya TC and Chandrayaan – 1 M^3, and crater counting has been done on Kaguya TC images. For spectral reflectance studies global mode Level 2 M^3 data have been used.

Surface morphological analysis has revealed that the Lowell crater region is extremely undulating with a relief of ~9.5 km. The highest location lies in the Cordillera scarp (~6 km high) and the deepest areas lie inside the Lowell crater which is ~3-3.5 km deep. Several prominent lineaments possibly related to the formation of the Orientale basin and/or the lunar grid is present in the area. The Lowell crater located amidst uplands is polygonal in shape and it shows N-S asymmetric ejecta distribution. Most of the proximal ejecta are emplaced in the northern side and the exterior impact melt pools are concentrated in the northwestern side.

The terraced crater walls on the western side are broader compared to the walls on the eastern side and they show rhombic cross-sections due to cross-cutting of the terraces with pre-existing lineaments. Also, they show comparatively gentle slopes and are largely topographically high compared to the western walls. The central peak is ~1.5 km high (from the crater floor) and it shows melt pond at around the summit, boulders at several places, and prominent slumping and subsidence on the eastern side. Numerous floor irregularities are present on the crater floor, the density being higher on the eastern side.

A small (~9 km in diameter) superposed asymmetric rayed crater (referred to as Crater S in the study) is present near to the eastern side rim of the Lowell crater. A pronounced rectilinear resurfacing is also present on the eastern side, which is ~ 3-6 km wide and extends to ~17 km from the floor of Crater S, terminating approximately half way to the central peak of the Lowell crater. The resurfacing show conspicuous scarcity of

impact craters and exhibits multiple generations of fresh viscous flows confined to a possible graben. A few potential volcanic source regions have been identified in the resurfacing suggesting that the unit could have formed due to volcanism during recent times (?). These fresh flows have superposed parts of comparatively older impact melt flows diverging from the Crater S and descending down the walls of Lowell crater.

Spectral diversity in the Lowell crater region has been worked out using representative average spectral reflectance curves, popularly used FCC's (based on integrated band depth and band ratios), and a Minimum Noise Function (MNF) based color coding. The MNF based FCC effectively captured the spectral variability in the Lowell crater region. The areas surrounding Lowell crater, which are the best approximates for the surface lithology of the Lowell target, largely show presence of massifs of un-shocked anorthosites, shocked anorthosites, Mg-spinel anorthoisites, basalts (of Lacus Veris), and mature soils.

The Lowell crater wall is largely composed of norite to anorthositic norite with intermittent anorthosite and Mg-spinel rich areas. The floor of the Lowell crater is largely occupied with gabbroic/basaltic melts and the floor irregularities also show conspicuous clinopyroxene signatures. A part of the proximal ejecta, which is nearest to the Lowell crater in the northwestern and northeastern quadrants also show presence of clinopyroxene. The central peak shows distinct compositional asymmetry. The rocks on the western side of the peak shows gabbroic/basaltic signature, whereas the ones on the eastern side (mostly coinciding with the slumped zone) are largely Mg-rich (low-Ca pyroxene and Mg-spinel bearing rocks).

Anomalous spectral signatures showing prominent curved inflexion ~1.25 µm (along with prominent 1 µm and 2 µm absorption feature) have been noticed at several spots on the central peak and at certain sites in the walls. Most of these correspond with the areas showing presence of boulders and could relate to presence of Mg-spinel troctolites or co-association of pyroxene and un-shocked anorthosite, or the 1.25 µm could be due to Fe^{+2} at the M1 site of pyroxene.

These observations indicate that the Lowell impact event would have excavated a deep seated pre-existing mafic pluton in addition to the Orientale basin ejecta and pre-existing megaregolith layer of anorthositic to anorthositic norite composition. The pluton would have been emplaced in the megaregolith layer prior to or after the formation of the Orientale basin at a depth of ~6.6 km (or less). The Mg-spinels observed in the central peak would have formed due to melt wall rock reaction in the area of the emplacement of the pluton. Also, Mg-spinel anorthosite exposures have been spotted in other non-mare units of the Orientale; however, a distinct scarcity exists in the IRR, which is supposed to have exhumed rocks from deeper levels in the Orientale region. In most of the observed occurrences in the Orientale basin, pyroxenes (mostly noritic rocks) are present in the adjacent areas. The rock association in the IRR is unshocked plagioclase.

The composition of the recently produced resurfacing is distinctively gabbroic/basaltic. However, the older flows (i.e. the impact melts from Crater S) largely show noritic signatures consistent with the composition of the wall of Crater S, emphasizing further that all these flows may not be co-genetic and that the fresh gabbroic/basaltic flows could have an alternate origin possibly volcanic (?). Few signatures of pyroclasts have also been noticed in the area supporting the volcanic preposition.

Crater count analysis for selected areas of the Lowell crater region has been performed to resolve the age controversy for Lowell crater (i.e. Imbrian vs Copernican), and to assign a time frame for the formation of the recent resurfacing. It has been estimated that the Lowell crater formed ~374 Ma ago; therefore, it is Copernican in age. Further, count of (plausible) impact craters on the youngest lobes of the resurfacing has indicated that they could be barely ~2-10 Ma old.

Finally, the inferences from these studies have been synthesized to assess geological evolution of the Lowell crater region. The highlights of the evolutionary stages include formation of the Lowell crater due to an oblique impact (~30^{o}-45^{o}) from S-SW direction ~374 Ma ago, excavation of a mafic pluton that possibly stalled in the megaregolith beneath the Orientale ejecta, formation of a rayed superposed crater, and apparent indications that the region would have experienced possibly volcanic activity (?) during recent times.

ACKNOWLEDGEMENT

As my thesis approaches completion, I realize that it has much deeper implication than just being a hard bound manuscript. Each chapter of this manuscript embodies the toil, brain storming sessions, persistent effort and emotional turmoil that was involved during its development. The thesis encloses the contribution of people who played significant roles as bookmarks during various stage of its completion. Hence I would like to take this opportunity of acknowledging each one of them and thank them for being there at all the right junctures.

First and foremost I would like to extend my sincere regards to my supervisors whom I have kept in high regards.

I am profoundly obliged to my supervisor Prof. R. P. Gupta, Earth Science Department; IITR who apart from being an adoring guide had also been a mentor who steered me to improvise and evolve consistently during my research period. He is a great teacher, educator and advisor.

I extend my gratitude towards Prof. J.N. Goswami, Director PRL, and my supervisor, who has inspired and motivated me from time to time. His guidance and suggestions will surely act as milestone in my life. Also, Prof. Goswami is greatly acknowledged for permitting me to join Indian Institute of Technology, Roorkee for Ph. D. work.

The committee members Prof. G.J. Chakrapani, Dr. R.K. Goel and Prof A.K. Sen are earnestly acknowledged for sparing their valuable time in monitoring the work progress and providing useful tips, critical comments and precious suggestions from time to time. My heart-felt thanks to Prof. A. K. Sen for also kindly agreeing to be my caretaker supervisor.

Prof. A. K. Saraf (Head, Department of Earth Sciences and my ex-committee chair) is gratefully acknowledged for providing me the research facilities and useful suggestions. Prof. S.V.S. Murty, Co-ordinator PLANEX, PRL is gratefully thanked for providing me all the help and support.

I endow special thanks to Prof. Utpal Sarkar, the ex-Academic committee chairman, PRL, who supported me immensely whenever required. My sincere thanks to Prof. A. K. Singhvi (The ex-Dean, PRL) and Mr. Yogendra Trivedi (Registrar, PRL) for providing all the administrative support from PRL.

I would like to gratefully acknowledge Prof. Narendra Bhandari, who introduced me to the intricacies of Planetary Sciences. Prof. R. Ramesh and other colleagues at PRL are gratefully accredited for sparing their precious time in taking classes during the course work.

My sincere gratitude to Dr. Pitambar Pati, Varinder, Reet, Rohan and Ashwani from IIT Roorkee and Indhu, Rishi, Vijayan, Durga and Amit from PRL. Thanks friends for being there with me and for chipping in wherever and whenever required. Special thanks to Gupta Madam who was always present with her motherly affection and unforgettable delicious meals that I savored with my colleagues.

I am also thankful to my PLANEX Newsletter team, who shared my responsibilities so that I could carry on my research work uninterruptedly. Special thanks Mr. K.R. Nambiar, Pauline Madam and Mr. Sudheen for their prompt help and support.

Last but not at all the least are my family members, my parents, my wife, my in-laws, my brother Chanchal, his wife Shweta and my nephew Chitransh. Garima, you were always behind me during all the stressful periods, took the entire burden and always encouraged me. Without your help and co-operation I would never have reached this mile-stone.

Blessings of my elders and well wishes of those younger to me have kept me going on this arduous journey of thesis completion. I am thankful to each one of you for being my strong support system.

Finally, I pay my obeisance to the almighty that conferred me with the capability, resources and people to carry on my work successfully. His blessings paved my way at every hitch and glitch during the journey of my research.

NEERAJ SRIVASTAVA

Contents

LIST OF FIGURES

LIST OF TABLES

LIST OF PUBLICATIONS

Publications in refereed journals

1. **N. Srivastava**, D. Kumar, R. P. Gupta, "Young viscous flows in the Lowell crater of Orientale basin, Moon: Impact melts or volcanic eruptions?" *Planetary and Space Science*, 87, 37-45, 2013.

2. R. P. Gupta, R. K. Tiwari, V. Saini, **N. Srivastava**, "A simplified approach for interpreting Principal Component Images", *Advances in Remote Sensing*, 2, 111 – 119, 2013.

3. P. Chauhan, P. Kaur**, N. Srivastava**, S. Bhattacharya, Ajai, A.S. Kiran Kumar and J.N. Goswami, "Compositional and Morphological analysis of high resolution remote sensing data over central peak of Tycho crater on the Moon: Implications for understanding lunar interior", *Current Science*, 102, 7, 1041- 1046, 2012.

4. **N. Srivastava**, "Titanium Estimates of the Central Peaks of Lunar Craters: Implications for Sub-surface Lithology of Moon", *Advances in Space Research*, 42/2, 281-284, 2008.

Extended Abstracts in International Conferences

1. **N. Srivastava** and R. P. Gupta, "Spatial distribution of spinel in the orientale basin: new insights from M3 Data", 44th *Lunar & Planetary Science Conf.*, Houston, 1509.pdf, 2013.

2. **N. Srivastava** and R. P. Gupta, "Compositional diversity inside Lowell crater, Orientale Basin: Evidences for extensive spinel rich deposits", *2nd Conf. on Lunar Highland Crust*, 9016.pdf, 2012.

Chapter 1

Introduction

1.1 Rationale for planetary sciences and exploration

Planetary science is the study of the origin, evolution, and current environments of planetary bodies, whether they orbit around the sun, as in our solar system, or around other stars (Hartmann, 1999). The primary goal of planetary studies through remote sensing observations (e.g. Pieters, 1986; Basilevsky, 1993; Reddy et al., 2011; Chauhan, et al., 2012), theoretical simulations (e.g. Sahijpal et al., 2007), and laboratory studies of samples (e.g. Taylor, 1975; Goswami, 1998; Montmerle et al., 2006; Parthasarathy et al., 2008; Chandra and Parthasarathy, 2009) is to determine the physical characteristics of various planetary objects (planets, dwarf planets, satellites, and small solar system bodies) and to

map their surfaces for topography, morphology, and composition. Information thus acquired, helps us to comprehend the mechanism and processes responsible for the origin and evolution of these distant extra-terrestrial bodies. This helps in understanding the development of our solar system.

The present day understanding is that solar system formed as a consequence of the collapse of a rotating molecular cloud of dust and gas. While the central mass gravitated and formed sun, the gas and dust surrounding it condensed to form grains that formed the proto-planetary disk, the solar nebula. These grains, through a series of processes, aggregated to form planetesimals (~<1 mm – 1000 km objects) and finally to various planetary bodies (e.g. Lynden-Bell and Pringle, 1974; Hartmann, 1999).

Chondrules, the circular grains in the meteorites are understood to be the building entities of planetary bodies and, calcium and aluminum rich inclusions within them are largely considered to be the first formed solids in the solar system. The chronology of the early solar system is deciphered based on the systematic of the extinct radionuclides or short-lived radionuclides such as ^{26}Al, ^{41}Ca, ^{60}Fe, ^{129}I, ^{36}Cl etc, which were present in the early solar system (e.g. Jeffery and Reynolds, 1961; Murty et al., 1997; Goswami, 1998; Sahijpal et al., 1998; Sahijpal et al., 2007; Sahijpal and Gupta, 2009; Montmerle et al., 2006).

Existing astronomical and compositional evidences from studies of lunar samples (Apollo and Luna missions), meteorites (from the Moon, Mars and asteroids) and, remote sensing observations suggest that the planetary bodies are heterogeneous and they possess extreme compositional and morphological diversity. The internal energy of a planetary body, which is a function of its size, is mostly responsible for the differences in the degree of differentiation an individual has undergone (e.g. Hartmann, 1999; Gupta and Sahijpal, 2010), leading to these variations. Large planets like the Earth and Venus are still evolving; whereas, the small asteroids have barely evolved after their formation and are considered primitive. The Earth's Moon represents an intermediate stage, thus serving as an important link between the two.

The wide variety of planetary bodies in our solar system is therefore reminiscent of the various stages of evolution that the solar system has undergone and detailed understanding about each of these would be valuable. Knowledge about factors governing their crustal structure and the evolutionary conditions may help us in exploiting our own environment in a better way and also to explore possibilities for human settlement elsewhere (Hartmann, 1999).

1.2 Motivation for studying the Moon

The Moon, our nearest celestial neighbor and the only natural satellite of the Earth, for centuries has instigated all the emotional gestures in human beings. Some looked at it with awe and worshipped it. For some, its beauty evoked romanticism, still others wrote verses on it. There were a curious few who observed its motion and phases, relating them with certain periodicity of the Earth. As a result, ancient lunar calendars were developed. Several activities like eclipses and tides were also ascertained with the revolution of the Moon around the Earth. The inquisitive nature of man has thus turned his steps towards understanding the Moon slowly and steadily. He has evolved from designing lunar calendars to setting step on the Moon.

Our knowledge about lunar geology prior to mid-nineties was mainly based on a) the Earth based observations (e.g. Hartmann and Kuiper, 1962; McCord et al., 1981; Pieters et al., 1986), b) studies of the samples brought back from Apollo and Luna missions (e.g. Wood et al., 1970; Levinson and Taylor, 1971; Taylor, 1975, 1982), and c) interpretations of data from several orbiters and robotic missions (e.g. Casella, 1976; Schultz, 1976; Scott et al., 1977; Basilevsky and Head, 1995; Greeley et al., 1993; Head et al., 1993; McEwen et al., 1993).

These studies provided a broad understanding of the surface features and compositional make-up of the Moon that led to a preliminary understanding for its formation and evolution (e.g Taylor, 1994**).** The Moon possibly formed via a giant impact on to the proto-Earth ~4.6 Ga (e.g. Hartmann and Davis, 1975; Cameron and Ward, 1976; Hartmann et al., 1986) and evolved through emergence of a global magma ocean (e.g.

Warren, 1985, 1990; Elkins-Tanton et al.,2011)**,** major surface modifications during cataclysmic phase ~3.9 Ga (Tera et al., 1974; Turner and Cadogan, 1975; Morbidelli et al., 2001; Koeberl, 2006), and a pre-dominant volcanic phase thereafter (e.g. Head and Wilson, 1992; Spudis, 1999; Ziethe et al., 2009). One of the major assertions from these studies was that the Moon comprises of broadly two types of terrains – the highlands, which are mostly made of anorthositic rocks and mare, which refer to dark low lying basaltic plains of varying composition.

The Clementine mission - 1994 (Nozette et al., 1994) and Lunar Prospector - 1998 (Binder, 1998) provided the first global picture of the Moon. The Clementine mission provided mineralogical information (and also limited elemental information - Fe and Ti concentrations only) at a spatial resolution of ~100-200 m from UVVISNIR multi-spectral imaging (e.g. Lucey et al., 1998; Tompkins and Pieters, 1999; Pieters et al., 2001; Lucey, 2004). The Lunar prospector provided global elemental maps of the Moon at coarse spatial resolution of ~150 km through γ-ray spectroscopy (Lawrence et al., 1998).

The findings from these missions were largely consistent with the earlier feel of the Moon. However, several surprises were met, especially from the far side, which was largely un-explored due to scarcity of data. Some of these findings include: largely feldspathic composition of the far-side, concentration of most of the radioactive regions on the near-side, and uniquely characterized gigantic South Pole Aitken Basin (SPAB), which is one of the largest and possibly the deepest basin in our solar system. These observations led to further sub-division of the lunar crustal terranes into four distinct geochemical provinces comprising of Feldspathic Highland Terrane (FHT), Procellarum KREEP Terrane (PKT), Mare Basalt (MB), and South Pole Aitken Terrane (SPAT) (Jolliff et al., 2000; Robinson and Riner, 2005).

Thus, the findings from Clementine and Lunar Prospector clearly pointed out that the Moon was not as homogeneous as considered earlier and they also enhanced the appetite to explore it further. As a result, a string of remote sensing missions equipped with state-of-the-art instruments (from various space agencies – ESA, JAXA, CNSA, ISRO, and NASA) were sent to the Moon during recent times commencing from the year 2004. High

quality diverse datasets have been derived from these missions that have provided an opportunity to explore the Moon at resolutions of about ~0.5 m (LROC-NAC) (Robinson et al., 2010) and in several spectral ranges (e.g. NASAs Moon Mineral Mapper - M^3 aboard Chandrayaan-1) (Pieters et al., 2009a; Goswami and Annadurai, 2009).

1.3 General Characteristics of the Moon

The various physical properties of the Moon and composition of its atmosphere are summarized in Heiken et al. (1991) and Lodders and Fegley, (1998). The orbit of the Moon is nearly circular (eccentricity ~0.055) with a mean separation from the Earth of ~384,000 km. The Moon differs from most of the satellites of other planets in that its orbit is close to the plane of the ecliptic instead of the planets equatorial plane. The lunar orbital plane is inclined to the ecliptic by ~5.145°; whereas, the Moon's spin axis is inclined by only 1.5°.

With a mean orbital velocity of ~1.023 km/s, the Moon completes its orbit around the Earth in ~27.3 days. The Moon appears to go through a complete set of phases as viewed from the Earth because of its motion around the Earth. As a consequence of tidal coupling between the Earth and the Moon, the Moon's rotational period of ~27.3 days exactly coincides with its period for revolution. Due to this, the Moon always keeps essentially same face toward the Earth. Also, the Moon is receding from the Earth at a rate of ~3.8 cm/year (Nordgren, 2010**)**. A few selected physical characteristics of the Moon are tabulated in Table 1.1.

Lunar atmosphere refers to the elevated presence of atomic and molecular particles in the vicinity of the Moon compared to the interplanetary medium. It is negligible in comparison with gaseous envelope surrounding the Earth and most planets of our solar system. Earth based spectroscopic methods, Lunar prospector mission and in-situ studies during Apollo missions have revealed presence of H, He, Li, O, Na, Ar, K, Ca, and Ti in the lunar atmosphere..

More recently, measurements from Moon Impact Probe (MIP) during Chandrayaan-1 mission have revealed that the lunar atmosphere has an atmospheric

pressure of ~$6.7x10^{-5}$ Pa which is at least two orders of magnitude denser than expected (Sridharan et al., 2010a). Further, MIP deciphered presence of H_2O (and also possibly CO_2) in the lunar atmosphere during its descent to the surface of the Moon (Sridharan et al., 2010b). The possible sources of the lunar atmosphere are out gassing due to radioactive decay within the crust and sputtering due to bombardment of the lunar surface by micrometeorites and the solar wind**.**

Table 1.1: Selected physical characteristics of the Moon from (Lodders and Fegley, 1998; Heiken et al., 1991).

Property	Value
Mean radius	1737.103±0.015 km
Mean equatorial radius	1738.139±0.065 km
Mean polar radius	1735.972±0.200 km
Surface area	3.792×10^8 km^2
Volume	2.196×10^{10} km^3
Mass	7.349×10^{22} kg
Bulk density	3.344 g/cc
Gravity	1.622 m/s^2 i.e. $1/6^{th}$ of the Earth
Escape velocity	2.376 km/s
Moment of inertia	0.394
Surface temperature (min, max)	120 K, 390 K
Black body temperature	277 K
Heat Flow	22-31 Mw/m^2

1.4 Scope of the thesis

The surface of the Moon is studded with impact craters of varying shapes and dimensions. Among them, the most spectacular ones are the large sized (> ~15 km diameter) complex impact craters (Melosh, 1989; Melosh and Ivanov, 1999) which possess central peaks, terraced crater walls and flat floor. The even larger ones (> ~300 km in

diameter) possess multiple concentric rings and are therefore termed as multi-ring basins (e.g. Wood, 1978; Melosh and Mckinnon, 1978; Spudis, 1993). Impact cratering is the principal geological process that has carved and modified the Moon's surface since its formation; therefore, the resulting impact craters/basins serve as important chrono-stratigraphic units (e.g. Shoemaker, 1962; Shoemaker and Hackmann, 1962; Stöffler et al., 2006). Further, the impact structures expose subsurface rock formations therefore they provide an opportunity to study the subsurface geology of an area through manned/robotic efforts or through remote sensing (e.g. Senft and Stewart, 2007).

The other fascinating areas on the Moon are smooth and dark volcanic plains, which are popularly known as mare basalts (e.g Spudis, 1999). Most of the mare basalts are also confined to the basins and craters, therefore it is quite possible that they would have played a key role in the lunar volcanism. Thus, geological investigation of lunar craters is important to decipher the geological history of an area on the Moon.

In this study, datasets from recent missions Chandrayaan-1 (ISRO), LRO (NASA), and Kaguya (JAXA) have been used to investigate geology of the Lowell crater region, a ~198 x 198 km^2 area on the far side of the Moon enclosing ~66 km diameter Lowell crater (13.00^{o}S; 103.40^{o}W) around its centre. The region is geologically important since it is located in the Orientale basin, the proto-type multi-ring basin on the Moon. Surface topography, morphology, spectral reflectance, and crater chronology have been the main aspects of the study.

Chapter 2

Geology of the Moon – a review

2.1 Morphology

The surface of the Moon displays several circular features, which formed from time to time due to hypervelocity impacts (~15-45 km/sec) of meteoroids of varying dimensions (micron to several kms). These are the manifestations of impact cratering, a fundamental geological process, which has played a key role in the formation and evolution of each of our solar system bodies including the Earth (e.g. Melosh, 1989; Grieve, 2005; Pati and Reimold, 2007; Osinski et al., 2011). On the Moon, the meteoritic impacts are responsible for producing present day relief variations, the maximum altitude difference being ~19.87 km between the highest (~10.77 km) and the lowest (~9.10 km) points with reference to a sphere datum of radius 1737.4 km (Jaumann et al., 2012). They have produced conspicuous morphological features on the Moon such as circular craters with size dependent morphologies and tectonic features of regional dimensions.

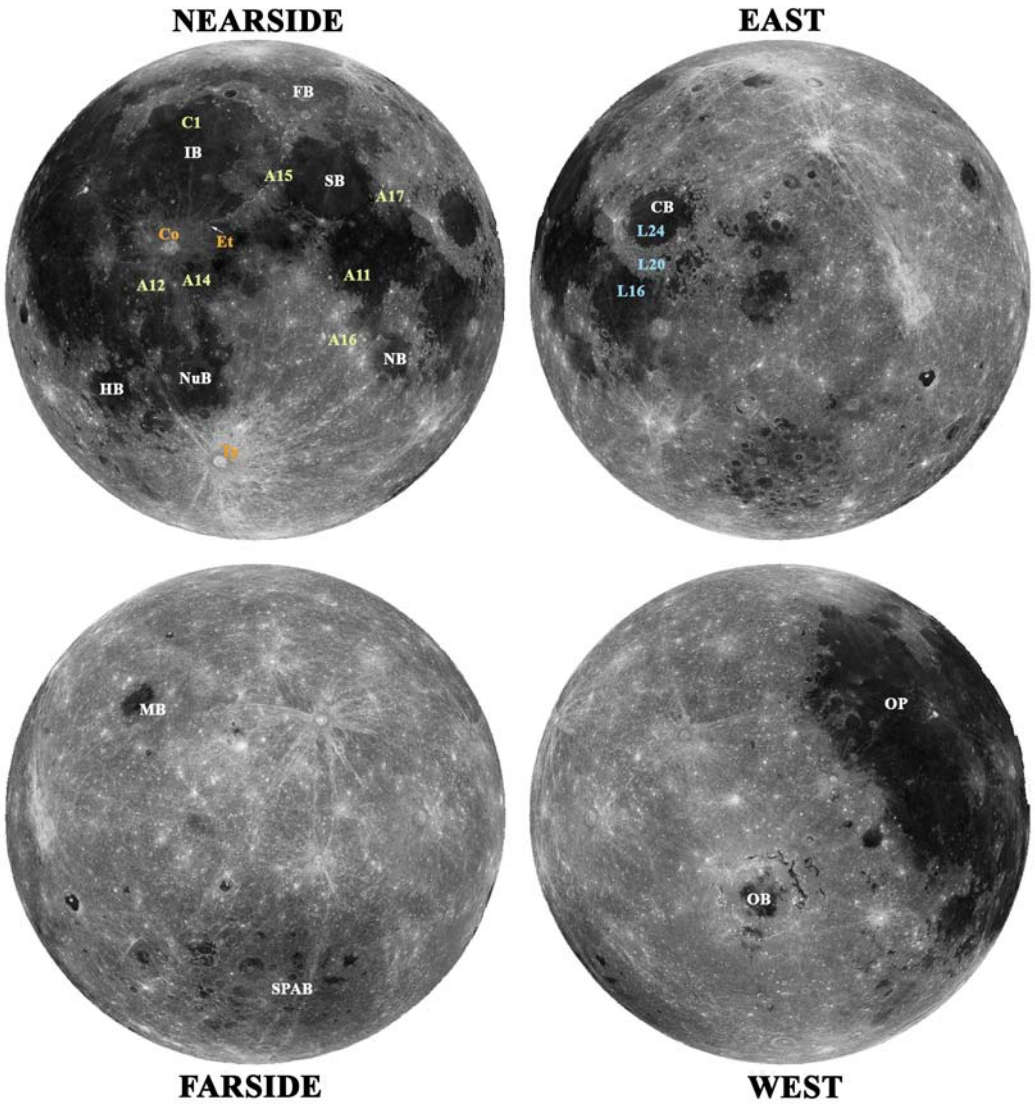

Figure 2.1 LROC WAC image mosaics showing nearside, farside, East and West faces of the Moo. Bright and heavily cratered regions are called highlands and the dark basaltic plains are termed as mare. Important craters, basins and specific landing sites are marked. Here OP: Oceanus Procellarum; IB: Imbrium basin; SB: Serenitatis basin; NB: Nectaris basin; HB: Humorum basin; NuB: Nubium basin; FB: Frigoris basin; CB: Crisium basin; Co: Copernicus crater; Ty: Tycho crater; Et: Eratosthenes crater; OB: Orientale basin; MB: Moscoviense basin; SPAB: South Pole Aitken basin; A11-17 (except 13): Apollo manned landing sites; L16, L20, L24: Luna robotic sample return sites; C1: Chang'e-3 landing site [source of base images: lroc.sese.asu.edu]

Broadly, there are two types of landforms on the Moon (Fig. 2.1). The light coloured and heavily cratered areas that are termed as “highlands” and the relatively smooth dark basaltic plains that formed due to volcanic outpouring of lavas, known as “Mare”. Global mare coverage is ~17% of lunar surface (~1% of crustal volume) but strikingly, most of the mare basalts are found on the near-side of the Moon possibly due to thicker far-side crust (e.g. Wieczorek et al., 2006; Jaumann et al., 2012). Thus, it is apparent from the physiography that hypervelocity meteoroid impacts and volcanism are the two fundamental geological processes that have modified and carved the lunar surface during its geologic history.

2.1.1 Impact craters

The impact craters are important in lunar geology since they expose subsurface rocks, thus providing us an opportunity to study the stratigraphy of an area through in-situ studies or remote sensing observations. Impact craters on the Moon vary from micron sized pits spotted in lunar glasses to a maximum of ~2500 km diameter South Pole Aitken (SPA) region, a gigantic impact structure on the south pole of the Moon (e.g. Taylor and McLennan, 2009). Broadly, impact craters are classified as simple and complex craters based on their morphology and morphometry, which is to a large extent size dependent (Fig. 2.2) (e.g. Melosh, 1989; Grieve, 2005; Melosh and Ivanov, 1999; Osinski et al., 2011; Jaumann et al., 2012).

Simple craters are smooth bowl shaped craters of diameter < ~15 km (for the Moon) with depth-to-diameter ratio of about ~1:5 (Melosh and Ivanov, 1999). A thin impact melt lining is normally present on the floor of the simple crater and rarely impact melts are present in the exterior regions. Only limited wall failure zones are present, and these are normally associated with floor irregularities (hummocks) and the rock fragments emplaced after the solidification of melts on the crater floor. With increase in size i.e. at diameter > ~15 km for the Moon, the shape and geometry of the craters gradually change (Melosh and Ivanov, 1999). A complex structure results due to downward and inward collapse of the initially steep crater walls.

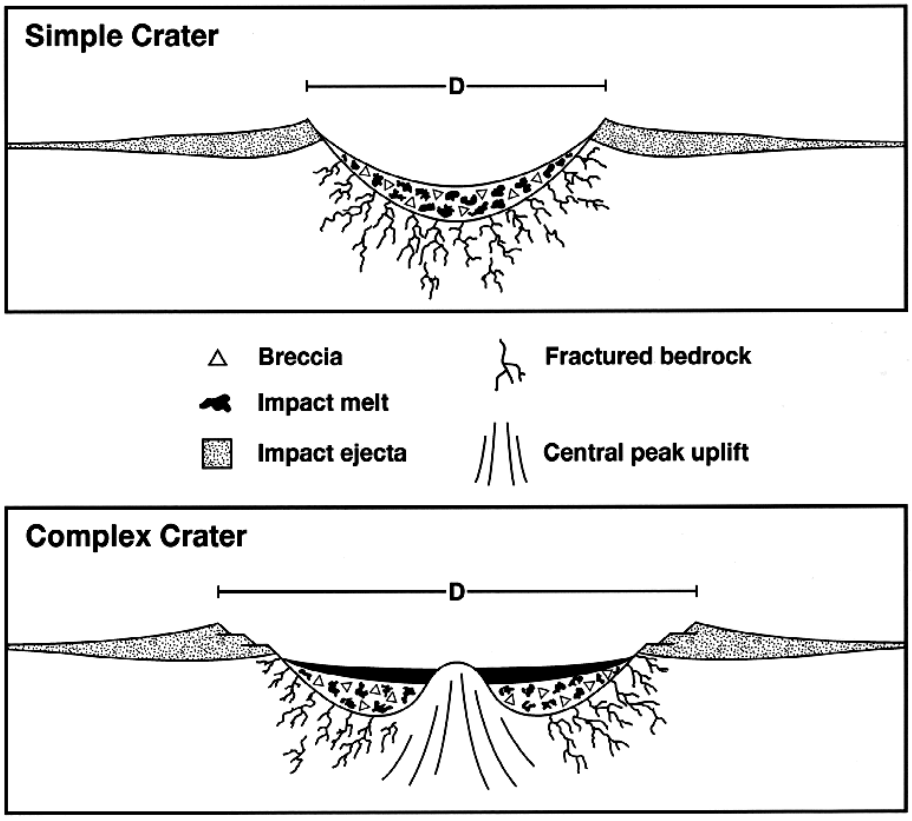

Figure 2.2 A schematic cross-sectional view of simple (top) and complex (bottom) craters showing morphological differences. Here D is the rim – rim diameter of the crater. [Source: spaceguard.rm.iasf.cnr.it]

Characteristic features of complex craters include central peak/cluster of peaks, terraced walls, widespread hummocks or floor irregularities, impact melt sheets on a large and relatively flat crater floor, and well developed continuous and intermittent ejecta blanket. This transition from simple to complex crater is gravity dependent; therefore, in case of the Earth even a ~2 km sized Dhala impact structure in the Bundelkhand region of India shows complex morphology (Pati et al., 2008, 2010). The depth to diameter ratio is ~1:10 - 1:20 for complex lunar craters, which compared to simple craters, is low. In a complex crater, the exposures of deepest rocks are found in the central peaks (e.g.,

Tompkins and Pieters, 1999; Srivastava, 2008). At diameters > ~100 km, the central peak transforms to a peak ring.

At ~300-350 km diameter, impact craters on the Moon transform to multi-ring basins, which are the largest impact related entities on the Moon and they appear to dominate its tectonic and stratigraphic framework (e.g. Hartmann and Kuiper, 1962; Melosh, 1989; Melosh and Mckinnon, 1978). A number of well established multi-ring basins occur on the Moon including the largest South Pole Aitken basin (SPAB), which is an extraordinarily large multi-ring basin (~2500 km in diameter) and a host to several probable multi-ring basins (e.g. Pieters et al., 2001). They also occur on the Earth as well as on other solar system bodies such as Callisto, Ganymede, Mercury, and Mars etc. Chicxulub impact structure (~100 km in diameter; Mexico), which is largely held responsible for the extinction of dinosaurs on the Earth, exhibits morphology of a multi-ring basin (Morgan et al., 1997).

All of these basins on the Moon are older than ~3.8 Ga and they possibly formed during Lunar cataclysm (also discussed in sections 1.2, 2.5.2 and 7.2), a period ~3.9 Ga when there was a sudden increase in the flux of impactors (Tera et al., 1974; Turner and Cadogan, 1975; Morbidelli et al., 2001; Koeberl, 2006). A plug of dense material generally underlies the centre of the basins resulting in excess gravitational pull. These are referred as MASCONS and are understood to have been formed due to melting and crustal adjustments during large impact events (Melosh et al., 2013).

2.1.2 Volcanic Features

The major volcanic features on the Moon are flood lava plains (e.g. Head, 1976; Head and Wilson, 1992; Basilevsky and Head, 1995; Spudis, 1999) that are analogous to the continental flood basalts on the Earth. These are formed from large volumes of low viscosity basaltic magma that erupted from fissures and extended as sheets resulting into flood type mare lava plains. Since most of the lunar mare basalts are also confined to the impact structures, such as Imbrium basin, Serenitatis basin, Orientale basin etc., it is likely that the impact events would have initiated and/or assisted volcanic activity on the Moon.

The other major volcanic features associated with these plains are the large sized (up to ~ hundreds of kilometre spatial extent and thousands of metre high) basaltic shields such as Cauchy (summit at 8^{o}N, 35^{o}E) and Marius Hills (summit at 14^{o}N, 52^{o}W) etc., (Spudis et al., 2013). These are host to cluster of small shields and domes (diameter ~2-10 km), rilles (long and narrow sinuous/arcuate/straight depressions that resemble lava channels) and pyroclastic deposits of varying dimensions.

Few silicic domes are also present on the Moon such as in the Gruithensen, Aristarchus, and Hansteen Alpha region on the near-side and Compton-Belkovich region on the far-side. These are steeper than the basaltic domes; have higher albedo and typically form by eruption and accumulation of highly viscous silica-rich lava from localized vents (e.g. Glotch et al., 2011; Jolliff et al., 2011).

The Moon also perhaps occasionally releases gasses from its interior due to radioactivity and volcanism (Hodges et al., 1973; Crotts et al., 2007; Crotts, 2008, 2012). A distinct surface feature which possibly formed as a result of voluminous gas release during recent times is the 2 km wide 'D' shaped Ina structure in Lacus Felicitatis on the near-side of the Moon (Schultz et al., 2006). However, the age and origin of this enigmatic feature on the Moon is still debated (Gary et al., 2012).

2.1.3 Tectonic features

Tectonics on the Moon have been primarily accredited to tidal forces, impact-induced stress, stress induced by the load of basalts within basins and thermal effects (e.g. Fielder, 1961; Strom, 1964; Casella, 1976; Melosh, 2011; Basilevsky, 1994; Hiesinger and Head, 2006; Jaumann et al., 2012). Unlike the Earth, where active tectonics is prevalent due to its large size and therefore high internal energy, the Moon has experienced only limited tectonism since its formation. Plate tectonics possibly never occurred on the Moon; however, photo-geologic investigations of the lunar surface have revealed formation of global lunar grid on the Moon just after the formation of the crust, due to compressive stresses and radial/concentric grabens that were produced locally due to colossal basin forming impacts and the load of mare basalts that filled in later.

The other major population of tectonic features is the globally present small-scale lobate scarps, which are low angle thrust faults. These are surface expressions of global cooling and shrinking of the Moon. Few of these thrust faults have been found to cut across small Copernican impact craters indicating that the Moon would have shrunk recently and that its interior might still be molten (e.g. Schultz, 1976; Binder, 1982; Watters et al., 2010).

2.2 Composition

The knowledge about composition of the Moon has been mainly derived from laboratory study of lunar samples brought back from Apollo and Luna missions and the lunar meteorites from unknown provenances of the Moon, that have occasionally reached the Earth. The Apollo and Luna samples also served as ground truth to aid in derivation of global compositional information from remote sensing missions such as Lunar Prospector, Clementine, Chandrayaan-1, Kaguya and Lunar Reconnaissance Orbiter (LRO).

Remote sensing techniques such as reflectance spectroscopy (e.g. Pieters and Englert, 1993; Lucey et al., 1998, 2000; Pieters et al., 2001), thermal emissivity measurements (e.g. Donaldson Hanna et al., 2011) and gamma ray spectroscopy (e.g. Lawrence et al., 1998; Gillis et al., 2004) have been used to derive information about the composition of the Moon. Further, based on the geomorphology and rock compositions, Jolliff et al. (2000) have broadly classified lunar surface into Procellarun KREEP Terrane (PKT), Feldspathic Highland Terrane (FHT), Mare Basalt (MB) and South Pole Aitken Terrane (SPAT) (Fig. 2.3).

KREEP refers to rocks that are enriched in K, REE's and P. They are also enriched in Th and other elements of incompatible nature, which are not incorporated into rock-forming minerals during crystallization of magma; hence, they become enriched in the residual magma and in the rocks that finally formed from it. A detailed account of lunar mineralogy and petrology acquired from the study of lunar samples is given in Levinson and Taylor, (1971), Taylor, (1975) and Heiken et al. (1991).

A major advancement in our knowledge about the Moon rocks is that they could be hydrated as opposed to the bone dry nature proposed earlier. Various laboratory studies and remotely sensed signals have indicated towards presence of both endogenic as well as exogenic H_2O/OH^- in the lunar rocks and soil (e.g. Feldman et al., 1998; Saal et al., 2008; Pieters et al., 2009b; Colaprete et al., 2010; Bhattacharya et al., 2013; Klima et al., 2013). In fact, a recent study by Saal et al. (2013) has revealed that origin of the water in the interior of the Moon and the Earth could be same.

2.2.1 Mineralogy

According to Papike et al. (1991), the most common silicate minerals are ortho and clino varieties of pyroxene [$(Ca,Fe,Mg)_2Si_2O_6$], plagioclase feldspar mainly anorthite [$CaAl_2Si_2O_8$], and olivine [$(Mg, Fe)_2SiO_4$]. Potassium feldspar ($KAlSi_3O_8$) and the silica (SiO_2) minerals (e.g., quartz) are comparatively less in abundance on the Moon and occur at isolated sites for e.g. Hansteen Alpha, Lassell Massif, the Gruithuisen Domes, and Aristarchus crater (e.g. Glotch et al., 2011).

Lunar mineral inventory is devoid of Fe^{3+} bearing minerals, micas, clays and amphiboles. Next in abundance to the silicates are the oxide minerals, which are predominantly concentrated in basalts, up to 20% by volume. The major oxide minerals are ilmenite [(Fe, Mg) TiO_3] and spinel {chromite [$FeCr_2O_4$]; ulvospinel [Fe_2TiO_4]; hercynite [$FeAl_2O_4$]; Mg-spinel [$MgAl_2O_4$] and armalcolite [(Fe, Mg) Ti_2O_5]}.

Native iron (Fe) and Troilite (FeS) are the common minor minerals in lunar rocks (Papike, et al., 1991). Iron is ubiquitous and usually small amounts of Ni and Co are also present indicating highly reducing environment under which lunar rocks formed. The rare budget includes apatite [$Ca_5(PO_4)_3(OH,F,Cl)$] and the related whitlockite [$Ca_3(PO_4)_2$]. Rare phosphides, sulfides, and carbides also occur in many lunar rocks.

2.2.2 Petrology

Broadly, rock types on the Moon are classified into highland rocks, volcanic rocks and breccias (Taylor et al., 1991).

a. Highland rocks

The highland rocks are mostly composed of ferroan anorthosites, Mg-suite rocks, and Alkali suite rocks. The ferroan anorthosites are primarily composed of plagioclase feldspar anorthite ($CaAl_2Si_2O_8$). They are light in color and are the most abundant crustal rocks on the Moon. The term "ferroan" is used since the minor minerals in these rocks such as olivines and pyroxenes have higher Fe content compared to the other crustal rocks, which are rich in Mg. The Mg-suite rocks constitute of norites and gabbros, which are composed of pyroxene and plagioclase feldspar; troctolites, containing mostly olivine and plagioclase feldspar; and dunites which are nearly pure olivine rocks.

Compared to the ferroan anorthosites, the Mg-suite rocks exhibit relatively higher KREEP concentration and the Mg# is also high. This particular rock type is not reported from any of the lunar meteorites therefore it is understood that they may be mostly confined to the PKT from where majority of lunar samples were brought during Apollo missions. However, remote sensing observations have revealed exposures of troctolites/dunites, norites, and possibly gabbros (of unknown Mg#) at several sites on the Moon (e.g. Pieters, 1991; Tompkins et al., 1999; Tompkins and Pieters, 1999; Yamamoto et al., 2010; Chauhan et al., 2011; Srivastava et al., 2013).

Further, recently NASA's Moon Mineralogy Mapper (M^3) onboard Chandrayaan-1 discovered a new Mg-rich lithology on the Moon. These are Mg-spinel anorthosites, which are devoid of mafic silicates such as olivine and pyroxene. The discovery of spectral signature of Mg-spinel anorthosite was made along the outer portions of the Moscoviense basin (Pieters et al., 2009b). Since then, they have been reported from several sites across the Moon (e.g. Dhingra et al., 2011; Dhingra and Pieters, 2011; Lal et al., 2012; Bhattacharya et al., 2012; Chauhan et al., 2012; Kaur et al., 2012; Srivastava and Gupta, 2012, 2013; Srivastava et al., 2013; Yamamoto et al., 2013). Origin of this new rock type

on the Moon is not properly understood at present; however, experiments have indicated that they would have formed due to interaction of plutons (mostly Mg-suite variety) with the crustal anorthosites (Prissel et al., 2012, 2013).

The rock types of alkali suite have higher alkali content compared to the other highland rocks therefore they have high Na/Ca value. They also possess high concentrations of La, Th and REE and the Mg# shows significant variations. Analogous to the Mg-suite, the alkali suite also appear to be restricted to the PKT but are comparatively less abundant (Taylor et al., 1991).

b. Volcanic rocks

Three types of volcanic rocks are known to occur on the lunar surface. These are basalts from effusive activity; pyroclasts, resulting from explosive activity; and silica rich evolved lithologies, which are expressions of silicic volcanism on the Moon. The Lunar lava flows forming mare basalts apparently erupted from fissures on the lunar surface. They contain more Fe and less Si, Al than their terrestrial counterparts therefore the lavas were quite fluid and they formed thin widespread flows. Many lava flows accumulated in thick stacks that partly filled many of the large impact basins and craters. The range of compositions among lunar basalts allows for recognition of a wide variety of lunar mare basalt types.

The most striking chemical characteristics of mare basalts are negative Eu anomaly and large variations in TiO_2 content. According to Wieczorek et al. (2006), this variation has enabled classification of mare basalts into four major groups: high-Ti (>8 wt% TiO_2); intermediate-Ti (4 – 8 wt% TiO_2); low-Ti (1- 4 wt% TiO_2), and very low-Ti (<1 wt% TiO_2). Further sub-classification is done on the basis of K_2O and Al_2O_3 concentrations.

The silicic rocks are compositionally evolved lithologies such as granite, its volcanic equivalent rhyolite**,** and the ones with relatively more mafic content such as alkali gabbro and alkali norite**.** Compared to the basalts, these are rare on the Moon and are mostly concentrated in various locales of Oceanus Procellarum such as Gruithensen, Aristarchus, and Hansteen Alpha (Glotch et al., 2011). On the far-side, silicic exposures

have been reported from Compton-Belkovich region - a unique Copernican aged volcanic complex on the Moon (Joliff et al., 2011). A few of these silicic domains have been found to be associated with spectral signatures of endogenic water (Bhattacharya et al., 2013).

The pyroclastic deposits are formed due to explosive release of gases when the rising magma arrives at the surface. As lava decant from a fissure, gases are released ensuing a jet of molten droplets resulting into formation of small glassy beads. On the Moon, these are dispersed extensively around the vents due to low gravity. A typical example of pyroclastic deposit on the Moon is the orange soil at the Apollo 17 landing site. These are known as Dark Mantle Deposits (DMDs) and orbital remote sensing of the lunar surface has revealed presence of several regional scale DMDs on the Moon such as, the Sulpicius Gallus, Rima Bode, Aristarchus region and the dark southern ring of Orientale basin (e.g. Gaddis et al., 1985; Weitz et al., 1998; Head et al., 2002).

Various new DMDs are been regularly reported from the Moon using M^3 data from Chandrayaan-1 (e.g. Besse et al., 2014). Some of these pyroclastic deposits have been found to show enhanced absorption beyond 2.8μm compared to the surroundings. These signatures reveal presence of OH^-/H_2O in them (e.g. Li and Milliken, 2013; Bhattacharya et al., 2013; Srivastava et al., 2013).

c. Breccias

The breccias are made up of fragments of older rocks that have been shattered, crushed, and melted by meteoritic impacts (Stoffler et al., 1980). Most rock samples returned by the Apollo and Luna missions were either monomict or polymict breccias. Polymict breccias are more common and they contain a variety of different materials, which includes several types of bedrock, impact melts, and earlier generations of breccias.

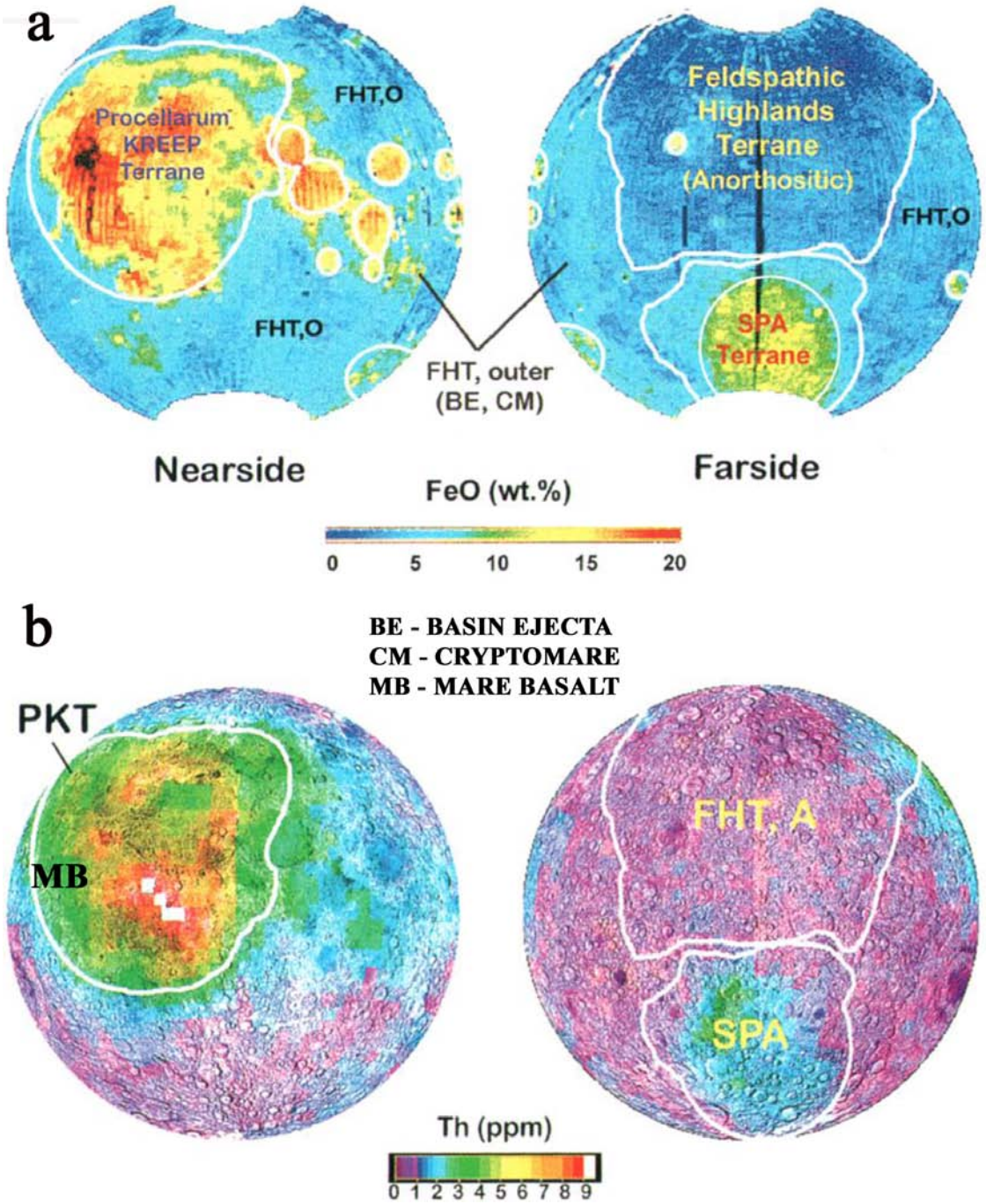

Figure 2.3 Major lunar crustal terranes based on surface morphology and geo-chemical characteristics. a) Global iron map of the Moon from Clementine UVVIS data; b) Global thorium map of the Moon from Lunar prospector data. [Source: Jolliff et al. (2000)]

2.3 Regolith and the megaregolith

The lunar highland crust is overlain by a layer of megaregolith ~10 km thick, and the mega-regolith is overlain by a few meters of surface regolith (e.g. Jaumann et al., 2012). The mega-regolith layer on the Moon formed due to the giant basin forming events and is composed of structurally disturbed crust and ballistically transported coarse grained materials comprising of polymict ejecta and comminuted melt sheets. After the cessation of the giant impact events ~3.8 Ga, the surface regolith formed, which is composed of loose, poorly sorted fine-grained material produced due to gardening of the surface mostly by smaller meteorites (up to micron size), solar wind and cosmic rays which continuously impinge the Moon due to absence of atmosphere and magnetic field.

2.4 Internal structure

Apollo seismic experiments have revealed that the Moon is a differentiated body and is composed of geochemically distinct crust, mantle, and core (Fig. 2.4) (e.g. Wieczorek et al., 2006; Jaumann et al., 2012). The primary crust is mostly anorthositic in composition, the average crustal density is ~2550 kg/cc, and is estimated to be on an average ~34-43 km thick (Wieczorek et al., 2013). The mantle is mostly composed of olivine-pyroxene mixture and a seismic discontinuity exists ~560 km indicating a possible compositional transition to more MgO and Al rich silicates. Depending upon whether it is present globally or not, the depth may also refer to extent of melting during formation of the global magma ocean or extent of melting of mare basalt source regions below the PKT.

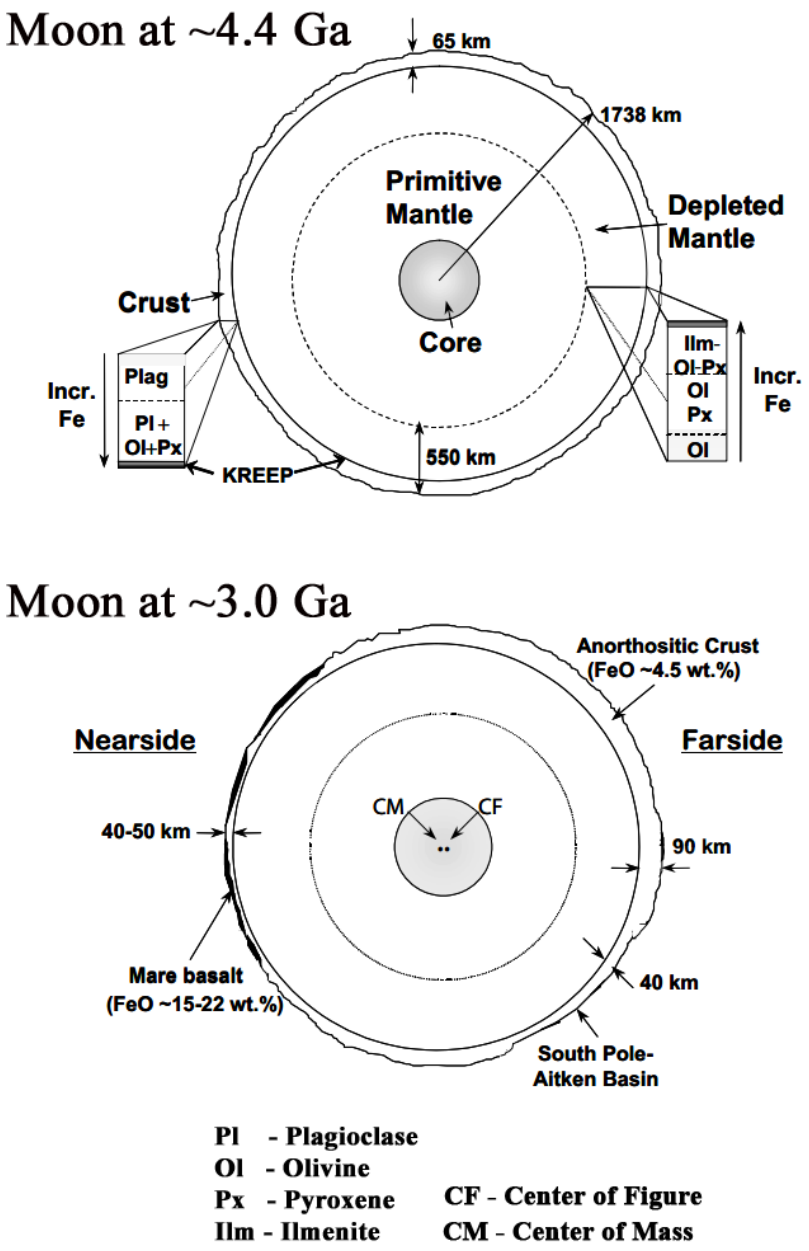

Figure 2.4 A cross-sectional view of the internal structure of the Moon. [Source: Wieczorek et al. (2006)].

In the lower mantle, at a depth of ~1150 km, seismic waves show strong attenuation indicating presence of a partially molten zone extending up to the core (Weber et al., 2011). Based on Apollo seismic data Nakamura et al. (1974) constrained radius of

the lunar core to be within 170-360 km and recently, using seismological array technique Weber et al. (2011) inferred a solid inner core surrounded by a Fe rich liquid layer ~330 km in diameter.

2.5 Origin and evolution

2.5.1 Giant impact hypothesis

It is the most favored hypothesis for the formation of the Moon. Proposed by Hartmann and Davis, (1975), the hypothesis proposes that the Moon was created ~4.56 Ga ago out of the debris left over from a collision between the young Earth and a Mars-sized body known as "Theia" (Fig. 2.5). On collision, the outer silicates of the two bodies would mostly have been vaporized, whereas, the metallic core of Theia would have entered the proto Earth. Hence, most of the material sent into orbit would consist of silicates, leaving the coalescing Moon deficient in iron. The more volatile materials emitted during the collision would have probably escaped, whereas, silicates would have coalesced.

A recent research has revealed similarity in the titanium isotopes for the Earth and the Moon rocks (Zhang et al., 2012). Such a scenario is not feasible if substantial part of the Moon would have formed from materials derived from a body other than the Earth. Thus, at present the origin of the Moon largely remains a mystery.

2.5.2 The Evolutionary Stages

The major evolutionary stages responsible for shaping the present day Moon are the formation of global crust, meteoritic bombardment resulting in formation of large basins, and the mare volcanism (Fig. 2.5). The formation of the lunar crust and mantle is best understood by global magma ocean hypothesis (Warren, 1985, 1990; Elkins-Tanton et al., 2011). It is hypothesized that soon after the formation a large proportion (up to ~500 km) of the Moon or the complete Moon melted due to accumulation of enormous amount of accretionary and radioactive heat ~4.4 Ga. Cooling resulted in fractional crystallization whereby Mg and Fe rich heavier minerals settled at the bottom forming the mantle and the

low density Ca and Al rich crystals along with rafted mafics floated to produce a thick, pristine, and largely anorthositic lunar crust. Later magmatic activity occurred resulting in the formation of plutons and ancient basalts, which are now exposed in dark haloed craters (Bell and Hawke, 1984; Pieters, 1991).

The global magma ocean concept stemmed from the observations that mare basalts were deficient in Eu, which occur both as divalent and trivalent ions in contrast to the other REE that occur only as trivalent ions (Warren, 1985). This difference caused Eu to concentrate in anorthite by substitution of Ca^{2+} leaving behind its depletion in the mantle. Recently, remote sensing data from Kaguya and Chandrayaan-1 have revealed large outcrops of crystalline anorthosite at several places across the Moon especially in the Orientale region, thus furnishing direct evidences for occurrence of global magma ocean during evolution of the Moon (e.g., Ohtake et al., 2009; Cheek et al., 2013; Srivastava and Gupta, 2012, 2013).

The meteoritic bombardments which have occurred throughout the geologic history of the Moon have led to the major modifications of the lunar crust. Initially the impact rate was high and as the flux of impactors reduced with time, the rate gradually reduced and is presently constant (Koeberl, 2006). Dating of lunar samples have revealed that at ~3.9 Ga there was a significant increase in the rate of bombardment. This period is known as Late Heavy Bombardment (LHB) or Lunar Cataclysm (also discussed in sections 1.2, 2.1.1 and 7.1) in the lunar history and has witnessed formation of numerous large basins on its surface.

The secondary crust of the Moon formed due to mare volcanism that occurred subsequent to and even prior to the LHB. Lava flows and pyroclastic deposits provide information about the Moon's internal constitution and the thermal history. Mare volcanism on the Moon began ~4.2 Ga ago and extensive activity continued up to ~3 Ga. The role of impact in mare volcanism is not clear, however, with substantial reduction in the impact flux and significant reduction in heat-generating radioisotopes, frequency of volcanism gradually ceased on the Moon.

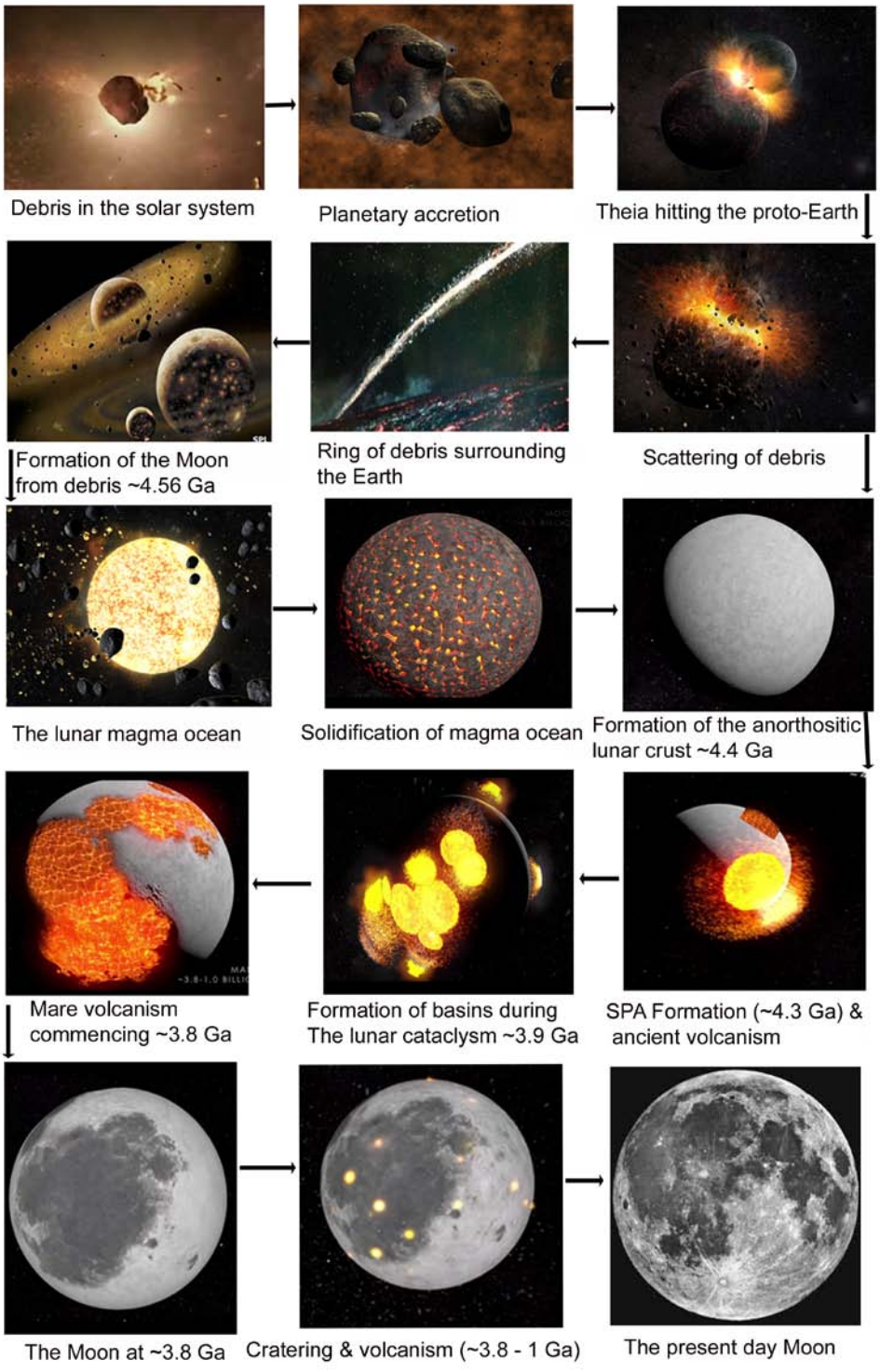

Figure 2.5 A pictorial depiction of origin and evolution of the Moon. [Source of base images: bbc.com, sservi.nasa.gov, i.ytimg.com, thegalaxytoday.com, nasa.gov, thelivingmoon.com]

Nonetheless, crater counting using high-resolution datasets obtained by Clementine, Kaguya, and LRO missions have revealed that sparse mare volcanism continued up to ~1 Ga on the near-side as well as on the far-side of the Moon (Hiesinger et al., 2003; Haruyama et al., 2009; Whitten et al., 2011; Cho et al., 2012) and also possibly at few locations in the late Copernican era (Strom and Fielder, 1968, 1970; Srivastava et al., 2011, 2013; Chauhan et al., 2012). The evolutionary history of the Moon is divided into five main stages (Wilhems, 1987), which are tabulated in Table 2.1.

Table 2.1: Lunar Stratigraphic Systems (Wilhems, 1987)

System	Typical Units	Age (Ga)
Copernican	Fresh, rayed craters; minor maria	~1.2 – present
Eratosthenian	Slightly degraded craters, significant maria	~3.2 – 1.2
Imbrian	Imbrium and Orientale basins; Cayley plains; degraded craters; most maria	~3.85 – 3.2
Nectarian	Nectaris + 12 other basins; many degraded craters; some light plains;	~3.92 – 3.85
Pre-Nectarian	Basins and craters; volcanic and intrusive igneous rocks; megaregolith and crust	~before 3.92

Chapter 3

Lowell crater region – the study area

3.1 Location and extent

The study area termed as “Lowell crater region” covers an area of ~198 x 198 km^2 in the NW quadrant of the Orientale basin on the far side of the Moon, just beyond the western limb (Fig. 3.1). The region encloses ~66 km diameter Lowell crater (centered at ~13°S, 103.4°W). In order to understand the physiography and geologic setting of the Lowell crater region, it is essential to comprehend location and geology of its host mega impact structure – the Orientale basin. Centered ~ (20°S, 95°W), the Orientale basin is a ~930 km diameter impact basin on the western limb of the Moon. It is the youngest and the most well preserved multi-ring basin on the Moon. It is host to several large complex impact craters such as Lowell, Maunder, and Kopff craters. The formation of the Orientale basin defines the beginning of the upper Imbrian period in the lunar stratigraphic system (Wilhelms, 1987).

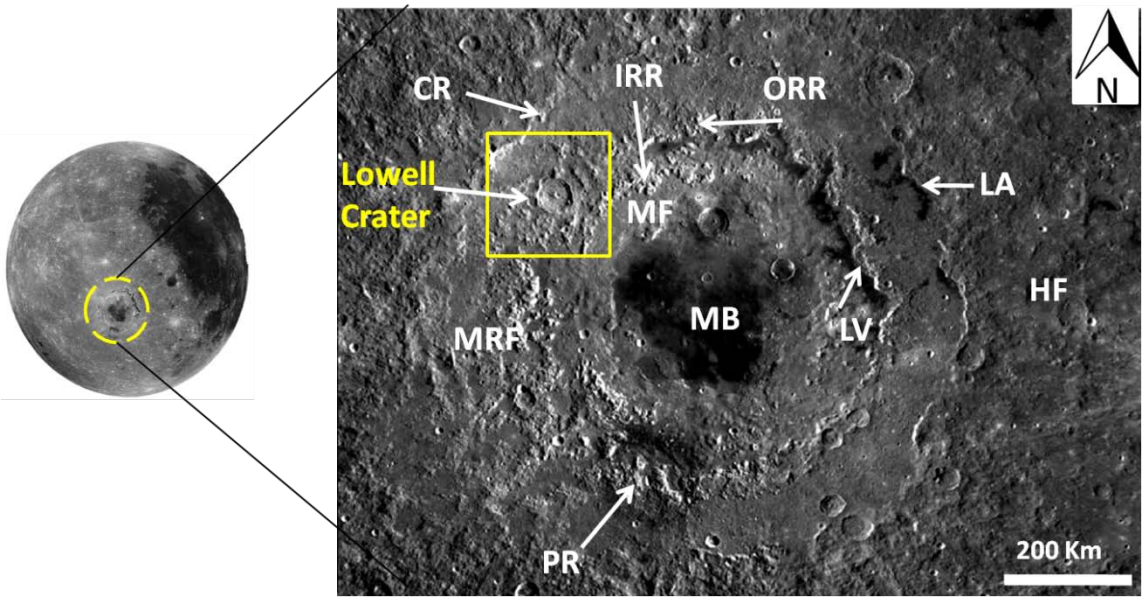

Figure 3.1 LROC – WAC mosaics showing the study area Lowell crater region (enclosed within yellow) inside the Orientale basin located on the western limb of the Moon. The Lowell crater is centered at ~13^{o}S, 103.4^{o}W. The various geological units of Orientale basin are marked such that, HF: Hevelius Formation; MRF: Montes Rook Formation; MF: Maunder Formation; MB: Mare basalt; LA: Lacus Autumni; LV: Lacus Veris; PR: The pyroclastic ring deposits; CR: Cordillera Ring; ORR: Outer Rook Ring; IRR: Inner Rook Ring. [Source of base images: lroc.sese.asu.edu and wms.lroc.asu.edu]

3.2 Geology of the Orientale basin

The multi-ring basins on the near side of the Moon are largely filled with basalts obscuring morphological features. In contrast, most of the far side basins reveal morphology due to absence of mare basalts, possibly due to thicker far side crust. Therefore, both these categories of basins do not provide an opportunity to simultaneously study the morphological and compositional make-up of these mega impact structures.

Orientale basin on the western limb of the Moon, at the near side far side transition, is distinctively different from these basins. The basin is only partially filled with basalts; therefore, it clearly showcases the morphological and topographical details of the impact basin and volcanic features that formed afterwards. Thus, the Orientale basin provides an

opportunity to simultaneously investigate impact cratering and volcanism - the major geological processes that have modified the Moon since its formation.

The Orientale basin possesses three prominent rings defined by the outermost - Cordillera Ring (CR); middle - Outer Rook Ring (ORR), and the innermost - Inner Rook Ring (IRR), with diameters of ~930 km, ~620 km, and ~480 km respectively (Head, 1974). The CR is understood to be the equivalent of crater rim, the ORR marks the possible boundary of the transient cavity that formed during the Orientale impact event, and the massifs of the IRR are considered to be equivalent to the central peak of a complex crater. From various basin forming models and photo-geological interpretations of images available from the earlier Moon missions, it is understood that faults and dikes are likely to be present along the rings (e.g. Melosh, 1989**,** Whitten et al., 2011). There are four principal geological formations in Orientale basin. These are described in the following sub-sections.

3.2.1 The Maunder Formation

The Maunder Formation (MF) represents the impact melt sheet created by large scale melting of the upper crustal rocks during basin formation impact event and lies largely within the Inner Rook Ring. The melt sheet is a mature, iron-poor highland unit. Its spectral signature corresponds to a feldspathic, "upper" crustal rock type, such as anorthositic norite or noritic anorthosite (e.g. Spudis et al., 1984; Hawke et al., 1991; Bussey and Spudis, 1997, 2000). Recent studies have indicated towards possibility of fractionation and differentiation in this melt sheet after its formation, resulting into a layered structure (Vaughan et al., 2013).

3.2.2 The Hevelius Formation

The Hevelius Formation (HF) refers to the ejecta blanket that lies beyond the CR and extends up to ~500 km from the base of the Cordillera Mountains. It is uniformly feldspathic in composition similar to the Maunder Formation (Bussey and Spudis, 1997, 2000; Spudis et al., 1984; Belton et al., 1992; Head et al., 1993).

3.2.3 The Volcanic units

The basalts of the Orientale basin comprises of mare basalts (~1 km thick basalts that lie within the IRR) and the lacus units Lacus Veris and Lacus Autumni of limited areal extent at the base of ORR and CR respectively (e.g. Whitten et al., 2011). The mare basalt resulted from magma flooding of the basin ~3.58 Ga ago, ~300 Ma after the formation of the Orientale basin. The lacus units are mostly present in the northeastern part of the Orientale basin and are understood to have been formed during the later stages of the Orientale basin evolution when the volcanic activity shifted to higher altitudes producing pulses of volcanism along the CR and the Outer Rooks. Some of the ponds in Lacus Autumni are as young as the youngest basalts (~1 Ga) of Oceanus Procellarum (Whitten et al., 2011; Cho et al., 2012).

Though these basalt exposures are severely contaminated with highland material (e.g. Spudis et al., 1984; Whitten et al., 2011), Spudis et al. (1984) concluded that compositionally they are similar to the near side basalts. Spectral reflectance studies using Galileo data and Clementine data have revealed that most of these basaltic soils are of medium to high Ti variety (TiO_2 ~ 1–8 wt %) (e.g. Greeley et al., 1993; Bussey and Spudis, 2000).

Apart from the effusive activity resulting in basalts, the Orientale basin also witnessed explosive volcanic activity in the form of pyroclastic volcanism (Schultz and Spudis, 1978; Head et al., 2002). A distinct ~100 km diameter low albedo ring of pyroclastics with a definitive source crater at the centre is present in the SW part of the Orientale basin.

3.2.4 The Montes Rook Formation

The Montes Rook Formation (MRF) is knobby in appearance and lies predominantly between the ORR and the CR. It is understood to represent mega sized deep-seated ejecta materials derived and emplaced during the Orientale impact event. They are slightly more mafic than the Hevelius Formation (Bussey and Spudis, 1997). However, surprisingly the Montes Rook Formation show FeO content of only ~(2–6 wt %), which is similar to the Hevelius Formation (Bussey and Spudis, 2000).

3.3 Lowell crater: geologic significance

The Lowell crater occurs in the Montes Rook Formation between the ORR and the CR in the NW quadrant of the Orientale basin. It is named after Percival Lowell, a US astronomer who founded the famous Lowell observatory of Arizona (Menzel et al., 1971). As shown in Fig. 3.1, its eastern rim intersects the ORR and possibly the target rocks for the impact event would have been mostly the knobby massifs of Montes Rook Formation. The crater is Copernican or Imbrian in age (McEwen et al., 1993; Scott et al., 1977). The lithological assemblage of its central peak comprises of gabbroic and anorthositic rocks (Tompkins and Pieters, 1999) and the average estimated TiO_2 wt% for the central peak is 0.44±0.14 (Srivastava, 2008).

Lowell crater is plausibly the youngest and the largest impact crater inside Orientale basin (within CR, its outermost ring). The crater is geologically important due to its location in the Montes Rook. It lies just outside/intersects the ORR, which defines the limit of the transient that formed during the Orientale impact event. Due to its large size, it is expected that the Lowell impact event would have excavated parts of the Orientale ejecta and some part of the Orientale target facies. Also, the Lowell crater provides an opportunity to investigate the effect of Orientale forming impact event on the structural make-up of the area, which lies along the ORR.

Chapter 4

Datasets used and methodology overview

4.1 The Missions

Remote sensing data from recently accomplished/ongoing missions Chandrayaan-1, Kaguya, and Lunar Reconnaissance Orbiter (LRO) have been used in this study (Fig. 4.1). Here, a brief account of these missions, their science goals, and payload configuration is discussed.

4.1.1 Chandrayaan – 1

Chandrayaan-1, India's maiden Moon mission was launched on 22nd Oct., 2008 at 6:30 am IST, from Satish Dhavan Space Center, Sriharikota using PSLV-XL. On 8th Nov., 2008 it entered the lunar orbit. Chandrayaan-1 was conceived keeping in mind its probable role in strengthening lunar science and was designed to execute the following objectives (Bhandari et al., 2004; Goswami and Annadurai, 2009**)**:

- Preparing a 3-D topographical map of the Moon
- Detecting and estimating mineral abundance through hyperspectral imaging
- Chemical mapping using X-ray fluorescence and γ-ray spectroscopy
- Recognition of potential sites for water

Accordingly, Chandrayaan-1 was fashioned as a polar lunar orbiter cuboidal in shape (approx. 1.50 m). It surveyed the Moon from Nov., 2008 to Aug., 2009 from an altitude of ~100 km and from a raised orbit of ~200 km during the terminal phase of the mission. It was equipped with state-of-the-art remote sensing devices capable of providing accurate high resolution data in the visible, infrared, X- ray, and gamma ray regions of the electromagnetic spectrum.

There were eleven payloads in the lunar craft (Goswami and Annadurai, 2009). Six of them were indigenous and remaining five either international guest payloads or made in collaboration with Indian counterparts. The optical sensors include panchromatic Terrain Mapping Camera [TMC; spatial resolution ~10 m] for surface morphology and morphometry studies and hyperspectral sensors [Hyperspectral Imager (HySI), Moon Mineralogy Mapper (M^3), and Infrared spectrometer (SIR-2)] for compositional mapping.

Other instruments onboard Chandrayaan -1 include Lunar Laser Ranging Instrument [LLRI] to measure altitude of the spacecraft from the lunar surface, High Energy X-ray spectrometer (HEX) to measure concentration of radioactive elements, Chandrayaan-1 X-ray Spectrometer (C1XS) to measure the elemental composition, Miniature Synthetic Aperture Radar (Mini SAR) to explore the mysterious polar regions, Sub-Atomic Reflection Analyser (SARA) to study the solar wind – surface interaction and magnetic anomalies, Radiation Dose Monitor (RADOM) for studying radiation environment around the Moon, and Moon Impact Probe (MIP) with an inbuilt camera and a spectrometer.

Power backup in the lunar craft was provided by solar arrays. During eclipses, power generation was supported by Lithium ion batteries. The ground segment, a regulatory entity comprises of three basic infrastructural units. These include Deep Space Network (DSN), Spacecraft Control Center (SCC), and Indian Space Science Data Center (ISSDC). These were specifically designed to support Chandrayaan-1 and other upcoming

planetary missions of ISRO. The telemetry, tracking and command were communicated through S-band frequency and the data was received from the lunar craft in the X-band frequency. For these purposes, two antennae measuring 18 m and 32 m were set up at ISRO tracking centre at Byalalu, near Bangalore.

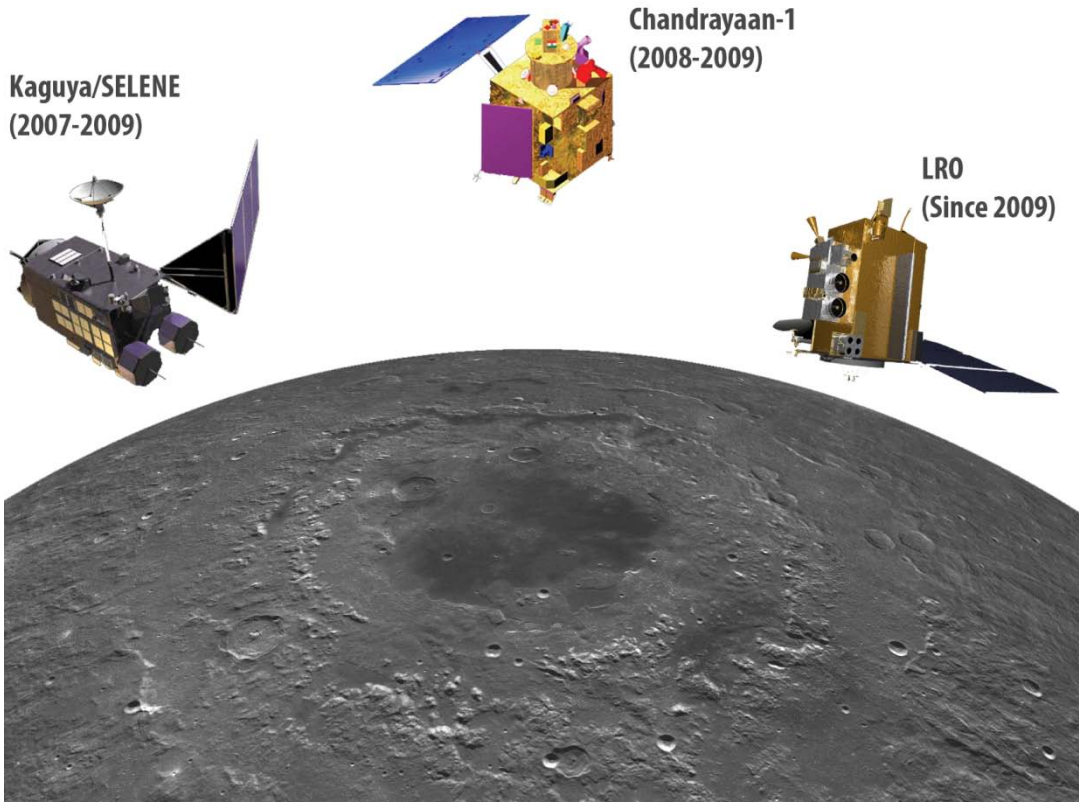

Figure 4.1 A schematic representation of the spacecrafts Kaguya, Chandrayaan-1, and LRO observing the Orientale basin on the Moon. Panchromatic images, DTM's, and hyperspectral data from these three missions have been used in this study. [Source of images: phys.org (Moon showing Orientale), nssdc.gsfc.nasa.gov (LRO), brahmand.com (Chandrayaan-1), nssdc.gsfc.nasa.gov (Kaguya)]

4.1.2 Kaguya

Launched on 14th Sept., 2007 by H-IIA from Tanegashima Space Center, the Japanese lunar mission KAGUYA (SELENE: Selenological and Engineering Explorer) of JAXA entered polar orbit of the Moon on 4th Oct., 2007 (Kato et al., 2010). The major science objectives were:

- Study of the origin and evolution of the Moon
- In-situ measurement of the lunar environment
- Observation of the solar-terrestrial plasma environment

The mission comprised of a main orbiter and two sub-satellites OKINA and OUNA. A total of 14 instruments were present on the main orbiter and the two sub-satellites which got separated from the main orbiter Kaguya after entering the lunar orbit. Kaguya observed the lunar surface for about a year and eight months and finally it was crashed on to the surface of the Moon in a controlled operation on 10th June, 2009 near Crater Gill on the SE limb.

Science payloads aboard the main orbiter Kaguya include X-ray spectrometer and γ-ray spectrometer for chemical mapping, Lunar Imager/SpectroMeter (LISM) for producing high-resolution digital imagery and spectroscopic data for surface mineralogy and surface morphology studies, RADAR Sounder and LASER altimeter for surface/subsurface structure determination and Lunar Magnetometer, Plasma Imager, Charged Particle Spectrometer, and Plasma Analyzer for studying the surface and space environment. The LISM consisted of three sub-systems: Terrain Camera (TC), Multiband Imager (MI), and Spectral Profiler (SP).

4.1.3 Lunar Reconnaissance Orbiter (LRO)

As a part of the US Vision for Space Exploration program NASAs LRO mission was launched on 18th June, 2009 by Atlas V 401 launch vehicle from Cape Canaveral Air Force Station along with a companion satellite Lunar Crater Observation and Sensing Satellite (LCROSS). The duo reached the Moon's orbit on 23rd June, 2009 and the LRO is still under operation. Similar to the reconnaissance surveys by the Lunar Orbiters in the 60s which laid the foundation for Apollo landings, the LRO mission intends to do the necessary background work to facilitate next generation human exploration of the Moon (Robinson et al., 2010). The specific objectives include:

- Identifying and mapping of potential lunar resources
- Preparing detailed maps of the lunar surface

- Collecting information on the Moon's radiation levels
- Studying Polar Regions for resources usable in manned / robotic sample return in future
- Providing data to characterize future robotic / human landing sites and
- Measurements directly usable for future Lunar Human Exploration

Immediately after reaching the Moon's orbit LCROSS recorded definitive evidences for presence of water-ice on the Moon by impacting a Centaur rocket into a permanently shadowed crater Cabeus on the lunar South Pole and by studying the composition of the plume (Colaprete et al., 2010).

The payload suite and experiments onboard LRO consists of Lunar Reconnaissance Orbiter Cameras (LROC) and a Lunar Orbiter Laser Altimeter (LOLA) for global surface morphology and topography; a Cosmic Ray Telescope for the Effects of Radiation (CRaTER) for characterizing the radiation environment of the Moon; a Diviner Lunar Radiometer Experiment (DLRE) to measure thermal emission for determining surface composition; and, a UV probe Lyman Alpha Mapping Project (LAMP), a Mini-RF Lunar Exploration and a Neutron Detector (LEND) for search of water ice.

4.2 Payload details

Data from Moon mineral M^3 (Chandrayaan-1), TC, MI (Kaguya) and LROC-NAC, WAC (LRO) have been used in the present study (Fig 4.2). The technical specifications and archival details of the data are given in Table 4.1 and the list of data used in the study is provided in Table 4.2.

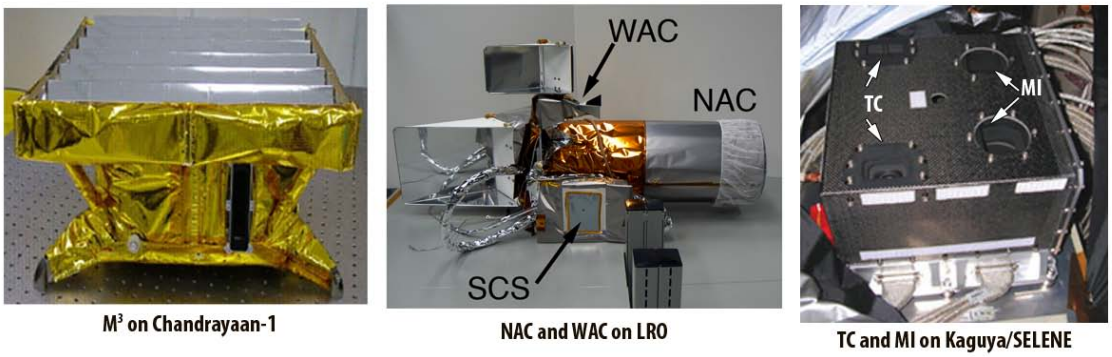

Figure 4.2 A mosaic showing payloads whose data have been used in the study. Here, M^3: Moon Mineral Mapper; WAC: Wide Angle Camera; NAC: Narrow Angle Camera; SCS: Sequence and Compressor System; MI: Multi-band Imager; TC: Terrain Camera [Source of images: isro.org (M^3), lroc.sese.asu.edu (NAC, WAC) and kaguya.jaxa.jp (TC, MI)].

4.2.1 Moon Mineral Mapper (M^3)

NASA's discovery instrument M^3 flew aboard ISRO's Chandrayaan-1 mission as a guest payload (Goswami and Annadurai, 2009; Green et al., 2011; Boardman et al., 2011). Designed and built at Jet Propulsion Laboratory (JPL), Pasadena, California, it is a state-of-the-art imaging spectrometer, in fact the first imaging spectrometer (along with the ISROs indigenous HySI, also on Chandrayaan-1 mission) to fly to the Moon for dedicated observations and mapping.

According to Green et al. (2011), accurate compositional mapping using reflectance spectroscopy in visible and near infrared from M^3 were aimed to accomplish the following objectives:

- Characterization of the lunar highland rocks in the context of geologic processes
- To identify and characterize the diversity of lunar volcanism
- To identify and map the presence of hydrous phases
- To identify the recent impact flux at 1 AU and use craters as probes to the interior
- Identification of areas of rare or previously unseen lunar materials
- To determine if detected polar hydrogen is related to H_2O
- To identify and map areas with diverse "feedstock" for future utilization

M^3 is a pushbroom type imaging spectrometer with a FOV of 24^o (40 km from 100 km orbit). It has mapped > 95% of the lunar surface in the Global mode during the life time of the mission (Green et al., 2011). Also several sites of high scientific value have been observed at a very high resolution in the targeted mode.

4.2.2 Terrain Camera (TC)

The Terrain Camera (TC) forms a part of LISM onboard Kaguya (Haruyama et al., 2008). It is a pushbroom panchromatic imager with 2 optical heads, TC1 and TC2, each comprising of a linear CCD sensor of 4096 pixels. TC1 and TC2 have slant angles of ±15°, an instantaneous field of view is 0.00553° and the sampling interval is 6.5 ms, on the lunar surface at the spacecraft. In the normal-swath mode the TC swath is 35 km, which provides sufficient overlaps in the data for producing image mosaics. It has acquired stereo data for > 99% of lunar surface (Haruyama et al., 2012).

4.2.3 Multiband Imager (MI)

Also a part of LISM onboard Kaguya, MI is a high-resolution multiband imaging camera consisting of visible and near infrared sensors (Haruyama et al., 2008; Ohtake et al., 2008). It acquires imaging data in the pushbroom mode by using selected lines of area arrays. The spectral band assignments are 415, 750, 900, 950 and 1000 nm for visible and 1000, 1050, 1250 and 1550 nm for near infrared. The spatial resolution of visible bands is 20 m, and that of near infrared bands is 62 m from the 100 km orbit.

4.2.4 Lunar Reconnaissance Orbiter Camera (LROC)

The LROC consists of two Narrow Angle Cameras (NAC's) and a single Wide-Angle Camera (WAC) (Robinson et al., 2010). The NAC's are monochromatic pushbroom scanners each comprising of 700 mm focal length Cassegrain telescope that images onto a 5064 pixel CCD line array providing a cross track field of view (FOV) of 2.85° with an IFOV of 10-microradians (angular resolution of 50 cm from the 50 km nominal orbit).

The WAC is a push-frame imager and works both in multispectral and monochrome mode. It has two lenses imaging onto the same 1024 x 1024 pixel, electronically shuttered CCD area array, one imaging in the visible/near infrared (VIS), and the other in the Ultraviolet (UV). In monochrome mode, 1024 x 14 pixels are read out in one visible band (645 nm). In color mode, only the center 704 x 14 visible pixels and 512 x 16 UV pixels binned to 128 x 4 pixels, are read out for each band. The VIS optics have a cross track FOV of 91.7° (monochrome) and 61.4° (color), and the UV optics a 58.96° FOV.

4.3 Methodology overview

The detailed methodology adopted for carrying out surface morphology and morphometry, spectral reflectance studies, and crater chronology has been discussed in the respective chapters 5-7. Here, the salient points giving a brief account of the steps adopted to accomplish the objectives of the study are listed. These are:

- Detailed review of relevant scientific literature on lunar geology, impact cratering, reflectance spectroscopy, and dating of planetary surfaces has been carried out for identification of the research gaps and subsequent formulation of the objectives.
- The data were downloaded through public access web portals (Table 4.1) and were geo-referenced and mosaicked using image processing software ENVI (except for WAC data, for which the mosaic was downloaded) to carry out analysis.
- A broad morphological survey of the study area has been carried out using coarse resolution LROC-WAC and photometrically corrected 750 nm M^3 data to identify various morphological units in the Lowell crater region. Specifically the units of Lowell crater (the crater rim, exterior ejecta deposits, interior and exterior melt pools, crater floor irregularities, central peak area, terraced crater walls, lineaments, and the various resurfaced areas) have been identified and mapped.

Table 4.1: Technical specifications and archive details for the datasets used in the study. [Sources: Goswami and Annadurai, (2009) and Green et al. (2011) for M^3; Robinson et al. (2010) and lroc.sese.asu.edu for LROC NAC and WAC; Haruyama et al. (2008), Ohtake et al. (2008) and kaguya.jaxa.jp for TC and MI]

Mission, (Launch Year) [Agency]	**Sensor [Calibration level], [Radiometric Resolution]**	**Resolution Spatial and/or Vertical (Swath)**	**Spectral range , resolution**	**Website (Archive)** **[Misc. Details]**
Chandrayaan-1, 2008 [Indian Space Research Organization (ISRO)]	Moon Mineral Mapper (M^3) [Level 2] 12 bit	~140 m (Global Mode) from 100 km orbit (40 km)	Hyperspectral (83 bands) in the spectral range (540 nm – 2980 nm) with 20 – 40 nm resolution	http://ode.rsl.wustl.edu/moon/indexProductSearch.aspx
Lunar Reconnaissance Orbiter (LRO), 2009 [National Aeronautics and Space Administration (NASA)]	LROC –NAC) 12 bit (encoded to 8 bit)	~ (0.5 m – 1m) (5 km)	Panchromatic (400 – 750 nm)	http://wms.lroc.asu.edu/lroc [Among WAC data, global base map mosaic from the visible monochrome images has been used in this study.]
	LROC – WAC 11 bit (encoded to 8 bit)	~100 m (105 km – 57 km)	Multispectral, also works in monochrome mode in visible	
Kaguya, 2007 [Japan Aerospace Exploration Agency (JAXA)]	Multi-band Imager – Visible (MI – VIS) [Level 2b] 10 bit	20 m (19.3 km)	Multispectral (5 bands): 415-1000 nm	https://www.soac.selene.isas.jaxa.jp [MI –VIS data – only 750 nm band is used] [DTM_TCortho: scene data files of DTM, TC ortho, and qualification flag created from TC_w_Level2A
	Terrain Camera (TC) [Level: L3D] 10 bit	7.4 m Relative height resolution ~ few 10s of m (35 km)	Panchromatic image and DTM	

Table 4.2 List of datasets used in the study.

Chandrayaan – 1 M^3	**Kaguya TC**	**Kaguya MI**
M3G20090213T061652	DTMTCO_03_02783S142E2594SC	MVA_2B2 _01_0 2 452S132E2573
M3G20090213T080353	DTMTCO_03_04950S097E2585SC	
M3G20090213T180532	DTMTCO_03_02783S102E2594SC	
M3G20090213T195213	DTMTCO_03_04951S097E2574SC	
M3G20090213T115953	DTMTCO_03_02784S155E2584SC	
M3G20090213T155552	DTMTCO_03_04954S157E2542SC	
M3G20090213T195213	DTMTCO_03_04953S157E2553SC	
M3G20090213T140913	DTMTCO_03_04954S104E2542SC	
M3G20090213T101313	DTMTCO_03_04954S144E2542SC	**LROC - NAC**
M3G20090213T180532	DTMTCO_03_04952S157E2564SC	
M3G20090212T222453	DTMTCO_03_02785S156E2573SC	M184196652RE
M3G20090213T001153	DTMTCO_03_04950S111E2585SC	M184196652LE
M3G20090213T022112	DTMTCO_03_02784S115E2583SC	M181844927RC
M3G20090213T040732	DTMTCO_03_04954S130E2542SC	M181844927LC
M3G20090422T134730	DTMTCO_03_04951S110E2574SC	M105192594RE
M3G20090212T104932	DTMTCO_03_04950S137E2585SC	
M3G20090213T122313	DTMTCO_03_04952S104E2564SC	
M3G20090213T162141	DTMTCO_03_04953S103E2553SC	
M3G20090212T184721	DTMTCO_03_04954S117E2542SC	**LROC - WAC**
M3G20090212T203719	DTMTCO_03_04953S144E2553SC	
M3G20090422T174330	DTMTCO_03_02783S155E2595SC	*Orientale
M3G20090212T203852	DTMTCO_03_02783S129E2594SC	
M3G20090211T224812	DTMTCO_03_04950S151E2585SC	
M3G20090422T113800	DTMTCO_03_02783S115E2594SC	
M3G20090212T143253	DTMTCO_03_02784S128E2583SC	
M3G20090212T082712	DTMTCO_03_02785S142E2573SC	
M3G20090422T153400	DTMTCO_03_04951S124E2574SC	
M3G20090421T082045	DTMTCO_03_04951S137E2574SC	
M3G20090211T231038	DTMTCO_03_04952S117E2564SC	
M3G20090212T003453	DTMTCO_03_04952S131E2564SC	
M3G20090212T011737	DTMTCO_03_04952S144E2564SC	
M3G20090212T044205	DTMTCO_03_04953S117E2553SC	
M3G20090212T064032	DTMTCO_03_04953S130E2553SC	
M3G20090212T082712	DTMTCO_03_05797S142E2554SC	

*Mosaic downloaded from http://wms.lroc.asu.edu/lroc_browse/view/orientale

- Standard morphometric parameters for complex impact craters such as crater depth, rim height, rim diameter, floor diameter, and central peak dimensions (Melosh, 1989; Pike, 1974, 1977a, 1977b, 1980, 1985; Shoemaker, 1962; Stöffler et al., 2006) have been determined for the Lowell crater from TC DTM by drawing cross-sections across the crater. Four cross-sections have been drawn in the NS, EW, NW-SE, and NE-SW directions to take care of the various surface heterogeneities. Parameter values estimated from each of these sections have been averaged to determine a representative value.

- The morphology and the morphometry of the Lowell crater have been used to assess the Lowell impact conditions.

- Surface composition has been inferred based on the characteristic spectral reflectance curves of the lunar minerals. For this, photometrically and thermally corrected Level – 2 M^3 hyper-spectral images have been used. Spectral parameters such as band shape, band center and integrated band depth (IBD) have been used to identify the dominant mineral composition in an area.

- Surface maturity due to space weathering adversely affects the composition dependent reflectance spectra on the airless Moon. Therefore, to ensure more reliable interpretations, analysis have also been made on the basis of average spectral reflectance curves derived for specific areas such as small craters which are fresh and least mature. Regional assessment of spectral variations have been made by preparing false color composites (FCC^s) using popularly used schemes [R: IBD 1000 nm, G: IBD 2000 nm and B: R1578 nm (Cheek et al., 2011)] and [R: R1209 nm/R1818 nm, G: R730 nm/R930 nm and B: R1000 nm/R1250 nm (Dhingra et al., 2011)].
- Due to diverse spectral behaviour of the area a Minimum Noise Function (MNF) based FCC has been prepared to make optimum use of the M^3 hyperspectral data. The mineralogy of different units of the Lowell crater has been used to derive an understanding of the variations in composition of rocks with depth in the area of impact.

- The formation age of the Lowell crater has been determined by applying crater chronology technique (e.g. Neukum and König, 1976; Neukum 1983; Neukum and Ivanov, 1994; Neukum et al., 2001) which involves fitting the observed crater size-frequency distribution (CSFD) of a surface unit to a known production function (PF), and to use chronology function (CF) to obtain an absolute age. Relatively flat areas with minimal resurfacing have been selected on the proximal ejecta blanket for crater counting to ensure reliable age estimates. Manual crater counting has been performed using ArcGIS based CraterTool and curve fitting has been accomplished using CraterStats software as described in Kneissl et al. (2011).

- Detailed investigations involving very high resolution surface morphology studies (using LROC-NAC data and Kaguya MI, TC images), delineation of specific topographic relationships, and assessment of spectral associations have been carried out for selected targets.

- Based on the findings from the study, geology of the Orientale basin and the existing understanding of the evolution of the Moon, the geological evolution of the Lowell crater region have been inferred.

Chapter 5

Surface morphological analysis

5.1 Regional topography and morphology

The surface topography of the Lowell crater region in the northwestern quadrant of Orienatle basin is shown in a 3D view (of a part of the area) derived from TC DTM and image mosaics (Fig. 5.1). The topographic profiles showing relief in the area are plotted in Fig. 5.2. The terrain (occupying an area of ~198x198 km^2) has been found to be extremely undulating with a relief of ~9.5 km. The Lowell crater region is bounded by steep and high outermost Orientale ring (the Cordillera scarp) on the northwestern side and the Inner Rook massifs, and portions of low lying Maunder formation on the southeastern side. The Cordillera scarp attains a maximum height of ~6 km from the adjoining low lying areas

(section CC') and the massifs of Inner Rook show elevations up to ~3 km, relative to the Maunder lows (section BB' in Fig 5.2).

The central part of the Lowell crater region is occupied by Lowell crater having a diameter of ~66 km and depth of ~3.5 km (sections BB' and DD'). The Lowell crater is centred at ~(13^{o}S, 103.4^{o}W) and it exhibits a prominent central peak, which is up to ~1.7 km high above the Lowell crater floor (Fig. 5.2). Distinct topographic units are present in the areas adjacent to the Lowell crater. Commencing at the apex of the Lowell crater, a northward trending chain of peaks and plateau occur (P), which is up to ~3 km high (section AA'). Smooth plains are present on both the sides of these uplands. Numerous less elevated small surface mounds ~1.5 km high (section AA' and CC') are present in the southern part.

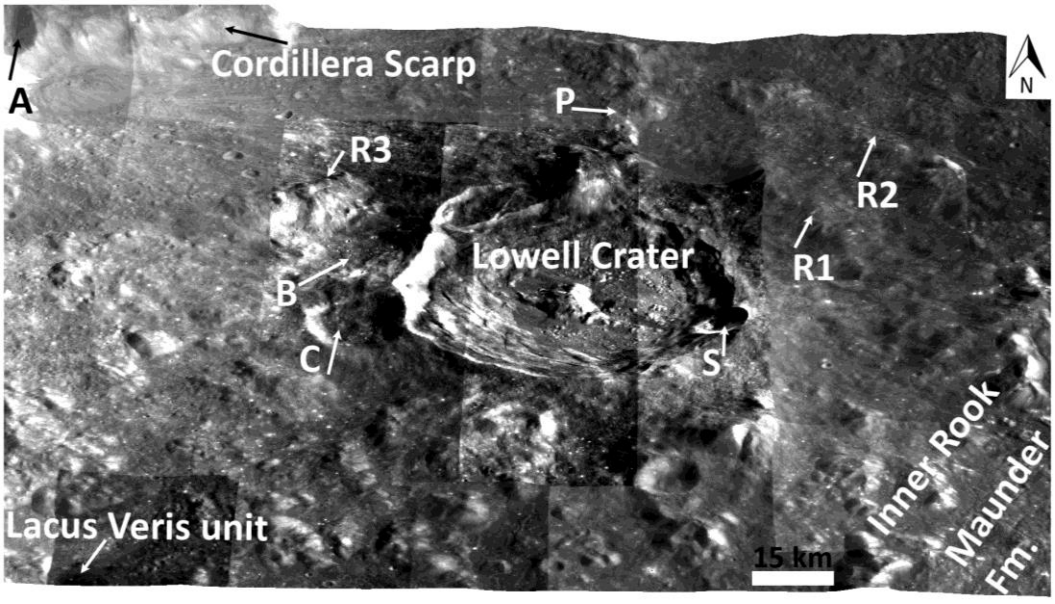

Figure 5.1 A 3D view of a part of Lowell crater region showing the regional topography. The major geologic formations of the area are marked and the various notations used are - R1, R2 and R3: major ridges in the area; P: northward trending peaks and plateau; A, B and C: major depressions/craters; S: small superposed crater over Lowell crater wall. Here vertical exaggeration is 5.

A pair of prominent ~NW-SE trending ridge (R1 and R2) and a conspicuous ~NE-SW ridge (R3) are present near to the northeastern and the northwestern flanks of the Lowell crater respectively. In addition to these, two prominent conspicuous pre-existing

depressions are present bordering its western edge (B and C). Among these, C is a shallow pre-existing crater (~20 km in diameter) and B could also be a severely modified pre-existing crater with R3 defining its rim. Two small and deep asymmetric fresh rayed Copernican craters A and S are present in the area, which have formed on the steep slopes of Cordillera scarp and the Lowell crater wall respectively. The ejecta emanating from these craters superpose the preexisting topography of the region.

5.2 General morphology and morphometry of Lowell crater

Here, morphology of Lowell crater, which is the major surface feature in the study area, is described. The morphological features of the Lowell crater are shown in Fig. 5.3 and Fig. 5.4. The Lowell crater is polygonal in shape and exhibits features such as a prominent central peak, terraced crater wall which is broader on one side, an asymmetric continuous ejecta blanket, interior and exterior impact melt deposits, crater floor irregularities, lineaments, and numerous slump zones. Additionally, a ~9 km diameter superposed crater is present on the central part of the eastern flank of the Lowell crater. Hereafter, in this study, this superposed crater has been referred to as Crater S.

Morphometry refers to quantitative description of the shape of the landforms on a planetary body and it complements the other techniques of morphological analysis such as visual observations and photo-interpretations. In the case of the Moon, morphometry particularly refers to the geometric measurements of impact craters (Pike, 1973). These tools were developed during telescopic studies of the Moon (prior to the Apollo program) to strengthen the investigations in absence of opportunities for field studies. They have been widely used to study lunar craters using Apollo panoramic and orbital metric photographs (e.g. Pike, 1973, 1974, 1977a, 1977b, 1980, 1985).

Morphometry of impact craters describe the basic diameter-dependent variations in crater topographic features (Stoffler et al., 2006). The geometric parameters commonly used for this purpose includes crater depth, rim height, rim width, width of rim flank, rim wall slope, floor diameter, height of central peak, and basal area of central peak. Detailed measurements on lunar imageries have made it possible to represent the different geometrical characteristics of lunar impact craters by equations of a power law form $y = a$

D^b. Here, y is a given crater characteristic, *D* is the rim - rim diameter of the crater and a, b are constants.

In this study, morphometric parameters for the Lowell crater (and also Crater S) have been derived from TC DTM and four derived topographic sections passing through the central peak of the Lowell crater along AA', BB', CC' and DD' in the ~ N-S, E-W, NW-SE and SW-NE directions respectively (Fig. 5.2). The values are listed in Table 5.1. Also, using the relation of Croft, (1985), it has been estimated from the present day diameter of the Lowell crater that the transient cavity, which would have formed during the initial stages of the cratering process, could be ~54 km wide.

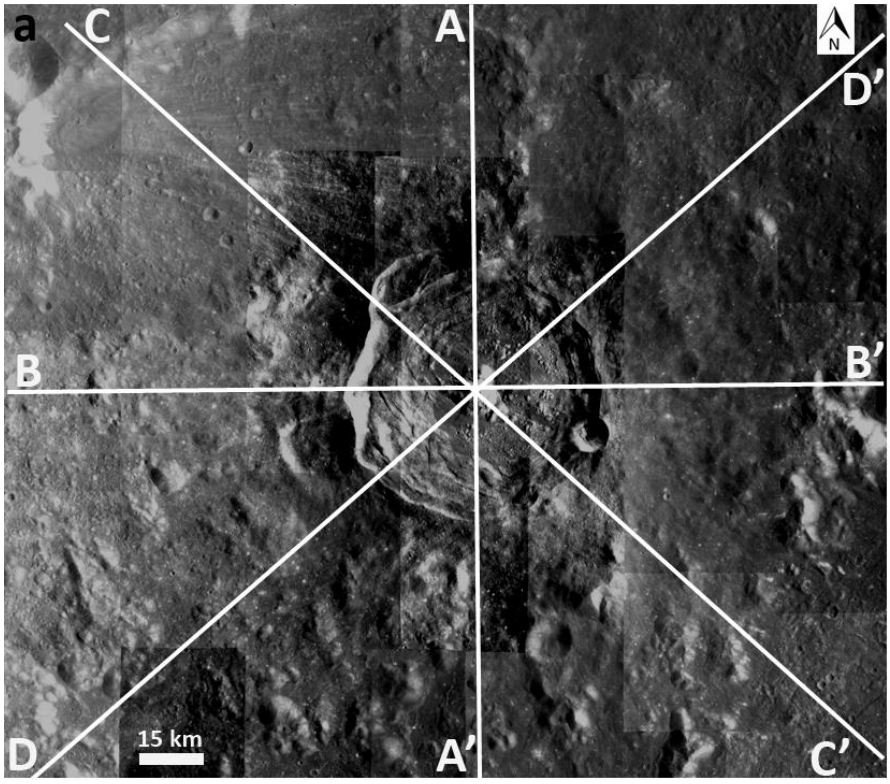

Figure 5.2 The topographic cross-sections for the Lowell crater region from TC DTM mosaic showing relief variations and undulating nature of the terrain. a) TC image mosaic of showing the extent of transects for which topographic profiles have been derived and plotted in sub-sections b-e; b) Profile AA' along ~ N-S direction; c) Profile BB' along ~W-E direction; d) Profile CC' along ~NW-SE direction; e) Profile DD' along SW-NE direction.

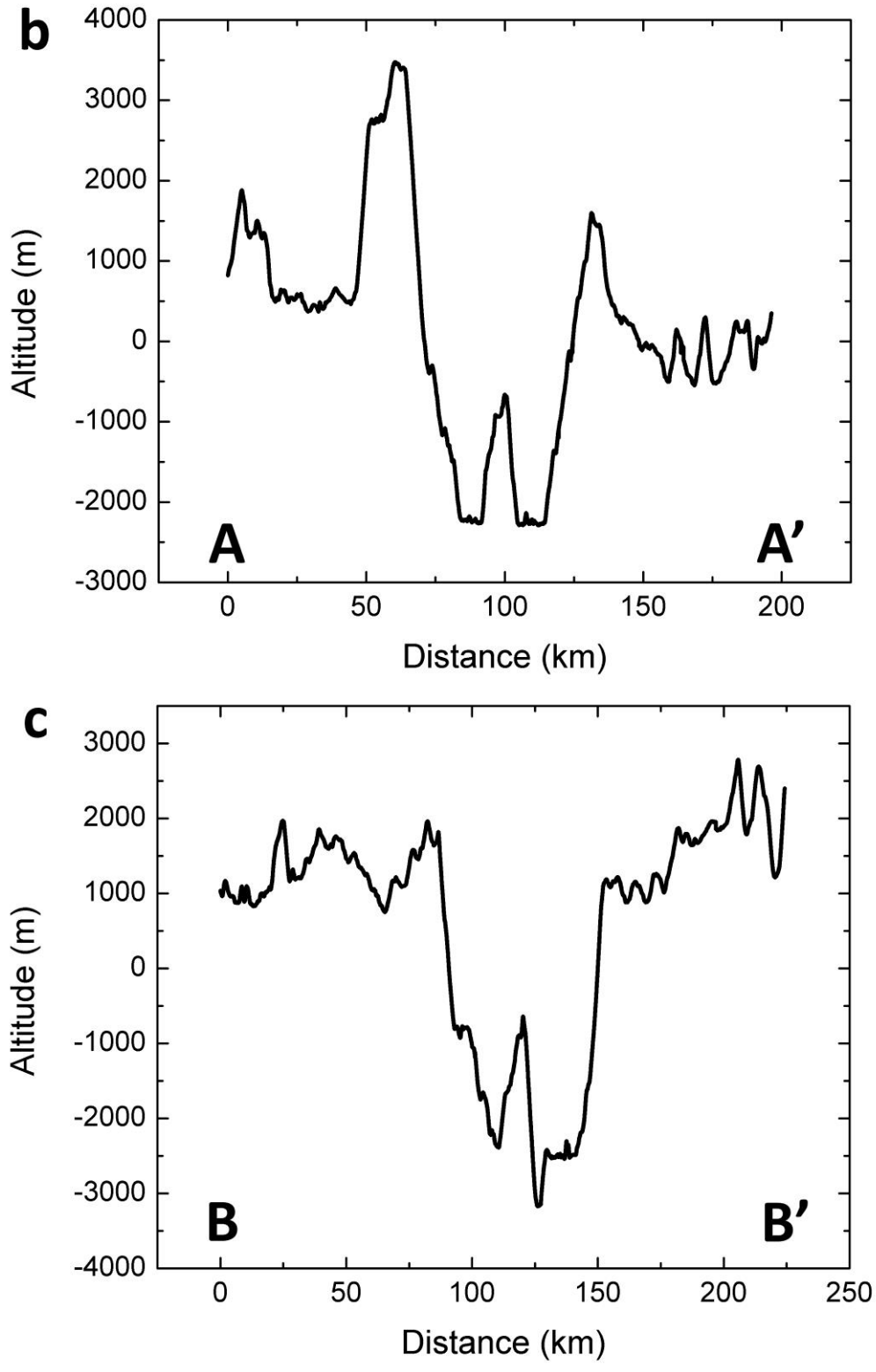
b
4000
3000
2000
1000
0
-1000
-2000
-3000
Altitude (m)
A
A'
0
50
100
150
200
Distance (km)
c
3000
2000
1000
0
-1000
-2000
-3000
-4000
Altitude (m)
B
B'
0
50
100
150
200
250
Distance (km)

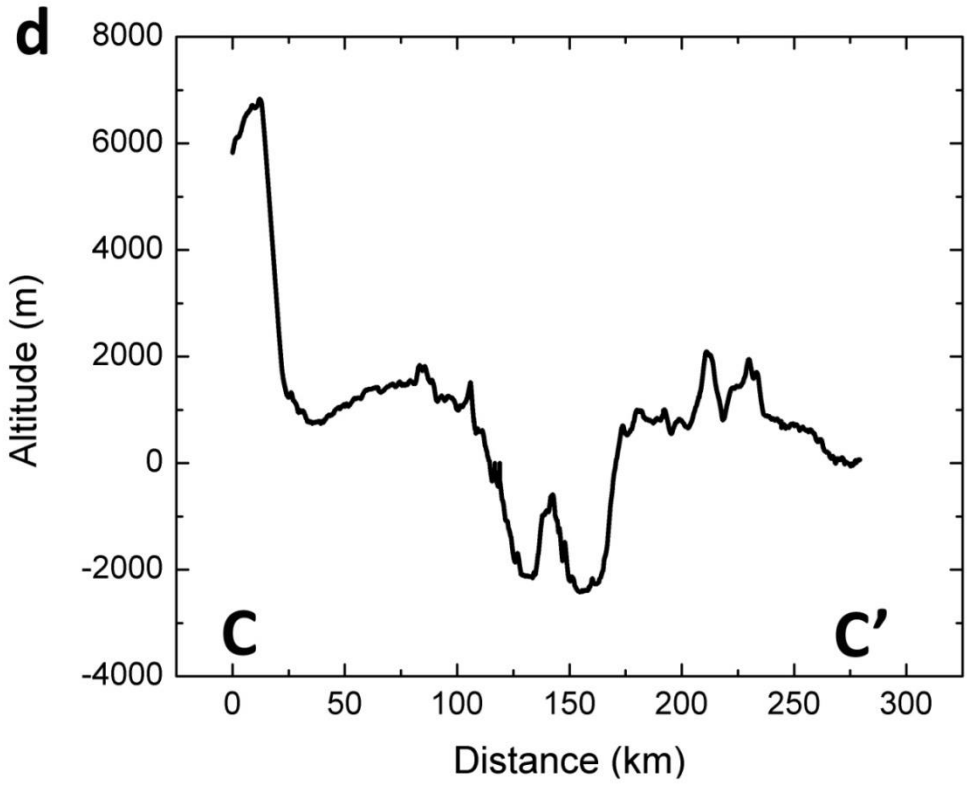
d
8000
6000
4000
2000
0
-2000
-4000
Altitude (m)
C
C'
0
50
100
150
200
250
300
Distance (km)

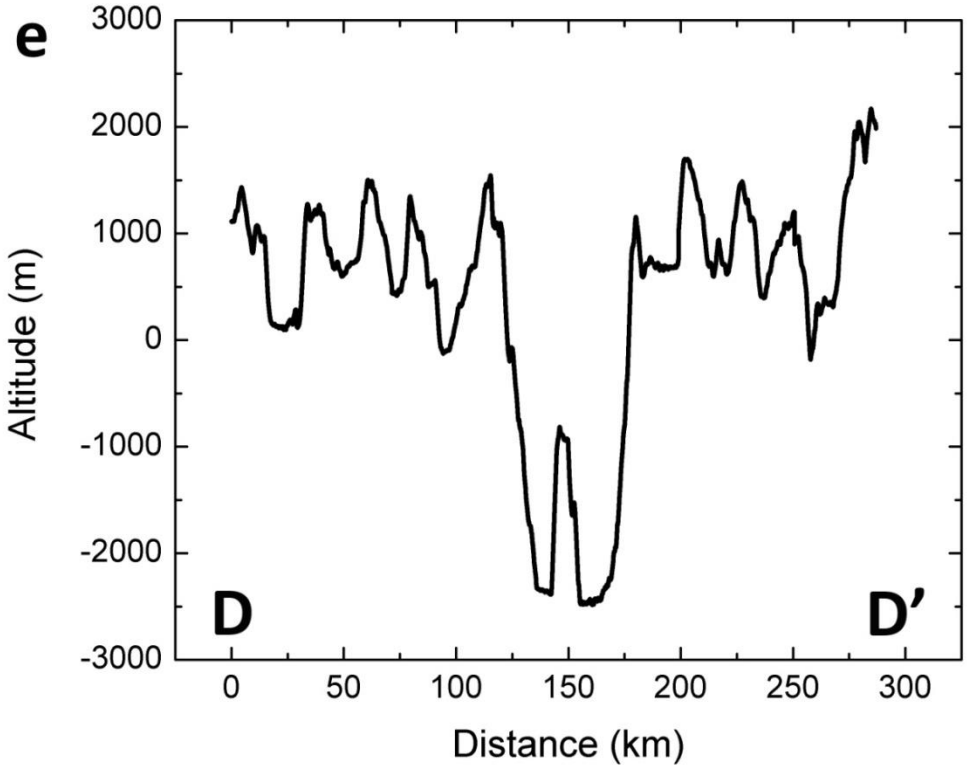
e
3000
2000
1000
0
-1000
-2000
-3000
Altitude (m)
D
D'
0
50
100
150
200
250
300
Distance (km)

Table 5.1 Selected morphometric parameter estimates for Lowell crater and Crater S determined from TC DTM and topographic sections plotted in Fig. 5.2 b-e. Here, X indicates that the respective parameter value could not be determined from the cross-section.

Morphometric Parameter	**Estimated value from cross – sections**	**Average**
Lowell crater diameter	AA': X BB': 67.5 km CC': X DD': 64 km	~67.83 km
Lowell crater depth	AA': X BB': 3.50 km CC': 1.87 km DD': 3.65 km	~3.00 km
Lowell rim height	AA': X, 1.80 km BB': 0.88 km, 0.20 km CC': 0.40 km, 0.25 km DD': 0.87 km, 0.50 km	
Lowell rim wall slope	AA': X (N), 12.26^{o} (S) BB': 10.34^{o} (W), 15.20^{o} (E) CC': 8.92^{o} (SW), 14.39^{o} (NE) DD':10.56^{o}(NW), 12.98^{o} (SE)	
Lowell floor diameter	AA': 27.5 km BB': 32 km CC': 33 km DD': 29 km	~30.37 km
Lowell floor area (including central peak area)	974.40 km^2	
Height of central peak	AA': 1.60 BB':1.87 CC': 0.90 DD': 1.75	~1.53 km
Basal area of the central peak	~157 km^2	
E-W diameter of Crater S	~9.35 km	
Crater S depth from western and eastern rim	~0.08 km (W) ~3.2 km (E)	
Area of Crater S	~63.56 km^2	
Floor area of Crater S	~5.76 km^2	
Total area (Lowell crater + Crater S)	~3422 km^2	

5.3 Morphological units

As evident from section 5.2, the Lowell crater can be broadly divided into rim and crater wall area, central peak area, crater floor area and ejecta blanket. These are described in the following sub-sections.

5.3.1 Rim and crater wall area

The rim of a crater defines the lateral extent of the inward slumping during the modification stage of a cratering process subsequent to the excavation stage, which initially would have resulted into the formation of a smaller transient cavity. The rim in Lowell's case is sharp and polygonal in shape. The pre-existing topography, structural features and post formation major impact event appear to have affected the present day appearance of the rim. For example,

- the northern apex shows a distinct discontinuity due to presence of a pre-existing peak
- the northwestern part shows an eye-shaped bulge due to enhanced slumping possibly due to convergence of pre-existing lineaments
- the southwestern part shows an inward humps due to presence of the pre-existing craters
- the southeastern rim shows distorted outward bulge due to the formation of Crater S

The crater wall is broader on the western side compared to the eastern part due to enhanced slumping on the western side during the modification stage (Fig. 5.3). This could be related to pre-existing topography and/or the nature of the Lowell forming impact i.e. direction and angle of impact. The walls show prominent slump terraces and at places show rhombic appearance (rw in Fig. 5.4) due to cross-cutting of the terraces by mostly north and northwest trending pre-existing lineaments, which could be related to the global lunar grid and/or to the formation of the Orientale basin.

In addition to these, prominent post cratering slump zones have also been noticed on the walls of the Lowell crater (e.g. sz in Fig. 5.3). Pre-existing weaknesses and surface topography appears to have promoted the formation of such zones. For example, a

prominent slump zone occurs at the intersection of the Outer Rook Ring and the southeastern rim of Lowell crater (sz in Fig. 5.4). Similarly, another pronounced slump exists at the northern apex, possibly due to the presence of ~3 km high pre-existing peak at the apex of the crater.

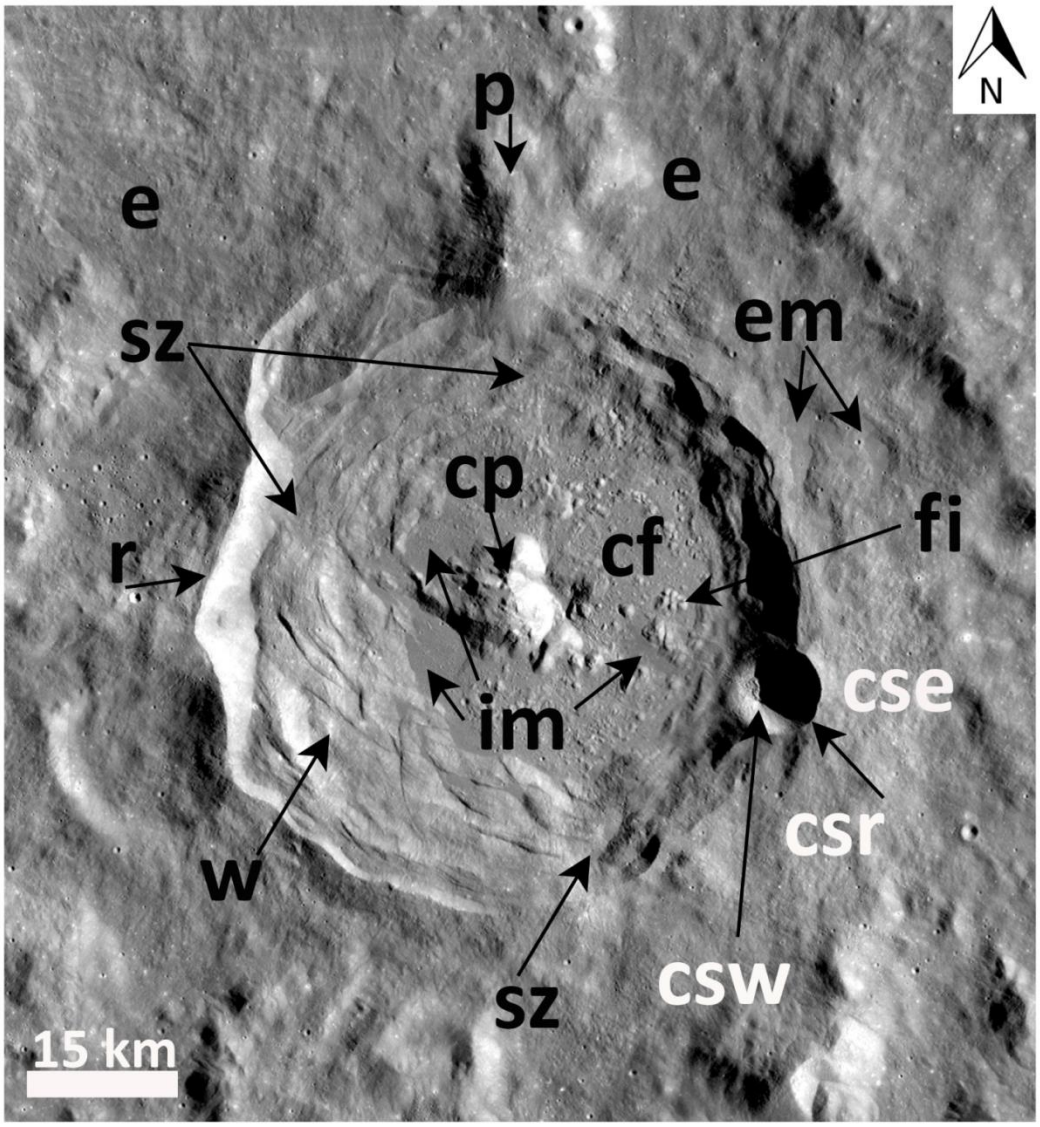

Figure 5.3 A LROC-WAC image mosaic showing morphological features of the Lowell crater and superposed Crater S. These are marked as cp: central peak; cf: crater floor; w: wall; r: rim; e: ejecta; im: inner melts; em: exterior melts; sz: slumped zones; si: floor irregularities and p: pre-existing uplands. cse, csr and csw refer to the ejecta, rim and wall of the superposed Crater S.

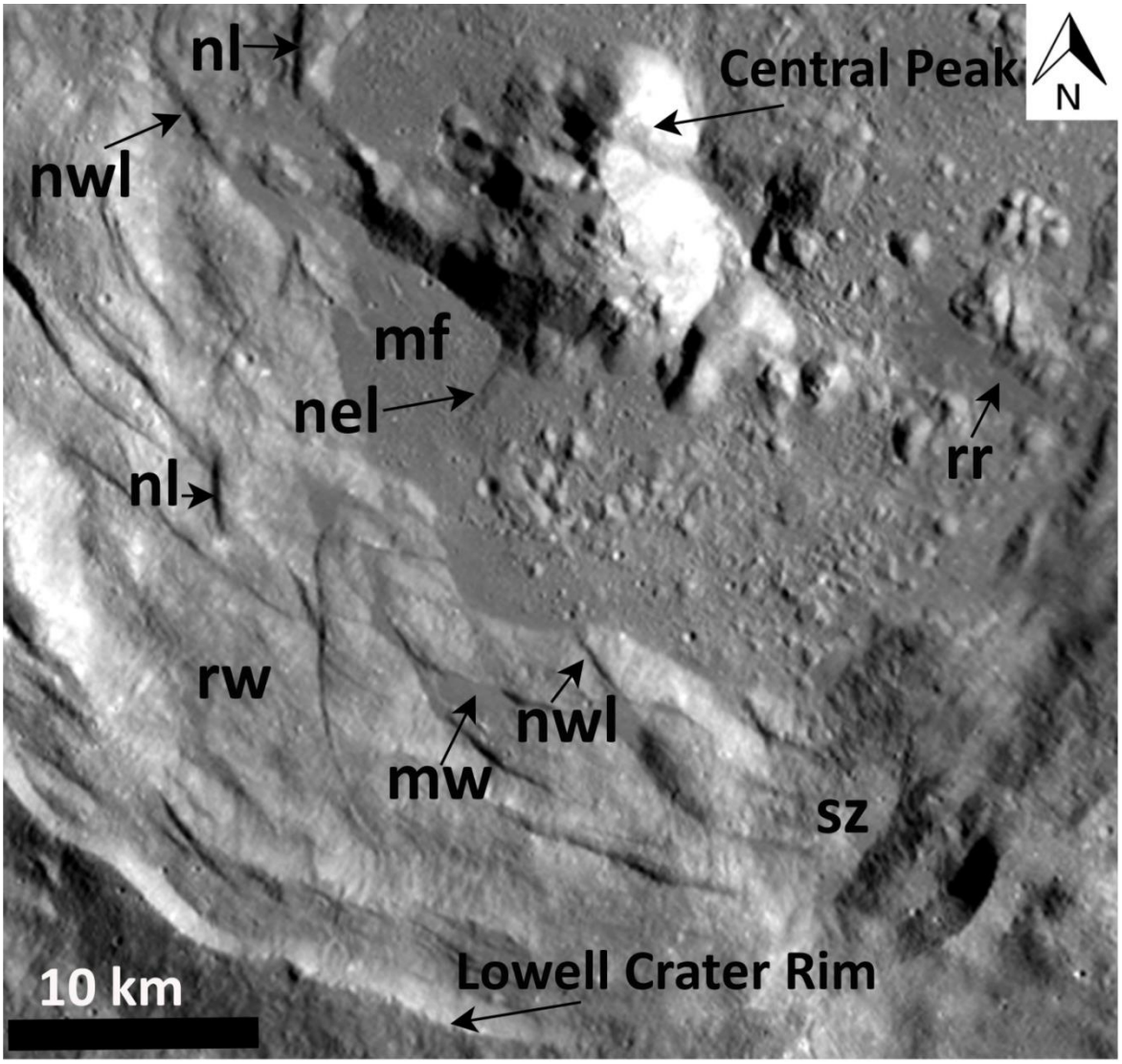

Figure 5.4 A zoomed view of a part of the Lowell crater (from mostly southwestern part) from LROC-WAC data showing detailed morphology of the central peak, the terraced crater wall, and the crater floor. Here, nl, nwl and nel refer to north, northwest, and northeast trending lineaments respectively. Other notations refer to– rw: rhombic sections on the wall; sz: slump zone on the wall; mp: melt pool on the central peak; mw: melt pool on the wall; mf: melt pool on the floor; rr: recent resurfacing.

Among the inner melts (im in Fig. 5.3), small pools of impact melts are present in topographic lows of the wall (e.g. mw in Fig. 5.4), comparatively larger ones on the Lowell crater floor (mf in Fig. 5.4 and 5.5), and the recent resurfacing composed of distinct fresh channelized flows that emanate from the superposed Crater S on the western Lowell wall and descend down on to the floor of the Lowell crater (rr in Fig. 5.4 and Fig. 5.5). A

detailed description of the morphology, composition, age and origin of these channelized flows is provided in section 5.4 and chapters 6-8.

5.3.2 Central peak area

Central peaks or the central upland area is characteristic features of complex impact craters. They also form during the modification stage of the cratering process and are a result of elastic rebound and inward slumping. They are understood to have exposed rocks from maximum depth in an impact crater, therefore are very important for stratigraphic studies on the Moon using remote sensing (e.g. Tompkins and Pieters, 1999; Srivastava, 2008).

In case of Lowell crater, the central peak covers an area of ~157.08 km^2 and rises to a maximum elevation of ~1.87 km above the average level of the Lowell crater floor. A zoomed view of the central peak in Fig. 5.5 shows a small melt pool at the apex of the central peak (mp) and a prominent, approximately 'V' shaped high albedo slumped zone (sz) at the eastern flank of the central peak. The western part exhibits an elongated limb extending almost up to the Lowell crater wall (sp). Patches of ~10-50 m boulders have been noticed at several sites on these central uplands. An expanded view of one such occurrence on the central peak in the northeast part, marked as 'bo' in Fig. 5.5a, is shown in the Fig. 5.5b.

5.3.3 Crater floor area

The crater floor area represents area between the central peak and the crater wall. Most of the impact melts formed during the impact cratering process are retained within the crater, typically occupying the low lying areas of the crater floor. Their texture mainly depends upon the area they occupy and the clastic content within them**.** A close look at the Lowell crater floor reveals presence of smooth interconnected melt pools on the western side and a plausible large melt pool occupying most of the low lying areas in the northeastern part (Fig. 5.3).

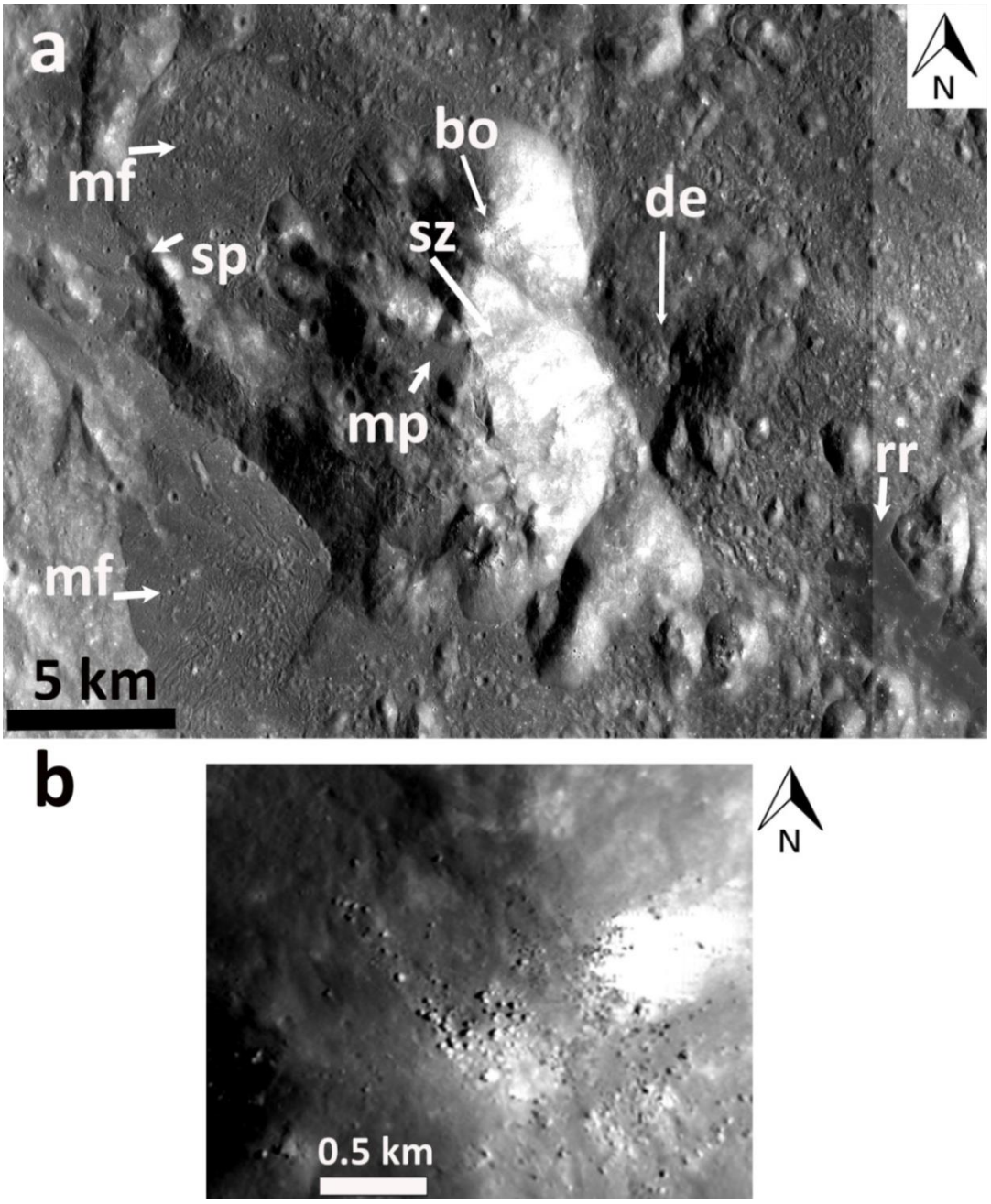

Figure 5.5 a) A zoomed view of the Lowell crater floor from TC image mosaic showing central peak area, melt pools on the floor (mf) and a part of the recent resurfacing (rr). Here mp, sz, and bo refer to melt pool, slump zone and boulders on the central peak respectively. Other notations refer to- sp: splinter connecting central peak with crater wall; de: deepest area on the crater floor; b) A zoomed view of the location marked as bo showing boulders spread over the central peak.

The smaller melt pools show relatively smooth appearance and exhibit characteristic flow features such as channels, flow lobes, cooling cracks and pits (Fig. 5.5). The plausible larger one exhibits presence of numerous floor irregularities which are understood to be broken target leftovers during the cratering process. Some of these floor irregularities are aligned along the crater wall in the form of an arcuate chain. A few irregularities or mounds are also present in the southeastern part of the crater floor, however, they are distinctively absent in and around the western side melt pools.

The central part of the eastern floor shows extension of the fresh channelized flows descending through the Lowell crater wall and terminating almost midway between the crater wall and the central peak. The deepest region of the Lowell crater (~600 m below the Lowell floor, marked as de in Fig. 5.5) occurs in line with these flows just next to the marked 'V' shaped slumping on the central peaks. It is prominently seen in the W-E topographic profile BB' (Fig. 5.2a, c).

5.3.4 Ejecta blanket

Impact ejecta refer to the target materials irrespective of their physical state that are transported away from the transient cavity rim by ballistic sedimentation and radial flows (Osinski et al., 2011). Therefore, in complex craters where late stage inward slumping is pronounced, ejecta deposits also occur in the rim area inside the final crater rim. The ejecta are classified into proximal and distal ejecta based upon their distance of occurrence from the final crater rim. The proximal ones refer to the material that fall near to the crater up to ~5 crater radii, beyond which, they are termed as distal deposits. The proximal ejecta up to ~1-2 crater radii generally show a continuous nature, therefore, is termed as continuous ejecta blanket. Further away, the texture of the ejecta material is patchy and discontinuous (Melosh, 1989).

In case of the Lowell crater, the panchromatic images do not show prominent rays similar to the ones seen in other highland craters of Copernican age such as Tycho, Jackson etc. Further, ray pattern, if present in this case, is complicated by rays from the fresh superposed Crater S on its eastern rim and also due to rays emanating from a fresh crater on the nearby Cordillera scarp in the northwestern direction (marked as A in Fig. 5.1).

Similar observations have been made by McEwen et al. (1993) concerning the role of superposed crater on the Lowell rim. In light of this, a definitive age of the Lowell crater is difficult to establish (a detailed discussion is provided in chapter 7).

In this study asymmetric exterior ejecta pattern up to ~2 crater radii from the Lowell crater rim has been observed and mapped using LROC-WAC data and photometrically corrected M^3 750 nm data (Fig. 5.2 and Fig. 17). It constitutes of a mildly low albedo sheet of ejecta material that extends in the northwest region and in the northeast parts, separated by a string of pre-existing uplands commencing at the northern apex of the Lowell crater. The ejecta emplacement appears to be partly controlled by the local topography. On the southern side, the extent of these deposits is comparatively less and is confined mostly to the near rim region. The continuous ejecta if at all present in the southeastern part would have been now superimposed by the ejecta from Crater S.

Numerous smooth exterior impact melt pools have also been identified occupying local depressions, however, all the identified ones lie in the northeast part within ~1 crater radii from the rim of the Lowell crater (em in Fig. 5.3). These pools are characterized with flow features such as pits, channels and ridges.

5.4 The fresh resurfaced unit

5.4.1 Gemorphology

The geologic context of the recent resurfaced unit with reference to the nearby basaltic areas Mare Orientale and Lacus Veris is shown in Fig. 5.6. The recently produced prominent resurfacing extends ~17 km inwards from the superposed Crater S, ~9 km in diameter, near to the eastern rim of the Lowell crater. The Kaguya TC images revealing the extent and geologic context of the recent flows inside Lowell crater and the MI-VIS image view of a part of the resurfacing depicting morphological details are shown in Figures 5.7 and 5.8 respectively. The topographic profiles for the unit derived from TC DTM are shown in Fig. 5.9 a-b.

The fresh resurfaced unit occupy ~64 km^2 area and is confined to a nearly linear channel which is ~3-6 km wide and ~100 m deep (e.g., section AB in Fig. 5.9b) and is

superposed on older flows emanating and diverging from Crater S (Fig. 5.7 and 5.8). A lower limit to the estimated volume for these fresh flows could be ~0.96 km^3, considering average thickness of ~15 m which is largely the observed thickness of the flows at the terminus of the unit. It has an average slope of ~4.5^0, with steep portions in the Lowell crater wall (section CD in Fig. 5.9b).

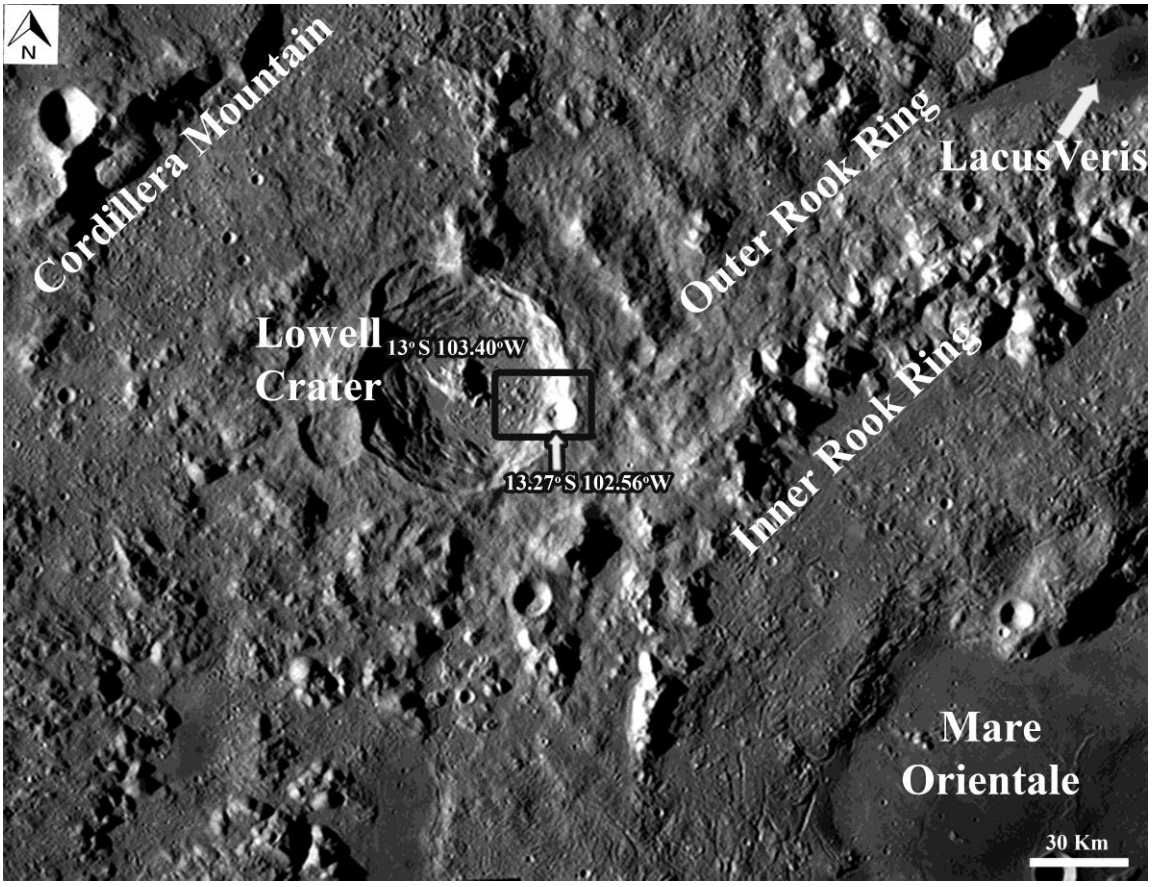

Figure 5.6 LROC-WAC image mosaic showing regional geologic setting of the recent resurfacing (enclosed within black coloured rectangle) with respect to the nearby basaltic regions (Mare Orientale and Lacus Veris), Crater S (also enclosed within the rectangle), and the host Lowell crater. Geographical co-ordinates of centre of the Lowell crater and Crater S is marked [Source: WAC mosaic from wms.lroc.asu.edu]

At the floor of Crater S lies a small conical uplift with a melt pond at the summit (Fig. 5.8 and Fig. 5.13). The surface of the pond shows a cluttered appearance and is composed of rock debris and melts showing wide cooling cracks. Numerous fresh viscous flows showing distinct outline and unperturbed flow fronts have emerged from it

descending through the walls of the Lowell crater (Fig. 5.8 and Fig. 5.10). These resemble "Pahoehoe" lava in terrestrial settings and show presence of prominent median channels.

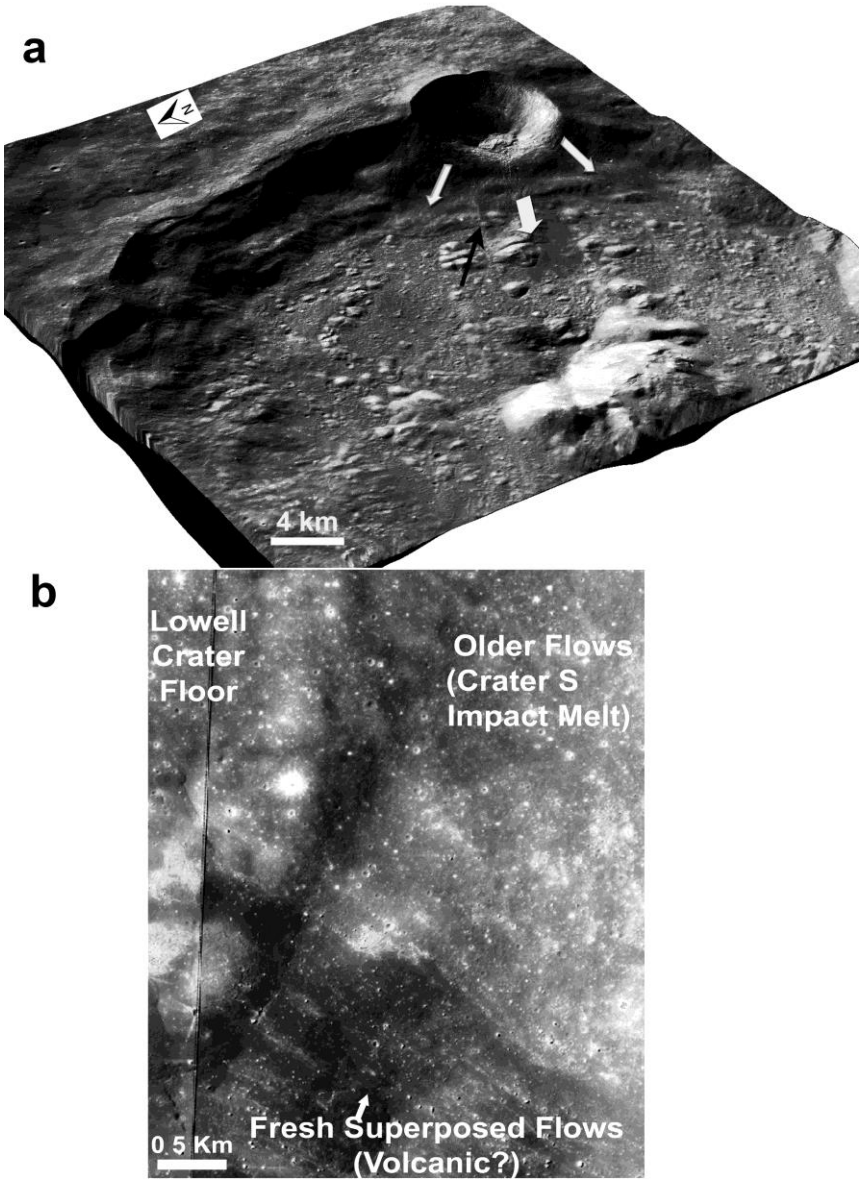

Figure 5.7 a) A 3D view from TC data DTMTCO_03_02785S129E2573SC showing the extent of old melts that originated and diverged from Crater S and the fresh resurfacing under consideration here following a rectilinear trend. The older flows are marked with thin white arrows and the comparatively fresh ones are indicated by thick central arrow; b) A zoomed view of the juxtaposition of these melts at the Lowell crater floor shown with black arrow in sub-section a.

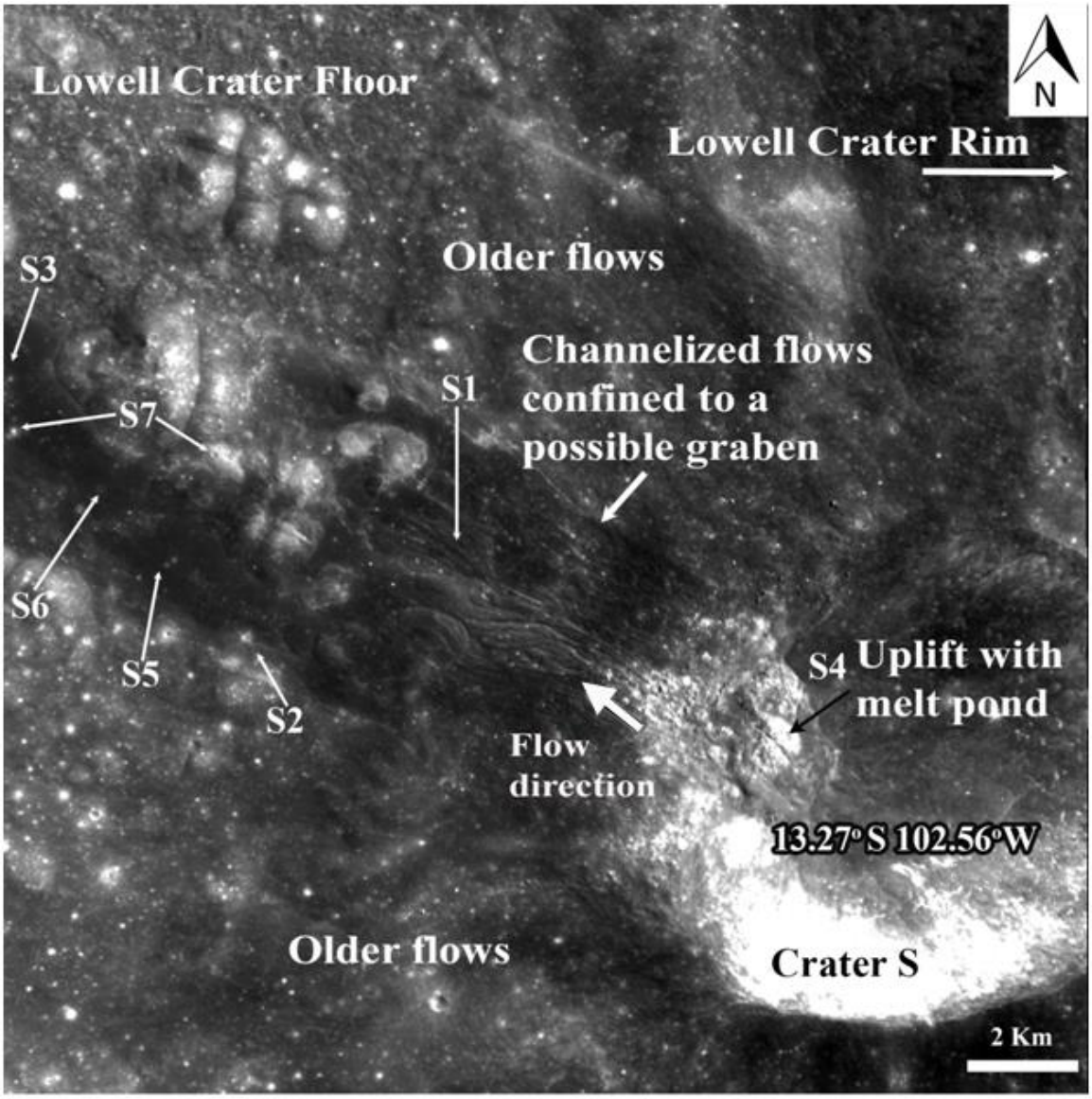

Figure 5.8 Kaguya's MI-VIS data MVA_2B2 _01_0 2 452S132E2573 of a part of the Lowell crater showing morphology of a part of the resurfaced area shown in Fig. 5.7. Enlarged LROC-NAC views of the regions marked as S1-S7 are shown in Figures 5.11-5.17.

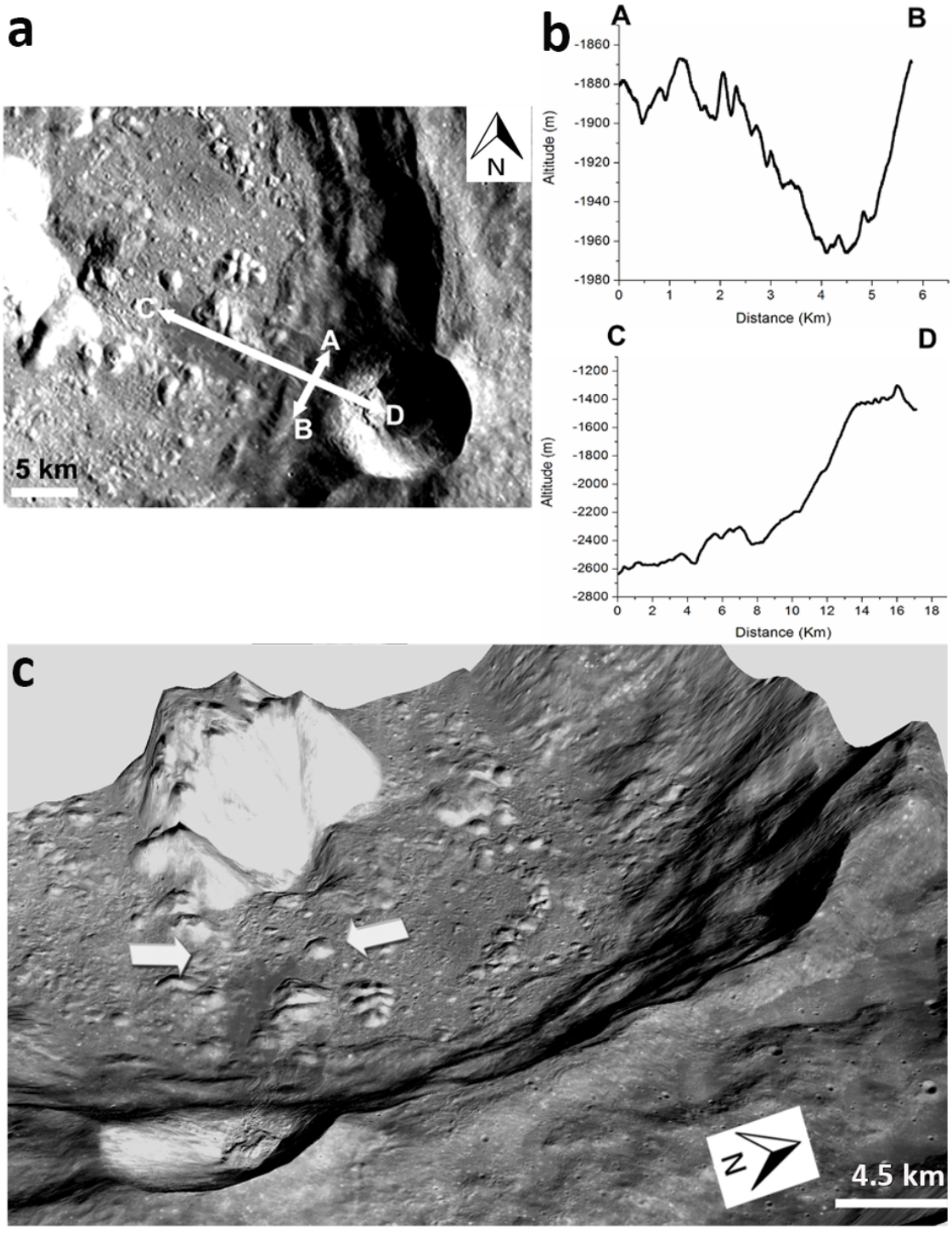

Figure 5.9 a). Kaguya TC data (DTMTCO_03_02785S129E2573SC) showing transects along which topographic profiles have been derived; b) Tropographic sections along AB and CD**;** c) A peak facing view (vertical exaggeration: 7) showing expression of the proposed graben in Lowell crater central peak resulting in subsidence and slumping.

Further down, on the Lowell crater floor (Fig. 5.11), at least three episodes of superposed flows can be identified. The oldest of these (flow 1) shows low albedo, smooth surface, only very sparse impact craters and linear alignment of rock fragments along the margin of the channel. It is less viscous in comparison to the two younger superposed ones (flow 2 and flow 3) which show smooth but lower albedo surfaces, well developed lobes due to their high viscosity and are devoid of any obvious primary impact craters. Only a few small craters/pits with diameter ranging from 10-80 m showing small central uplift or conspicuous depression and meter to decimeter sized wide fresh cracks are seen on their surface (Fig. 5.15). A distinct crater, ~135 m in diameter, showing conspicuous rock cluster surrounding it and extrusion of melts, is located on a surface mound on the channel floor (Fig. 5.16).

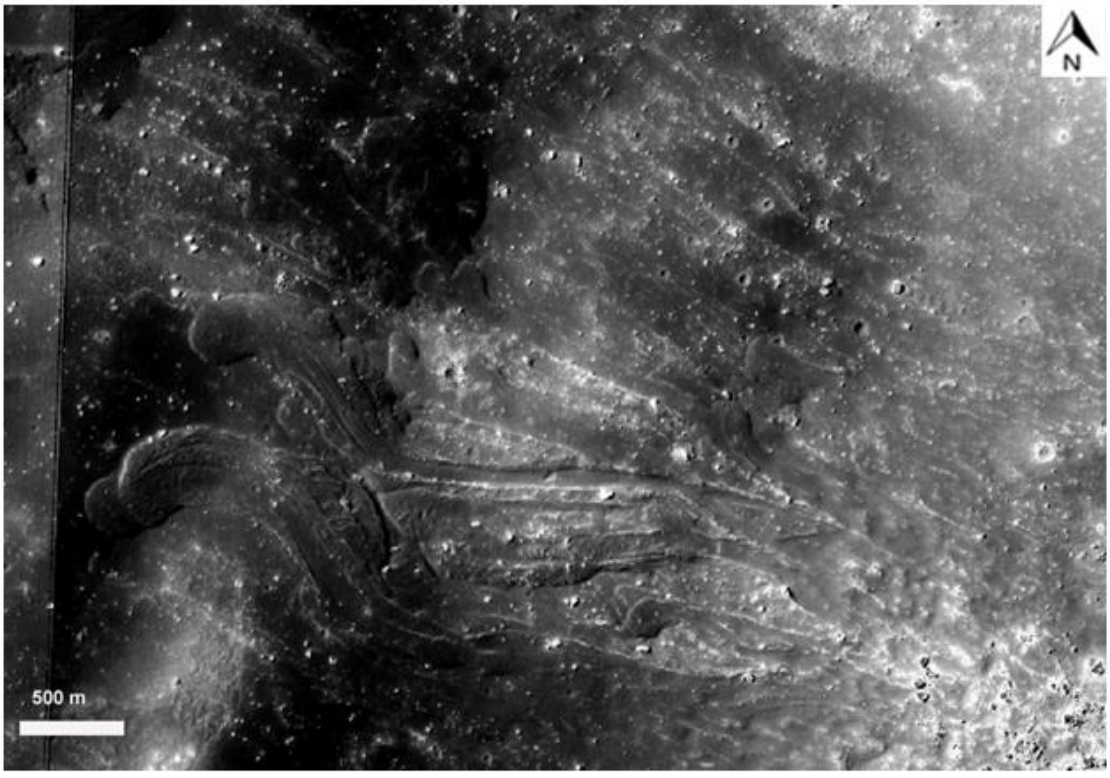

Figure 5.10 An enlarged view of the "Phaoehoe" lava like flows descending through the wall of Lowell crater [from LROC-NAC data M184196652 (LE&RE)]. Prominent median channels and superposed flows are evident in the scene.

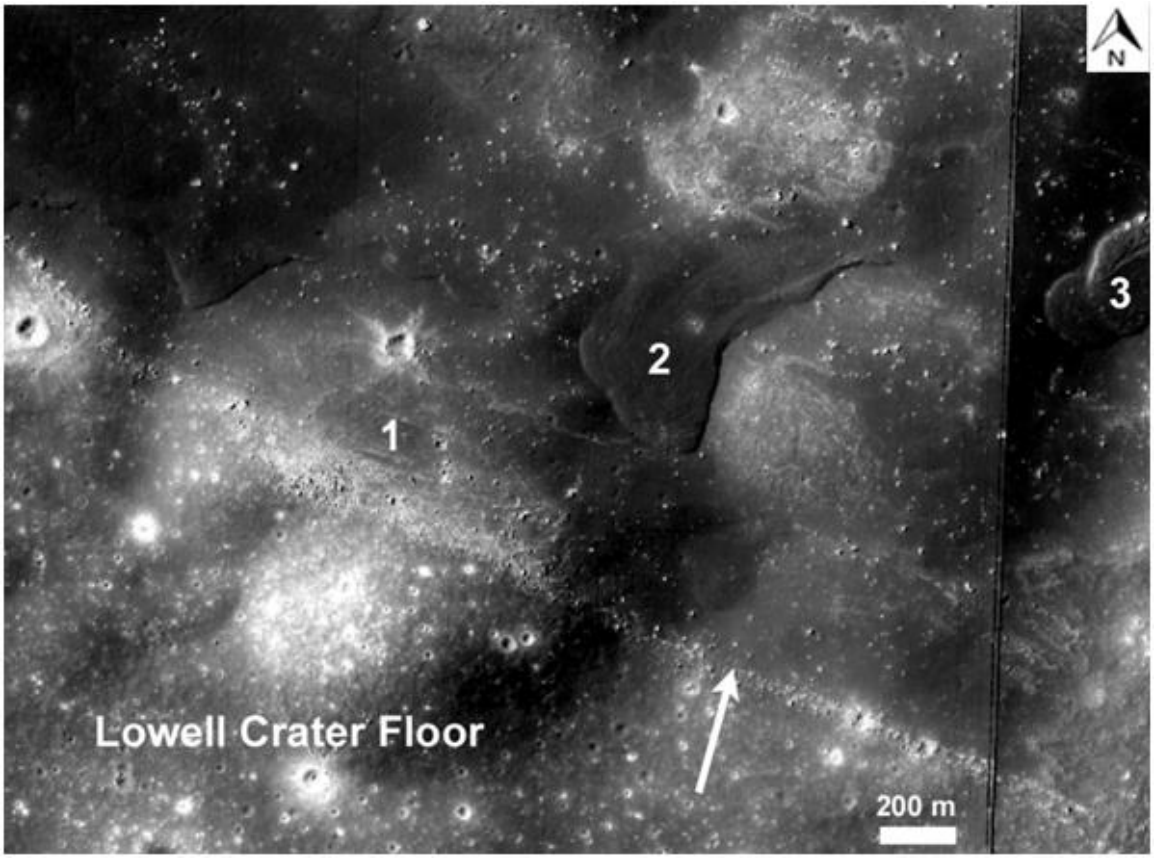

Figure 5.11 A portion of the resurfacing from LROC-NAC data M184196652 (LE and RE) showing a minimum of three generations of flows marked by 1, 2 and 3. Flow 1 represents the oldest and the least viscous ones followed by 2 and 3 which show well developed lobes due to higher viscosity. The white arrow shows boulders that got linearly aligned along the margin of the channel during flow 1. A distinct crater density contrast between the Lowell crater floor and the resurfacing is evident.

Further, towards the terminus of the resurfacing, a minimum of eight ~100 m wide craters/pits have been identified which are subdued in nature and are devoid of ejecta blanket and rays. The smaller craters are absent in the adjoining areas suggesting that they might be possibly covered with recent flows (Fig. 5.15). Thus, these depressions or craters might be expressions of craters/ pits formed on the pre-existing surface now lying buried under the fresh flow. Two polygonal craters are also present in this area which shows failed wall, asymmetric ejecta distribution and extrusion of melts (Fig. 5.16). In particular, the fresh resurfacing has a rather smooth surface compared to the older flows in adjacent areas

and the host Lowell crater floor which are filled with numerous small impact craters (Fig. 5.7, Fig. 5.8, and Fig. 5.11).

5.4.2 Mechanism of formation

Melt formation and its subsequent flow and accumulation in and around craters are a natural outcome of cratering from hypervelocity impacts on a planetary surface. They are basically recognized as low albedo resurfacings normally associated with impact craters and impact basins. The quantity of melts produced, their composition and distribution basically depends upon size and velocity of the impactor, the angle of impact and target characteristics (e.g. Pierazzo and Melosh, 2000).

On the Moon, since low albedo mare basaltic plains are also mostly associated with impact basins (e.g. Orientale Basin (Whitten et al., 2011)) and occasionally with craters (e.g. Tsiolskovsky (Pieters and Tompkins, 1999)), sometimes it is difficult to differentiate between basalts and impact melts using remote-sensing data. For young flows associated with Copernican impact craters such as Giordano Bruno, King, Tycho, Aristarchus etc., sometimes the observed flow morphologies are also similar to those produced by "Phaoehoe" lava flows in terrestrial settings (e.g. Strom and Fielder, 1968, 1970; Heather and Dunkin, 2003; Bray et al., 2010; Chauhan et al., 2012; Denevi et al., 2012). Therefore, deciphering their explicit origin is a difficult task and the issue has been aptly debated.

The volcanic theory cites crater count differences between some of the resurfacings and the host crater surface as the key evidence for post impact volcanic modifications of these recently formed craters (e.g. Strom and Fielder, 1968, 1970). However, evidences such as (a) lack of unambiguous melt sources, (b) proximity in distribution between melt and ejecta, and (c) the conventionally accepted idea of cessation of volcanic activity on the Moon prior to ~1 Ga, have been cited in support of an impact melt origin for various resurfacing flows with a fresh appearance (e.g. Howard and Wilshire, 1975; Hawke and Head, 1977; Denevi, et al., 2012).

Data from recent remote sensing missions such as Kaguya, Lunar Reconnaissance Orbiter (LRO) and Chandrayaan-l have revealed new details about the crustal structure and magmatic history of the Moon, through identification of fresh thrust faults across the Moon

(e.g. Watters, et al., 2010), extended volcanism on the far-side (Haruyama, et al., 2009; Jolliff, et al., 2011), spinel dominant dense crustal rocks at several locations (e.g Pieters, et al., 2011), and young mare units in the Orientale basin (Whitten, et al., 2011; Cho, et al., 2012).

Further, re-analysis of Apollo seismic data and experimental studies using lunar samples and simulations have deduced a partially molten lower lunar mantle and the core (Weber et al., 2011; Parker et al., 2012). Considering these recent advances in the understanding of lunar geology, possibilities for the occurrence of very young volcanic flows also exist on the Moon in favorable geologic settings such as in an extensional environment. Therefore, fresh resurfaced units on the Moon's surface need to be carefully investigated to decipher their origin (Srivastava et al., 2013).

Broadly there could be two plausible scenarios for the formation of the recently resurfaced unit under consideration in this study. Either it could be composed of impact melts formed during the Lowell/Crater S impact event, or alternatively it may be related to some sort of late stage volcanic activity, which would have occurred in the region subsequent to the formation of Crater S. The likelihood for the formation of the unit from impact melts formed during Lowell impact event appear minimal, as distinct crater density contrast has been observed between the resurfacing and the other areas of the Lowell crater floor (Fig. 5.11 and Fig. 5.12). Even the other resurfaced areas inside the Lowell crater show numerous small craters in contrast to the resurfacing discussed in this study. Further, several impact craters have also been observed on the older melts emanating from Crater S, its ejecta blanket and along its rim, suggesting that it could also be relatively older in age (Fig. 5.7).

However, because at present there are uncertainties in the understanding of crater density difference between impact melts and other surfaces (Ashley et al., 2012) and the fresh flows appear to directly emerge from Crater S, here, 'Crater S impact melt scenario' versus 'recent volcanic preposition' for the formation of the recently resurfaced unit has been evaluated based on the observed surface features on the resurfacing.

Figure 5.12 A juxtaposition of the resurfacing (right) and an adjacent area on Lowell crater floor (left) from LROC-NAC data M105192594RE showing contrast in crater density.

a. Uplift with melt pond at the summit

The structure could have formed due to stacking of impact generated debris produced during the formation and failure of Crater S, against the Lowell crater wall. An alternate mode of formation for the cone resembling structure could be that it could be the primary source region for magma ascent in case the recent resurfacing is of volcanic origin. Lack of evident source has been strongly put forward against volcanic origin of fresh flows on the Moon (Howard and Wilshire, 1975; Hawke and Head, 1977). Here, this plausible source region is lined with pile of boulders possibly pyroclasts and hosts a melt pond with cluttered appearance, thus, making it a candidate for a volcanic vent.

Figure 5.13 A blown-up view of the cone with melt pond at the summit from LROC-NAC data M181844927LC. The raised structure, prominent cracks, cluttered appearance and presence of pyroclastics and/or rock debris is clearly seen.

b. Multiple flows confined to a nearly rectilinear channel

Occurrence of numerous viscous superposed flows with distinct flow fronts and conspicuous lobes require strong continuous influx of melt and flow for an extended period of time. Since production and emplacement of impact melt is typically a splash event following a meteoritic event, it is quite unlikely that the entire unit would have formed due to instantaneous melting and flow of debris subsequent to impact at the Lowell crater edge forming Crater S.

However, presently there are uncertainties in the understanding of the emplacement of impact melts and there are assertions that they could remain mobile for an extended period of time after the formation of the crater (e.g. Howard and Wilshire, 1975; Bray et al., 2010; Ashley et al., 2012)**.** The extension of the viscous flow unit to ~17 km in-spite of high viscosity of the flows and gentle slope on the Lowell crater floor also indicate towards

existence of strong and sustained activity in the region. Further, after emerging from Crater S the impact melts should have spread onto the Lowell crater floor similar to the older melts (see Fig. 5.7 and Fig. 5.8).

Here fresh flows (Flow 1, Flow 2 and Flow 3 in Fig. 5.11) have been observed that are almost confined to an approximately rectilinear channel about ~100 m deep (see section AB, Fig. 5.13) and ~17 km long. This suggests that the unit is flowing along a lineament, possibly a graben-like structure. Therefore, there are indications that this may be a volcano-tectonic region (?). A central peak (of the Lowell crater) facing topographic view of the region (Fig. 5.9b) reveals expressions of the plausible graben in the peaks, where subsidence and slumping has occurred.

c. Depressions with positive relief or conspicuous low at their centre

Such depressions varying from ~10-80 m in diameter have been identified in the viscous layer flow 2. A prominent cluster occur almost mid-way in the unit (Fig 5.14). The two larger depressions (~80 m diameter) show higher disturbance and negative relief at their centre compared to the smaller ones that are less disturbed and show positive relief at their centre. These resemble tiny analogues of commonly found bench craters/concentric craters on the Moon's surface. The origin of such craters is debated, and both impact and volcanic origin have been proposed for their formation (Senft and Stewart, 2007; Wood, 1978).

The pre-requisite for their origin from impact process is a layered target comprising of a weaker layer such as regolith, overlying a strong layer e.g. basalt. Here, since the host viscous surface is quite fresh, the regolith layer if present may be negligible; however, a basaltic/gabbroic surface overlying harder older impact melts can emulate a similar scenario.

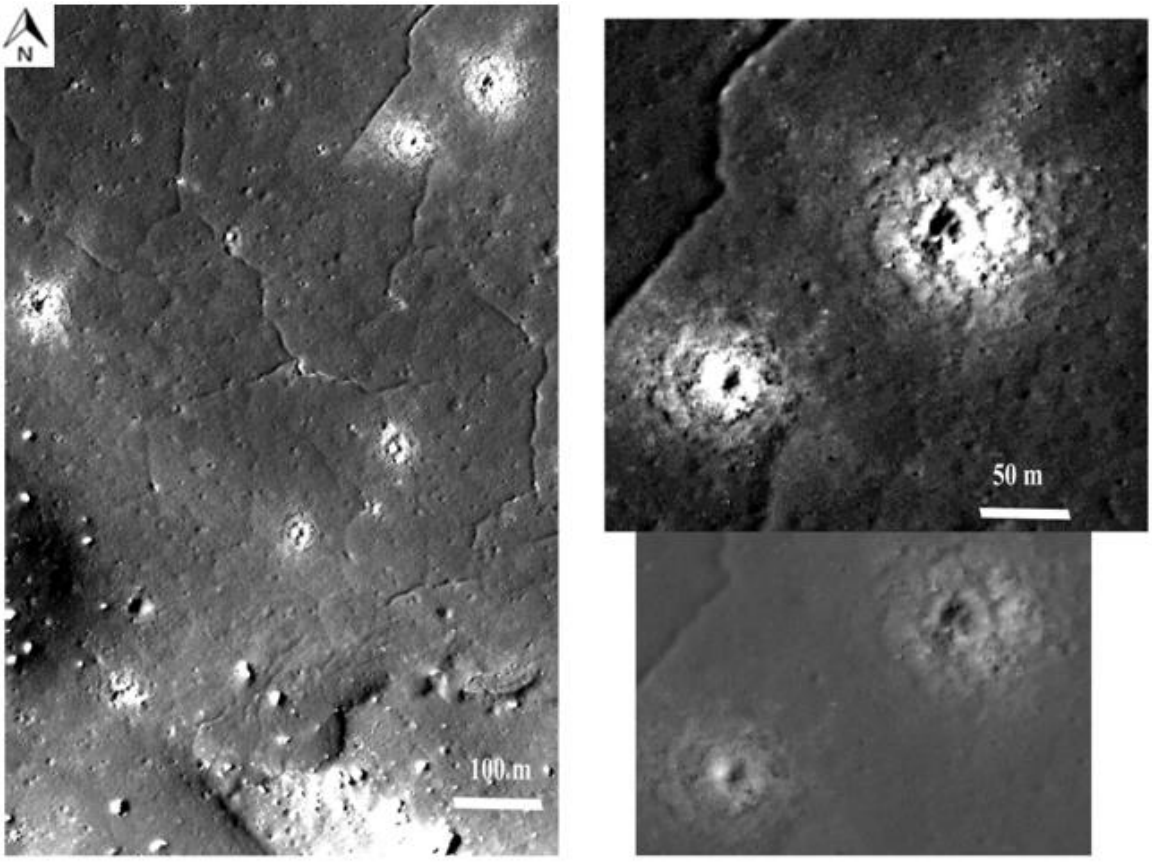

Figure 5.14 (Left) Pits/craters and cracks on the viscous surface from LROC-NAC data M105192594RE. (Right) Enlarged views of the two large ones located at the top right corner (Top: Normal appearance; Bottom: Linearly enhanced view). The right pit or crater shows a swirling depression whereas the left one shows uplift around the centre.

Considering the volcanic scenario i.e., if these were purely volcanic pits, the positive relief could be a manifestation of up-doming due to sub-surface pressure and the depressions could have formed due to collapse and release of pressure either by extrusion of gases and/or melt or their movement into the adjacent sub-surface areas. It appears that some of the slightly larger ~100 m sized craters/pits towards the terminus (e.g. Fig. 5.15) could also have formed due to release of trapped volatiles. This particular possibility is supported by the presence of a high density of smaller vesicle-like features surrounding them. In fact, the density of these vesicles is higher around these craters/pits compared to adjacent areas of the resurfacing.

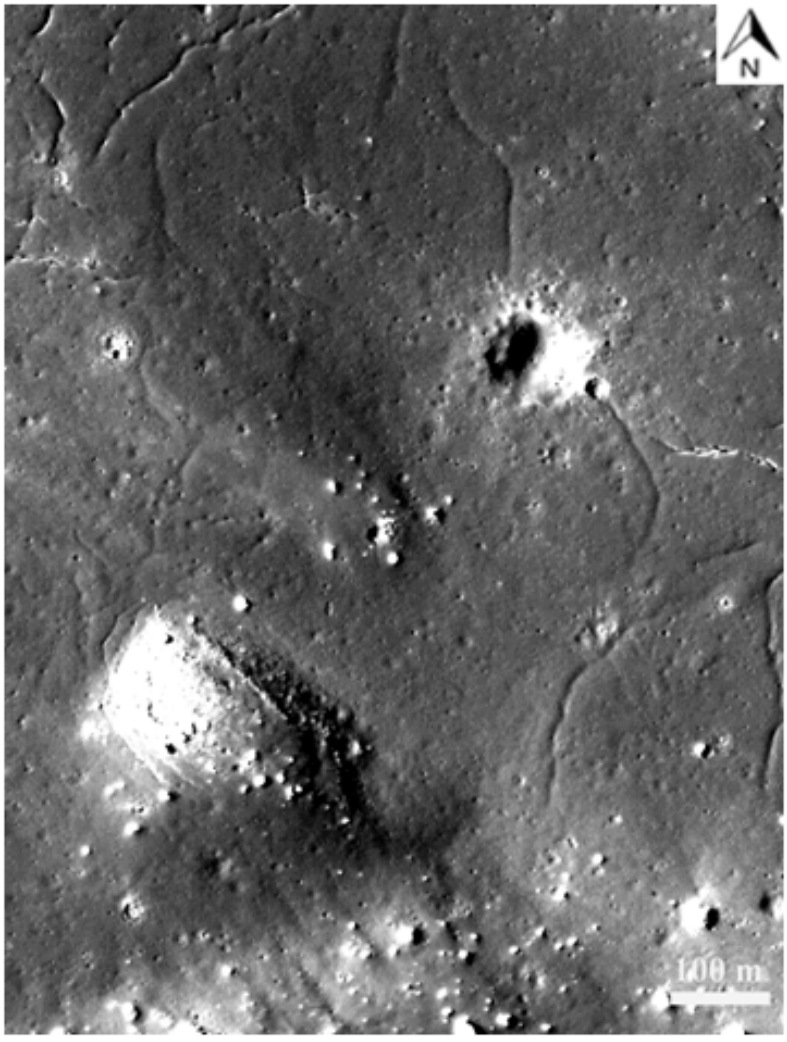

Figure 5.15 A subdued, possibly ghost crater/pit on the resurfacing seen in LROC-NAC data M105192594RE.

Additionally, the other possibilities for their formation could be (a) central up-doming due to presence of rocks and boulders inside the pit/crater, (b) collapse in primary impact craters and, (c) presence of shallow mound diagnostic of secondary craters, similar to the one's shown by Kumar et al. (2011) for larger ones (160-1270 m in diameter). The possibility for the observed craters/pits to be chain of secondary craters is minimal as, contrary to the observations of Kumar et al. (2011), here the larger depressions do not show small uplift at their centre.

Further, under remote circumstances boulders from nearby areas or slumping from the crater wall would have selectively produced the central uplift in the smaller craters/pits

only. As each of the small such pit exhibits similar morphology i.e. a positive relief at their centre and the larger ones, a swirling depression, and both these categories lie adjacent to each other, there is a possibility that these could be intrinsic to the flows. Therefore, indigenous forces might be responsible for producing them and inducing size-dependent differences in their morphology. Thus, several possibilities exist for the formations of these depressions.

d. **Fresh craters showing extrusion of melts**

Three fresh ~100 m diameter craters have been identified within the resurfaced unit, which show extrusion of melts. These include the crater surrounded with rock cluster ~135 m in diameter (Fig. 5.16a), and two polygonal craters of diameter 75 and 95 m with failed walls from which melts and boulders have been ejected (Fig. 5.16b). It may be argued that these could be either tiny primary /secondary impact craters or small volcanic edifices.

The possibility of them being secondary impact craters is only very remote as the energy may not be sufficient to produce melts extruding from them. Even primary craters as small as these are not known to be associated with melt sheets. The minimum size crater generating melt has been reported as 170 m in diameter (Plescia and Cintala, 2012) and these are understood to have been formed due to near-vertical impacts favouring higher melt production. Thus, the three small craters with associated melts observed here are very likely to be small volcanic edifices, and only under extremely rare circumstances these could be possibly impact craters.

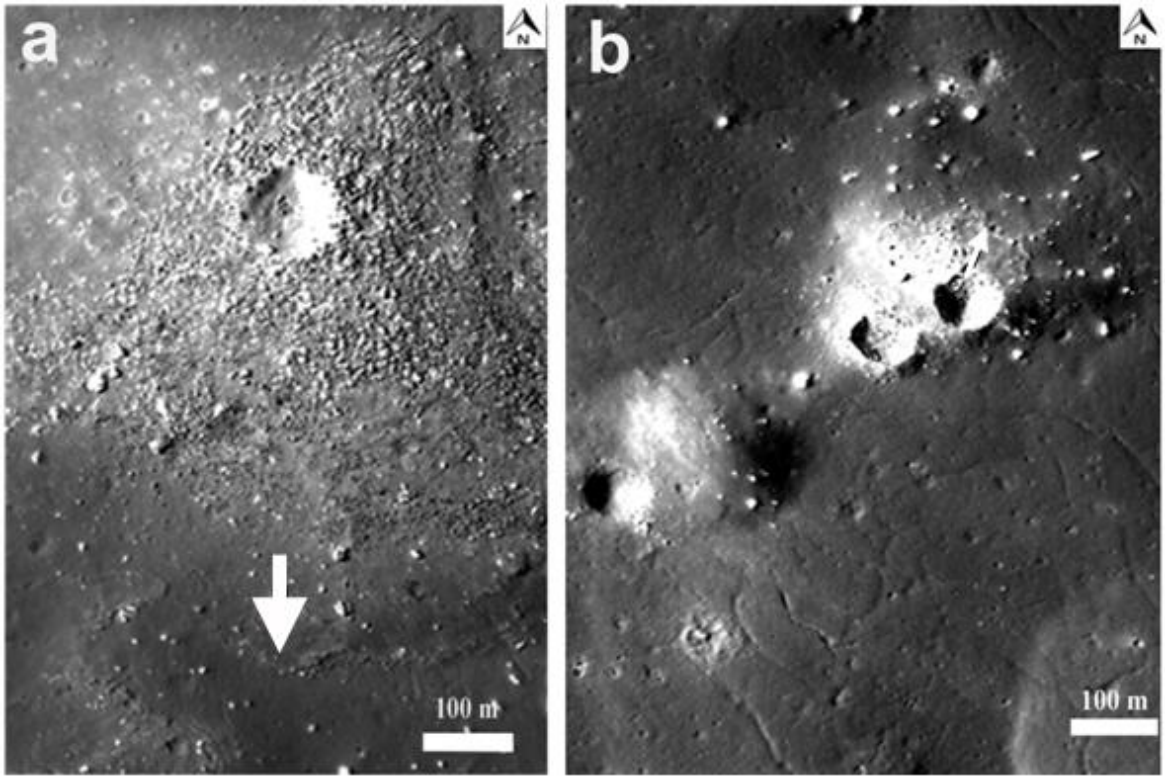

Figure 5.16 a) LROC-NAC data M105192594RE showing a distinct fresh crater surrounded with rock cluster. The arrows points to the flows emanated from them. Few boulders could be seen aligned with these flows; b) Pair of polygonal craters with failed wall as seen in LROC-NAC data M105192594RE. The arrow points towards distinct flows emanating from the crater on the right.

e. Boulders

Boulders have been spotted at several locations throughout the resurfaced unit. These include the ones that are lined along the boundary of the melt pond, embedded within the pond and the flows, stuck on the walls of Crater S and Lowell crater, linearly aligned along the boundary of the resurfacing (Fig. 5.12), and on the floor irregularities lying within the resurfaced unit. Some of these boulders could be debris from Crater S / other recent impact events in the nearby areas or broken fragments from thin draped layer of melt on the floor irregularities or could be pyroclastics resulting from explosive eruptions preceding the plausible volcanic event. Further, high viscosity of the flows also indicates a possible episode of explosive volcanic activity in the region.

Thus, the morphological features of the recent resurfacing emanating from the Crater S and terminating in the central part of the eastern side floor of Lowell crater could possibly be a manifestation of recent volcanic activity in the region assisted by impact events (Srivastava et al., 2013). However, direction association with Crater S, lack of knowledge regarding heat source for magma production during Copernican times and a suitable mechanism for magma ascent imparts severe constraints on the proposed volcanic preposition and needs to be investigated further.

5.5 Summary

Broadly the morphology of the Lowell crater is similar to most of the similar sized complex impact crater on the Moon. However, several peculiarities and/or interesting features have been noticed in the case of Lowell (Fig. 5.3 – 5.16). A few of them are mapped in Fig. 5.17 and a selected few are listed as flows:

- polygonal shape of the rim and pronounced W-E wall asymmetry with topographically lower, narrower and steeper terraced walls on the eastern side
- presence of a distinct eye structure in the northwestern edge due to enhanced slumping
- low albedo proximal ejecta mainly confined to the northern areas
- rhombic sections on the walls due to cross-cutting of terraces and lineaments
- prominent ‘V’ shaped slump zone on the central peak alongside a deep and steep ‘V’ shaped depression on the crater floor
- retention of most of the impact melts on the crater floor with very few external melt pools that are concentrated in the northeastern areas only
- W-E asymmetry in the distribution of floor irregularities with most of them present on the eastern side
- presence of deep and steep rayed Crater S, a superposed crater on the eastern wall
- A distinct recent resurfaced unit on the eastern side, which could be due to recent volcanic activity (?) subsequent to the emplacement of impact melts from Crater S

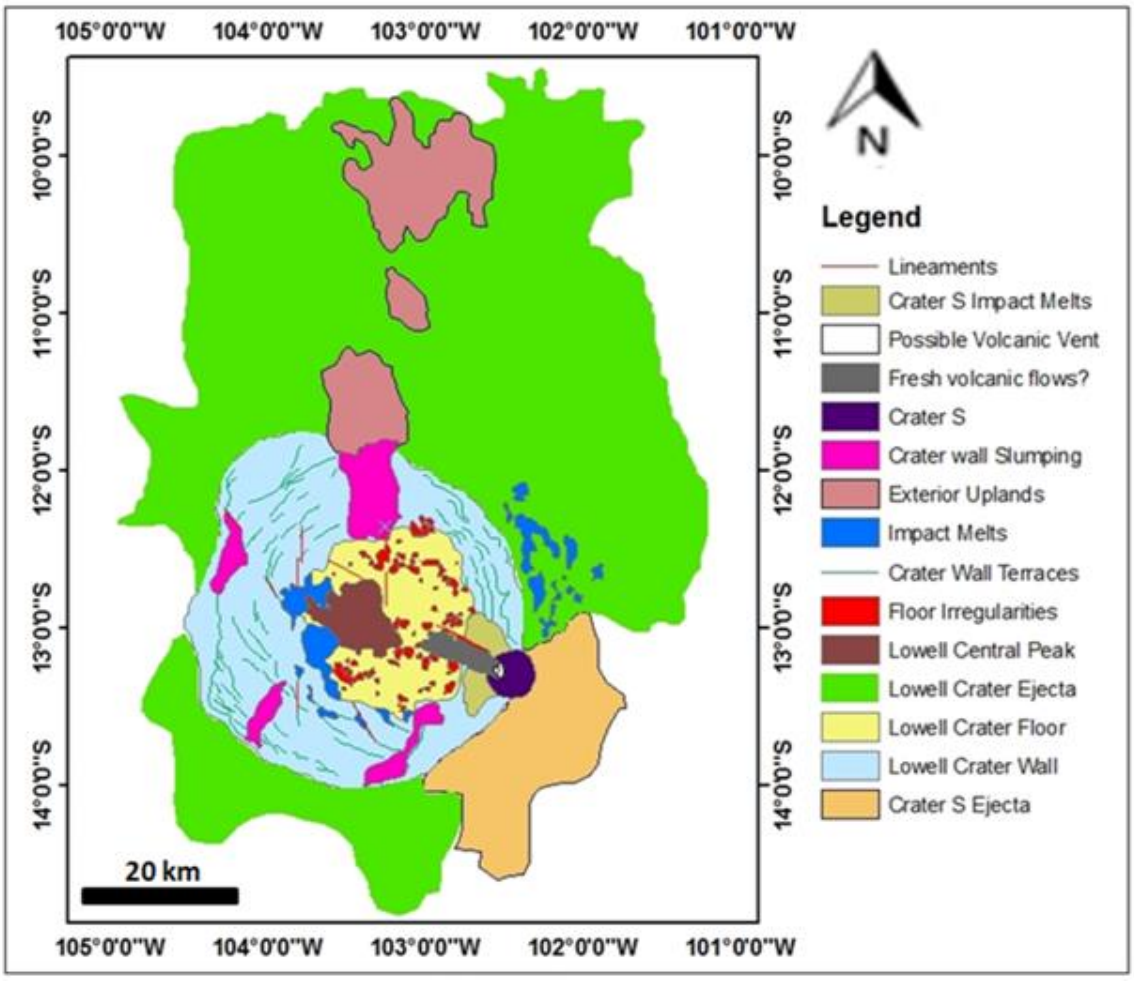

Figure 5.17 Geomorphological map of the Lowell crater prepared using photometrically corrected 750 nm M^3 data shown in Fig. 6.4, which clearly shows the extent of the low albedo ejecta around the crater.

Most of these observed specialties in case of the Lowell crater appear to be related to its broad geologic context i.e. location inside Orientale basin, the pre-existing surface topography and/or structure of the target region, and also to the angle and direction of the impact. Thus, the Lowell crater region emerges as an appropriate candidate for further investigating the effect of these important parameters on the impact cratering process.

Chapter 6

Spectral analysis for composition

6.1 Reflectance spectroscopy

The composition of rocks and their distribution on planetary surfaces provide important clues to the evolutionary processes that the planetary bodies have undergone since their formation. For distant and inaccessible planets, remote sensing, either from earth-based telescopes or from a fly-by/orbiter around the planetary body, has efficiently helped in identification and mapping of surface composition (e.g. Pieters, 1986; Pieters and Englert, 1993; Reddy et al., 2012a, b). The technique mainly used for this purpose is reflectance spectroscopy, which involves measurement of solar reflection from a target in the UVVISNIR region of the electromagnetic spectrum in discrete spectral bands (Adams, 1974; Adams et al., 1981; Hapke and Wells, 1981; Pieters, 1986; Burns, 1993; Pieters and

Englert, 1993; Clark, 1999; Gaffey et al., 2002; Gupta, 2003). The reflectance value when plotted against wavelength produces a spectral reflectance curve, which exhibits characteristic features that are used to identify the specific minerals present, thereby, enabling identification of the lithology of the area.

The orbit based reflectance spectroscopy is carried out in multi-spectral mode as well as in the hyperspectral mode. Multi-spectral technology involves measurement of reflectance value in a small number of discrete spectral bands such as in the case of Clementine mission (1994), when UVVIS multispectral data of the global Moon was acquired in five discrete spectral bands centered at 415 nm, 750 nm, 900 nm, 950 nm and 1000 nm (Nozette et al., 1994). With advances in technology and realization of the scientific importance, a hyperspectral sensor onboard an orbiter has developed into a popular and powerful tool for compositional mapping of planetary surfaces (Pieters and Englert, 1993; Gupta, 2003). It involves measurement of reflectance of a target in numerous, narrow contiguous spectral bands.

An advanced form of hyperspectral remote sensing is imaging spectroscopy which involves acquisition of inherently registered images of a scene in numerous fine and contiguous spectral bands (e.g. Pieters and Englert, 1993; Gupta, 2003). The concept of imaging spectroscopy is depicted in Fig. 6.1. Each pixel of a spectral image records reflectance value for a small ground segment which is termed as instantaneous field of view (IFOV) or the spatial resolution. The reflectance values when integrated over the entire wavelength provide spectral reflectance curve for a particular ground element, which is used to identify the composition.

The first imaging spectrometer flown on a planetary mission was the Infra-red Spectrometer (ISM) aboard Soviet Phobos mission to Mars in 1988. Several recently concluded/ongoing and planned planetary missions such as Chandrayaan-1 (2008) and Chandrayaan-2 for the Moon, Mars Reconnaissance Orbiter (2005) for the ‘Red Planet’, Cassini (1997) for Saturn, NEAR (1997) for asteroid and Rosetta (2004) for comet have an imaging spectrometer onboard.

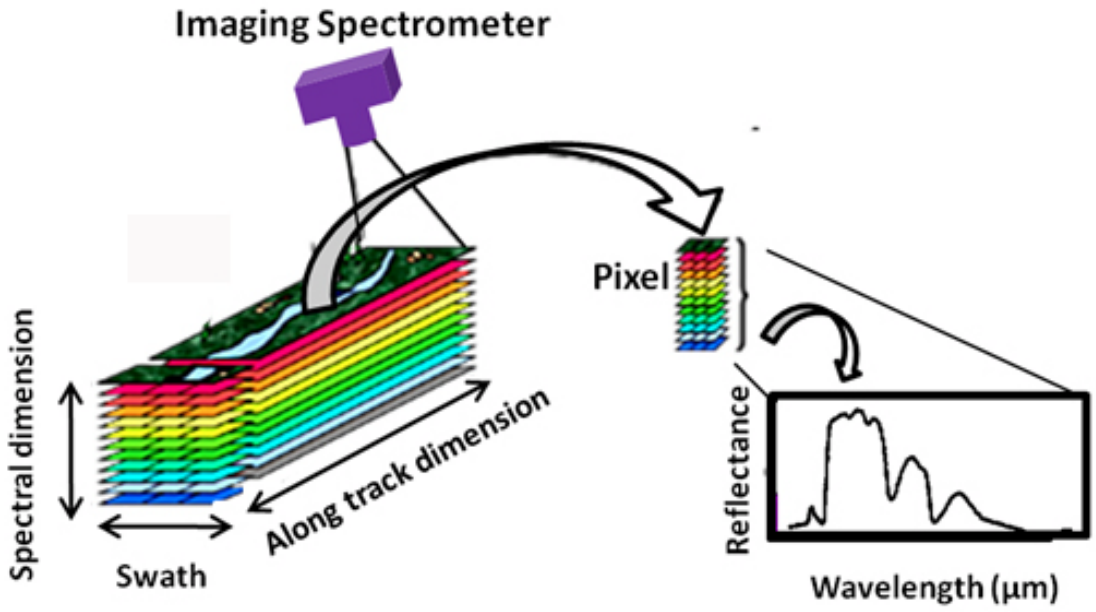

Figure 6.1 A schematic depicting concept of imaging spectroscopy. An area is imaged into several pixels, each encoded with a spectrum composed of several narrow contiguous bands, which is used to identify the material. The along track dimension is built by the motion of the spacecraft. The radiance measured by the spacecraft is converted to reflectance for material identification. [Source of base image: geospatialworld.net].

A wealth of hyperspectral data is available from the Moon in the UVVISNIR region of the electromagnetic spectrum, from imaging spectrometers M^3, HySI and point spectrometer SIR-2 onboard Chandrayaan-1 mission (Goswami and Annadurai, 2009; Pieters et al., 2009a; Boardman et al., 2011). These data are suitable to decipher principal lunar rock types on the basis of characteristic spectral reflectance signatures of their dominant minerals due to electronic transitions in ferrous ion present in their crystal lattice**.**

6.2 Factors affecting reflectance spectra

Reflectance spectra generated from remote sensing represent the sum total of contributions from various mineral assemblages present in the target. Further, the absolute values of reflectance of each mineral depend on a number of physical and chemical parameters such as composition, grain size, temperature, and surface maturity. The

scanning procedure employed and variations in sun angle during data acquisition further complicate it.

6.2.1 Composition

The laboratory derived characteristic spectral reflectance curves produced by common minerals which are found on the lunar surface are shown in Fig. 6.2. Pyroxene, olivine and anorthite are the major lunar minerals; whereas, recently discovered Mg-spinel and Cr-spinel (devoid of mafics and associated with anorthite) (Pieters et al., 2011) are new additions to this inventory and are being continuously reported from various parts of the Moon (Sunshine et al., 2010; Dhingra et al., 2011; Dhingra and Pieters, 2011; Lal et al., 2012; Bhattacharya et al., 2012; Kaur et al., 2012; Srivastava and Gupta 2012, 2013; Sun et al., 2013; Srivastava et al., 2013). Previously, in the Apollo samples Mg-spinels were only known to occur in association with mafic component such as olivine.

As illustrated in the figure (Fig 6.2), these minerals produce prominent characteristic absorption features in the VNIR spectral range 0.4 – 3.0 μm. The number of bands, their shape and position vary for different minerals. The pyroxenes, one of the ubiquitous minerals in our solar system, exhibits simple nearly 'V' shaped absorptions at ~1 μm and ~2 μm. In contrast, olivine shows a single broad tri-component absorption feature ~1 μm and the spinel shows a lone broad absorption feature centered ~2 μm (Pieters et al., 2011). These characteristic absorptions in the spectra are due to crystal field transitions in Fe^{2+} ions located in the specific distorted crystallographic sites (e.g. Adams, 1974; Burns, 1993; Clark, 1999; Varatharajan et al., 2014).

In pyroxenes, presence of Fe^{2+} ions in the crystallographic sites M1 and M2 (larger and more distorted) results in the diagnostic absorption bands ~1 μm and ~2 μm. The Fe^{2+} in the M2 site contributes to the 1 μm and 2 μm absorptions, whereas, Fe^{2+} ions in the M1 site only contribute to the 1 μm feature. This makes the 1 μm absorption relatively intense in energy compared to the 2 μm absorption due to superposition (Burns, 1993; Pieters and Englert, 1993). The low-Ca variety i.e. orthopyroxenes show absorption features centred at wavelengths between 0.9-0.95 μm and ~2.0 μm, which is normally shorter compared to the high-Ca variety i.e. the clinopyroxenes, which show band centers between 0.95-1 μm and

~2.25 µm (e.g. Staid et al., 2011; Pieters et al., 2011; Kaur et al., 2013; Varatharajan et al., 2014). As shown by Klima et al. (2011), the multiphase pyroxenes shows a continuous trend in the band center 1 Vs band center 2 values with respect to the increase in Fe^{2+} content (for low Ca^{2+}-pyroxenes) and then Ca^{2+} content.

The Fe rich orthopyroxenes and clinopyroxenes also exhibit a mild absorption feature ~1.2 µm due to presence of Fe^{+2} in the M1 crystallographic site**.** Normally its strength (which is directly related to Fe^{+2} content in the M1 site) is less than the 2 µm absorption feature; however, in Ca saturated pyroxenes the strength can exceed the 2 µm absorption strength. Its intensity is related to the thermal history of the pyroxenes (Klima et al., 2007; Klima et al., 2011)**.** In case of pyroxenes that are formed at high temperatures but which are quickly cooled, the ordering is less, resulting in more Fe^{+2} at the M1 site, and therefore a stronger 1.2 µm band.

The tri-component olivine signature ~1 µm has a middle absorption feature centered ~1.05 µm due to presence of Fe^{+2} ion at the M2 crystallographic site and the two exterior absorptions centered ~0.85 µm and ~1.25 µm due to the presence of Fe^{2+} ion at the M1 crystallographic site. With increase in the Fe content the tri-component band in olivine gets stronger and it shifts towards higher wavelengths. Thus, high spectral resolution reflectance data can be used to determine the forsteritic or fayalitic nature of olivine samples (Sunshine and Pieters, 1998).

The un-shocked plagioclase shows a broad and minor ~0.5% mafic absorption at ~1.25 µm due to presence of traces of Fe^{+2} as impurity (Bell and Mao, 1973; Adams and Goullaud, 1978). However, this feature could be lost due to the shock pressures, transforming it to a featureless spectrum (Adams et al., 1979; Bruckenthal and Pieters, 1984). Therefore, shocked anorthosites do not show any absorption feature and exhibits monotonically increasing reflectance spectra. Thus, definitive identification of anorthosite is hampered by presence of other mineral components (~1.25 µm band of olivine and clinopyroxenes) and space weathering process (discussed in section 6.2.4). Hereafter, until specifically described as “un-shocked”, the term anorthosite refers to the shocked anorthosite only.

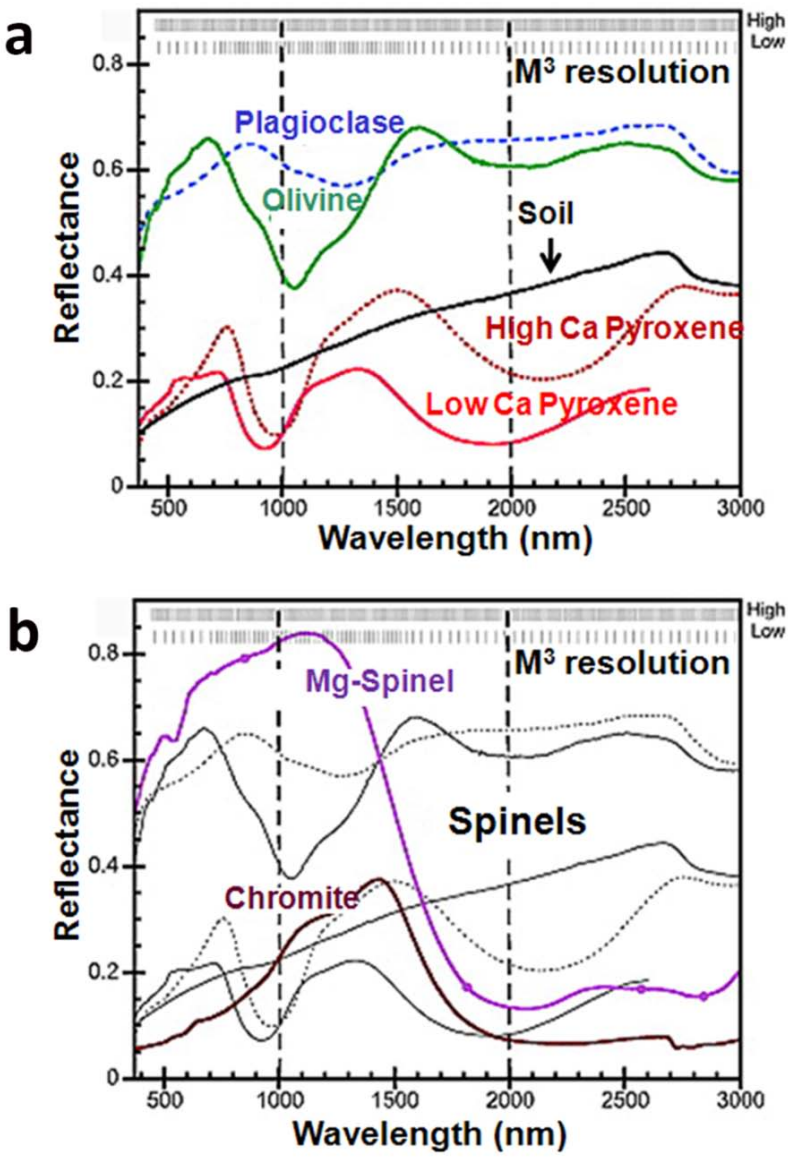

Figure 6.2 a) Laboratory reflectance spectra of major lunar minerals and soil. The pyroxenes show simple 'V' shaped absorptions ~1 µm and ~2 µm, olivine shows composite spectra centered ~1.1 µm, and plagioclase (unshocked anorthite) exhibits a weak and broad absorption feature centered ~1.25 µm. The soil shows monotonically increasing featureless spectra due to optical effects of space weathering; b) Laboratory spectra of terrestrial spinels (Mg-spinel and Chromite) are superposed over spectra of lunar silicates and soil [Source: Pieters et al. (2011)].

The presence of water ice and hydrated minerals can also be predicted on the basis of specific vibrational bands in the VNIR region of the electromagnetic spectrum. Water ice has bands centered ~0.81, 0.9, 1.04, 1.25, 1.5, 1.65, 2.0 and 3 microns (Pieters and Englert, 1993; Gupta, 2003). However, some of them may be easier to detect than others since their detection depends upon number of factors such as temperature, grain size, presence of other mineral components etc. Compared to the broader electronic transition bands for silicates the vibrational absorption features are sharp and narrow. Therefore, they essentially require very high spectral resolution for their detection and analyses. Recently M^3 data ~3 µm has revealed vibrational signatures of OH/H_2O on the Moon's surface (Pieters et al., 2009b).

Usually, reflectance spectrum from a planetary surface is a composite signal from different mineral components present within the IFOV of the sensor. For effective analysis and interpretation, it is essential to understand the effect of mineral mixtures on reflectance spectra. For example, presence of minor quantities of opaque, such as ilmenite ($FeTiO_3$), drastically reduces the reflectance values of the silicates and the spectra are flattened due to loss of contrast (Pieters and Englert, 1993). In case of mixtures of orthopyroxenes and clinopyroxenes, the band centre of the composite spectra shifts towards higher wavelength with increase in the clinopyroxene content. Thus, gabbros/basalts possess absorption bands centred between 0.95-1 µm and ~2.25 µm due to dominance of high-Ca pyroxenes whereas norites show absorption features centred at shorter wavelengths i.e., between 0.9-0.95 µm and ~2.0 µm, due to the dominance of low-Ca pyroxenes.

6.2.2 Grain size

It is one of the prominent factors affecting reflectance value of a particular target (Fig. 6.3a). Decrease in grain size increases the interaction area, therefore, minerals which are less absorbing or largely transparent, such as pyroxene, show increased reflectance with decrease in grain size, whereas, strongly absorbing minerals such as ilmenite ($FeTiO_3$) show decrease in reflectance with decrease in particle size. However, the position of the absorption band does not change with changes in the grain size (Pieters and Englert, 1993; Clark, 1999).

6.2.3 Temperature

Variations in temperature result in increased or decreased molecular vibrations and changes in crystal structure. Specific effects of temperature on reflectance properties vary from one mineral to the other. In general, it causes shift in positions and changes in intensities of crystal field absorptions (Singer and Roush, 1985). Further, temperature of a surface determines the wavelength at which thermal emissions become pre-dominant (compared to the reflected energy), therefore, can interfere with the reflectance values. The M^3 data beyond 2 μm was severely contaminated by thermal emissions from the Moon, therefore, appropriate corrections were made to make it fit for reflectance spectroscopy (Clark et al., 2011).

6.2.4 Surface maturation

Surface maturation is a phenomenon experienced by atmosphere-less planetary bodies having negligible magnetic field, such as the Moon, Mercury and asteroids (e.g. Hapke, 2001; Sasaki et al., 2003). Due to the absence of these barriers, weathering agents such as solar wind, galactic cosmic rays (GCR), meteorites and micrometeorites continuously bombard their surface causing melting of grains, chemical reduction, formation of agglutinates, and continuous reworking or "gardening" of the surface. Through time, these processes change the composition and texture of the original rocky components of the surface and greatly modify the optical properties of the area. Broadly, surface maturation reduces the absolute reflectance value of a target and also causes reduction in spectral contrast i.e. reduction in the band depth of the characteristics absorption features (Fig. 6.3c). It also causes steepening of the spectra or increase in the reflectance values towards NIR range of the electromagnetic spectrum.

6.2.5 Viewing geometry

During the data acquisition from a reflectance sensor aboard a spacecraft, the phase angle i.e. the angle between the source, target and sensor continuously changes due to change in solar zenith and elevation with time and also due to the changes in the attitude of the space craft in certain cases. This result in change in the shape of the reflectance spectra

(Mustard and Pieters, 1989) as shown in laboratory spectra of olivine acquired under different viewing geometries (Fig. 6.3d).

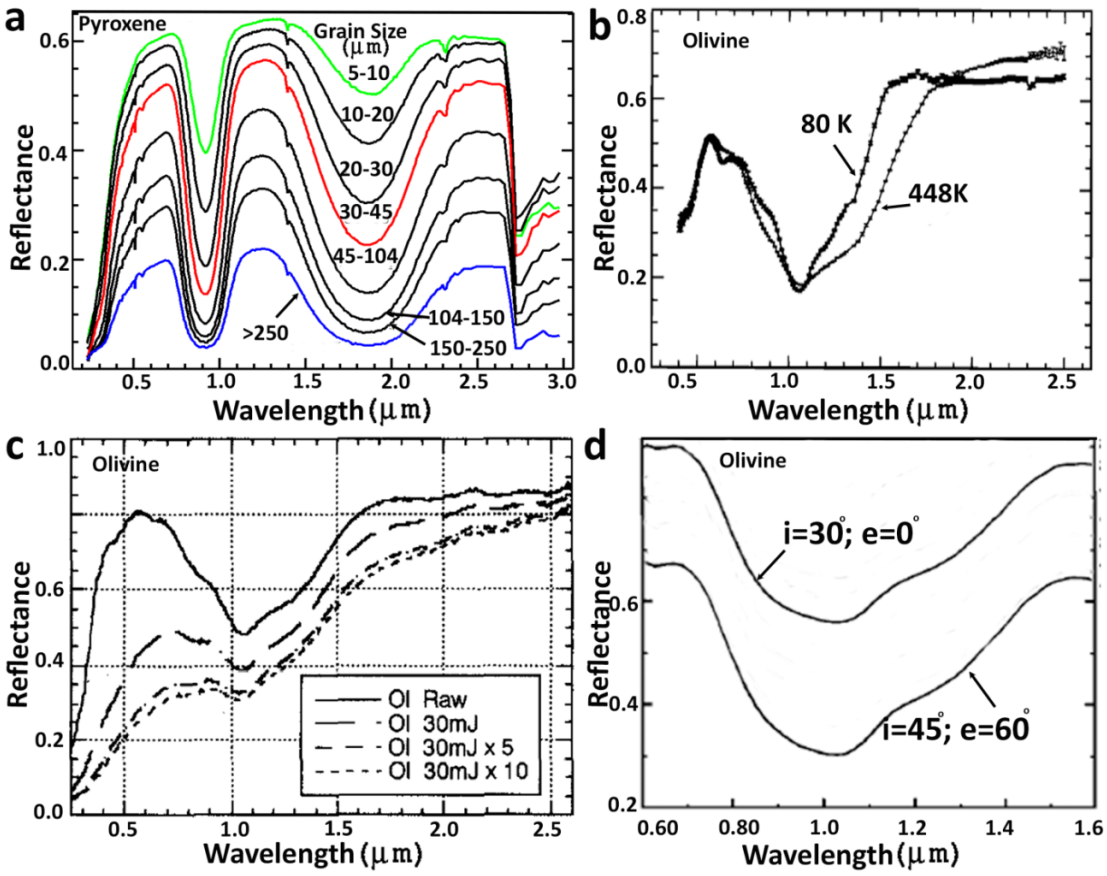

Figure 6.3 Effect of physical parameters on the reflectance spectra of minerals; a) grain size decrease results in increased reflectance and the spectral contrasts also changes; b) increase in temperature leads to broadening of the absorption band of olivine; c) the characteristic shape of the olivine spectra is lost with increased LASER irradiation simulating space weathering; d) the spectral shape for olivine changes as a function of phase angle. Here, spectra has an offset for clarity [Sources: modified after a) Clark, 1999; b) Singer and Roush, 1985; c) Sasaki et al., 2003; d) Mustard and Pieters, 1989].

6.3 Dataset used for spectral analysis

Calibrated global mode Level 2 hyperspectral data from M^3 have been used to investigate spectral characteristics of the study area. They comprise of 83 near-contiguous bands spanning 540 – 2980 nm. The spatial resolution is 140 meters and the spectral resolution varies between 20 – 40 nm (Table 4.1)**.** The data has been downloaded from PDS Geosciences Node Lunar Orbiter Data Explorer. The Level 2 data product is reflectance data derived from the Level 1B radiance data with data calibration steps including I/F correction, statistical polishing, thermal correction, photometric correction and band masking for reducing the noise and the artifacts in the data (Boardman et al., 2011; Green et al., 2011; Clark et al., 2011).

Vertical stripping in the M^3 images is due to the change in gain, offset and performance of the detector array elements and also the temperature of the detector operating above the nominal temperature causing degradation in signal-to-noise ratio (Green et al., 2011). The vertical bright lines in the data are due to calibration artifacts in the data (Besse et al., 2013). Images from optical period OP1B have only been used for preparing mosaic of the main study area i.e. the Lowell crater region. However, for peripheral studies involving entire Orientale basin, few strips from optical period OP2A has also been included. In total, 28 M^3 strips (Table 4.2) have been used to generate a mosaic of the Orientale basin by geo-referencing individual data strips using LOC file provided with the data and mosaicking them using ENVI.

6.4 Spectral parameters and analytical tools used

The derivation of useful compositional information from hyperspectral data requires selection/derivation of proper spectral parameters and application of appropriate analytical tools. Due to the high degree of dimensionality in imaging spectroscopy data, specialized techniques (such as Principal Component Analysis (PCA), Minimum Noise Function (MNF) and Spectral Angle Mapper (SAM)) are used for reducing data redundancy and classification (Boardman and Kruse, 1994; Green et al., 1988; Gupta, 2003; Gupta et al., 2013). However, as mentioned in section 6.2.4, spectral characteristics of airless Moon is a function of surface maturation also apart from composition; therefore, it is extremely

difficult to adopt a specific approach or technique to accurately classify and prepare a lithological map of an area. Any generalized and classified output for the Moon should be interpreted in conjunction with back and forth checking of the nature of the representative spectra vis-a-vis their geologic setting. In this study, to derive best possible representation for lithological variability, a detailed manual spectral survey has been carried out using ENVI software and color composites prepared using popularly used schemes and Minimum Noise Function (MNF) based approach. Specific parameters and related techniques used in this study are detailed in the sub-sections 6.4.1 – 6.4.5.

6.4.1 Continuum removal

Effective removal of the sloping continuum in the spectra is essential for accurate estimation of spectral parameters (Isaacson and Pieters, 2010; Varatharajan et al., 2014). Here, we have adopted the methodology of continuum removal as described by Clark et al. (1987). The local maxima with respect to a common baseline in the normalized reflectance spectra are first identified and then a straight line convex hull is fitted over, by connecting the two local spectral maxima on either side of the diagnostic absorption ends. In this study, following the methodology proposed by Cheek et al. (2011), 1 μm absorption feature is isolated by anchoring the continuum end points at 699 nm and 1578 nm and the 2 μm feature has been studied by anchoring the continuum at 1578 nm and 2538 nm (equations 2 – 3 in section 6.4.3).

6.4.2 Band center

As stated earlier in section 6.2.1, band centre is an important spectral parameter for interpreting compositional variations. For accurate estimation of the band center of the absorption features in the spectra, the sloping continuum has been removed as discussed in section 6.4.1. After removing the continuum, the band center has been estimated by fitting 2^{nd} order-3^{rd} degree polynomial to the range of reflectance values of the continuum removed absorption ends of the spectra as explained in Moriarty et al., 2013. The minima of these fitted curves correspond to the band center of the respective absorption features. To reduce ambiguity in estimation of band centre, the set of the reflectance values selected

for fitting the curve has been carefully chosen by thoroughly examining the nature of the absorption ends.

6.4.3 Integrated band depth

Defined by Cheek et al. (2011), integrated band depth (IBD) is widely used for studying compositional variations in an area using M^3 data. The band depth represents strength of the spectral absorption feature at a particular wavelength and is dependent on absorption strength of the mineral itself, their grain sizes and the abundance of the mineral, either as mono-mineral or as mixtures (e.g. Adams, 1974; Cloutis and Gaffey, 1991; Klima et al., 2007, 2011; Denevi et al., 2007). Instead of the commonly used band strength estimated only at the band minima, this IBD based method integrates band strength values across the complete wavelength range of the one and two micron absorption feature.

The apparent depth of an absorption feature D, relative to the continuum in a reflectance spectrum is given by (Clark and Roush, 1984):

Band Depth = 1 – Continuum removed Spectra (1)

The IBD refers to integration of the band depths over the spectral subset of an absorption feature and is proportional to the band area of the absorption feature. According to Cheek et al. (2011), IBD 1000 and IBD 2000 in case of M^3 data are given by:

$$\text{IBD } 1000 = \sum_{N=0}^{26} R(789 + 20n) / R_c(789 + 20n) \quad (2)$$

$$\text{IBD } 2000 = \sum_{N=0}^{21} R(1658 + 40n) / R_c(1658 + 40n) \quad (3)$$

Where, R – reflectance, R_c – continuum removed reflectance

As earlier mentioned in section 6.4.1, for IBD 1000 estimation the continuum offsets are chosen at 699 nm and 1578 nm and for IBD 2000 estimation the continuum offsets are chosen at 1578 nm and 2538 nm. After deduction of the two IBDs, compositional analysis is carried out with the aid of a popularly used FCC (False Color Composite) scheme. IBD 1000 and IBD 2000 are assigned red and green colors

respectively, and R1478 is represented by blue color. In such a scheme, yellow, green and orange tones refer to variations in maturity and composition of mafic rocks and blue/purple refer to feldspathic terrains and/or areas with high degree of space weathering.

6.4.4 Band ratios

Band ratios are useful parameters for characterizing variations in spectral reflectance curves. For e.g. since derivation of continuum is not possible in case of multi-spectral Clementine UVVIS data, therefore R950/R750 or R1000/R750 nm is popularly used as a proxy for the 1 μm band depth (e.g. Lucey et al., 1998). Further, usage of band ratios is popular in spectral reflectance studies since variations in spectra due to several known and also unknown physical parameters such as differences in lighting conditions between two regions gets normalized.

In this study, specific band ratios R_{1209}/R_{1818} (Band 30/Band 54), R_{730}/R_{930} (Band 6/Band 16) and R_{1000}/R_{1250} (Band 30/Band 32) have been used to prepare a FCC of the study region by assigning them red, green and blue colors respectively. Proposed by Dhingra et al. (2011), such a composite is useful in highlighting Mg-spinel anorthosite dominant regions in a scene. They occur in shades of magenta and soft pink. The pyroxene and /or olivine dominated areas appear in the shades of green and plagioclase dominated exposures are represented by blue color.

6.4.5 MNF transformation

Hyperspectral data by nature has abundant redundancy. MNF rotation transform is used to establish intrinsic dimensionality of hyperspectral image data to segregate noise and to facilitate subsequent processing by reduction of the computational requirements (Boardman and Kruse, 1994; exelisvis.com). The MNF transform is a linear transformation that consists of two separate principal component analysis rotations (Green et al., 1988).

The first rotation uses the principal components of the noise covariance matrix to de-correlate and rescale noise in the data such that the resultant noise has unit variance and is devoid of band-to-band correlations. This process is known as noise whitening. The second rotation uses the principal components derived from the original image data after

they have been noise-whitened by the first rotation and rescaled by the noise standard deviation. The intrinsic dimensionality of the data is determined by examining the final eigen values and the derived images. The data space is divided into a part that is associated with large eigen values and coherent eigen images, and a complementary part with near-unity eigen values and noise-dominated images. Improved spectral processing results are obtained by using only coherent portions thereby separating noise from the data.

In this study, MNF transformation has been applied to the M^3 data. Only bands with high eigen values and non-noisy appearance in the display have been selected and FCCs have been produced using their various permutations and combinations. Based on the consistency in knowledge derived from manual deductions of spectral variations and application of popularly used techniques (described in sections 6.4.3 and 6.4.4), the most appropriate FCC deciphering compositional variations in the region has been selected as a proxy for lithological map of the study region.

6.5 Mineralogy of Lowell crater region

6.5.1 General details

Spectral diversity in the Lowell crater region has been deciphered based on spectral reflectance curves derived from the M^3 hyperspectral data. Using ENVI software, a pixel-by-pixel examination of the spectra has been carried out to evaluate effectiveness of popularly used colour coding schemes in this case (sections 6.4.3 and 6.4.4) in mapping the spectral diversity of the area and to aid in interpreting MNF based FCC (section 6.5.3).

Four pixel average spectra have been derived for specific locations and band centers have been estimated as discussed in section 6.4.2 (Table 6.1). Since the Lowell crater is only Copernican in age (discussed in Chapter 7), its geologic units are not mature; however, the surrounding areas are quite old and are therefore spectrally mature. In order to minimize the effect of surface maturation for these old units, except for the mature soils, spectra have been derived from fresh craters/slopes where soil formation and/or accumulation would be least.

Broadly, eight distinct spectral signatures have been identified in the area. Representative sites (S1-S8) for each of these are marked in Fig. 6.4 and corresponding spectra are plotted in Fig. 6.5. These indicate presence of the gabbroic/basaltic rocks, noritic rocks, anorthositic rocks (un-shocked, shocked and Mg-spinel bearing), mature soils pyroclasts, and troctolites with Mg-spinel / olivine rich gabbro/basalt / co-existence of crystalline anorthosite and gabbro/basalt / mafic lithology bearing iron rich pyroxenes with Fe^{+2} at M1 site. The pyroclasts typically show noisy spectra with a peak ~750 nm, a strong 1 µm band and a weak 2 µm feature. Occasionally, they have been found to be associated with strong OH/H_2O band ~2.8 µm. Caution is needed to infer them since the shadowed areas also show similar characteristics.

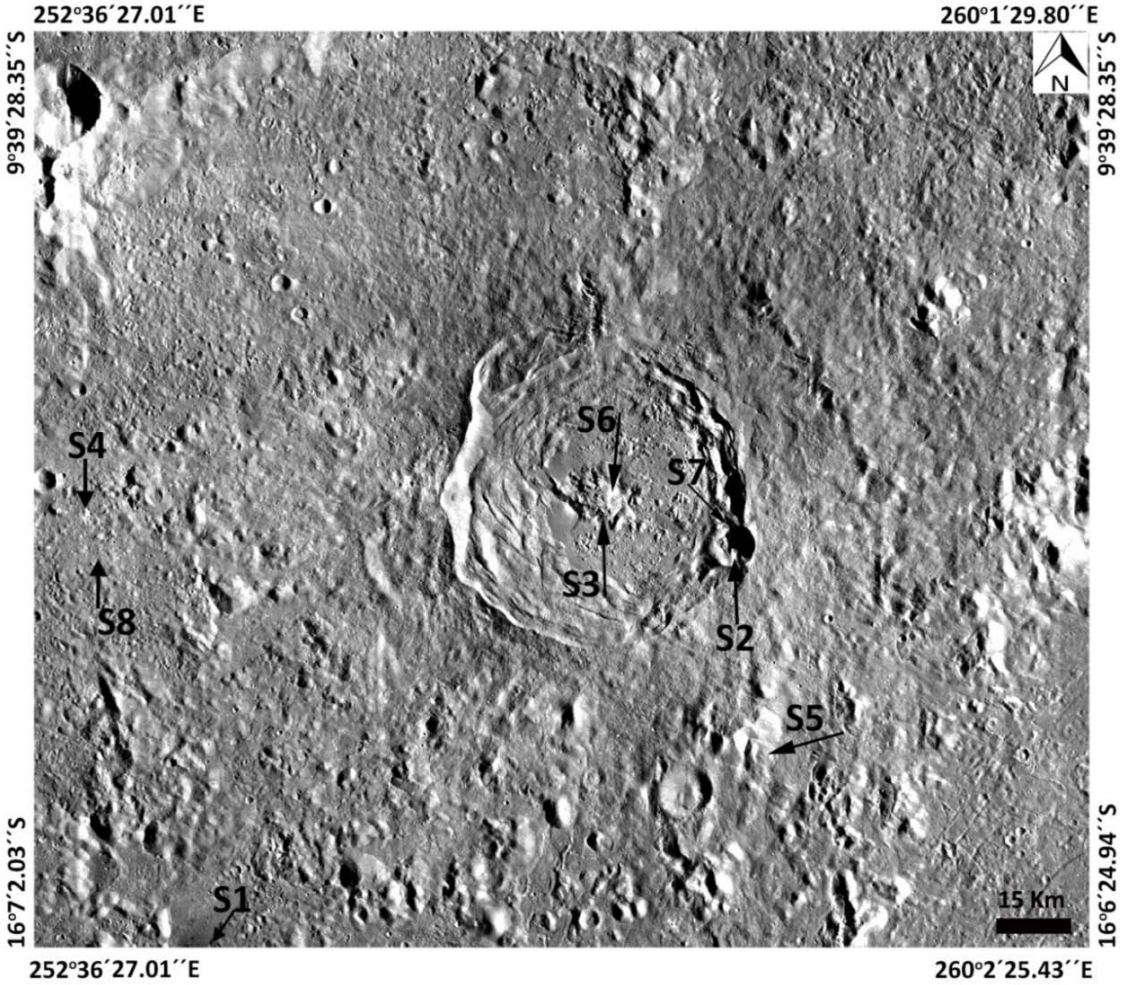

Figure 6.4 M^3 750 nm image mosaic of the Lowell crater region showing selected representative locations for which average (4 pixel) reflectance spectra and corresponding continuum removed ones have been plotted in Fig. 6.5 to reveal spectral diversity in the

area. Here, S1: Lacus Veris pond, S2: Crater S wall, S3: boulder lining on the central peak, S4: fresh surface inside a crater sampling Rook formation, S5: Inner rook massif, S6: central peak slump zone; S7: pyroclasts, S8: mature soil.

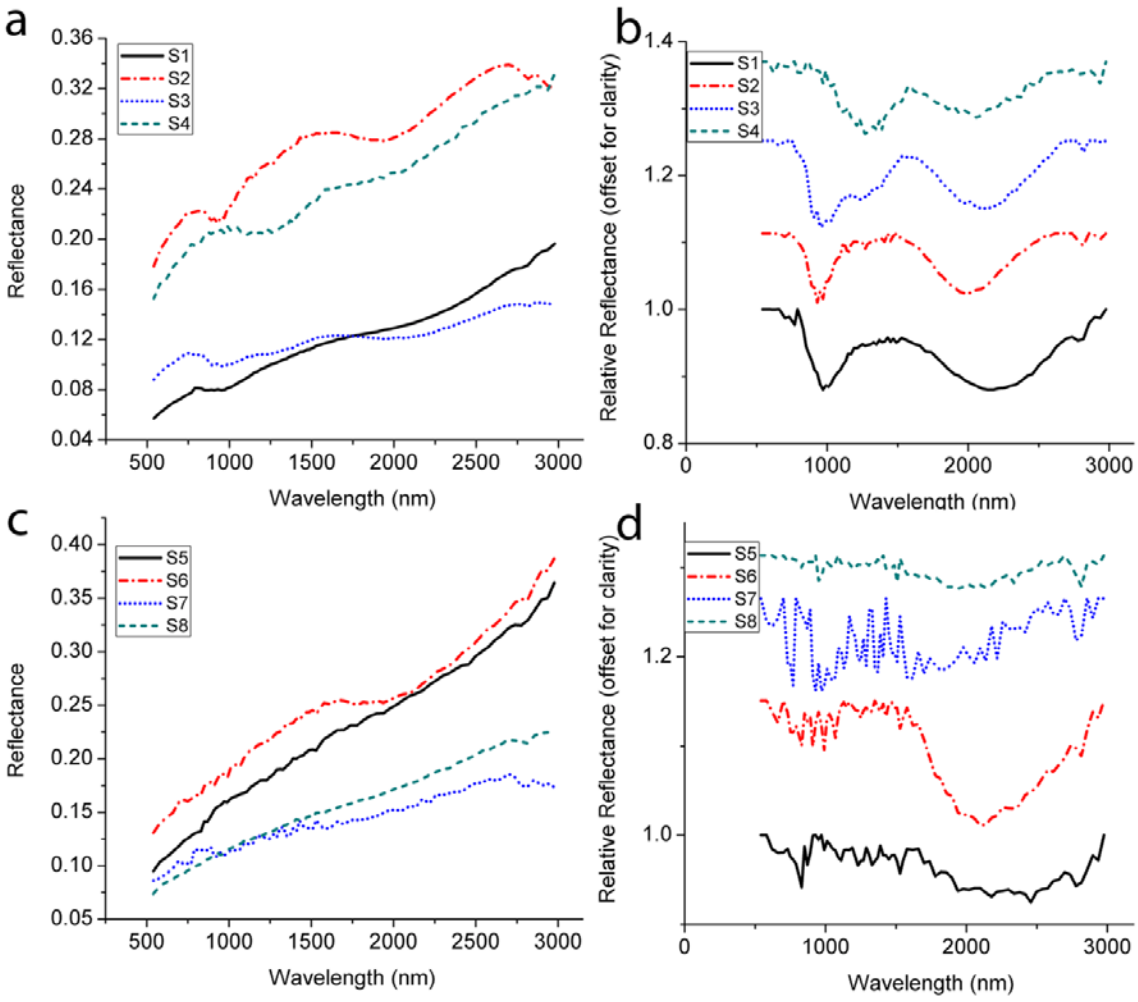

Figure 6.5 a, b) Average (4 pixel) reflectance spectra for sites S1-S4 marked in Fig. 6.4 and their corresponding continuum removed ones. The dominant mineralogy for these sites are S1: cpx, S2: opx, S3: [olivine along with Mg-spinel/cpx/opx] / [crystalline feldspar + cpx/opx] / [Fe rich pyroxene with Fe^{+2} at the M1 site], and S4: un-shocked anorthosite; c, d) Average spectra and corresponding continuum removed ones for for sites S5-S8 marked in Fig. 6.4 and; Here, S5: shocked anorthite, S6: Mg-spinel, S7: pyroclasts and, S8: mature soils.

False color composites (FCCs) have been made to get information about spectral variability in the study area. They have been prepared according to methodologies discussed in sections 6.4.3 and 6.4.4 and are shown in Figures 6.6 and 6.7 respectively. The largely blue appearance of the Lowell crater region in IBD based FCC (Fig. 6.6) suggests that the study area is largely anorthositic in composition or is highly space weathered; however, the Lowell crater has exposed mafic rocks as suggested by largely greenish to cyanish tinge in various units of the Lowell crater including the ejecta. The Lowell crater ejecta emplacement and distribution, which was not clearly seen in the grey-scale M^3 bands, is now clearly evident in the color composite.

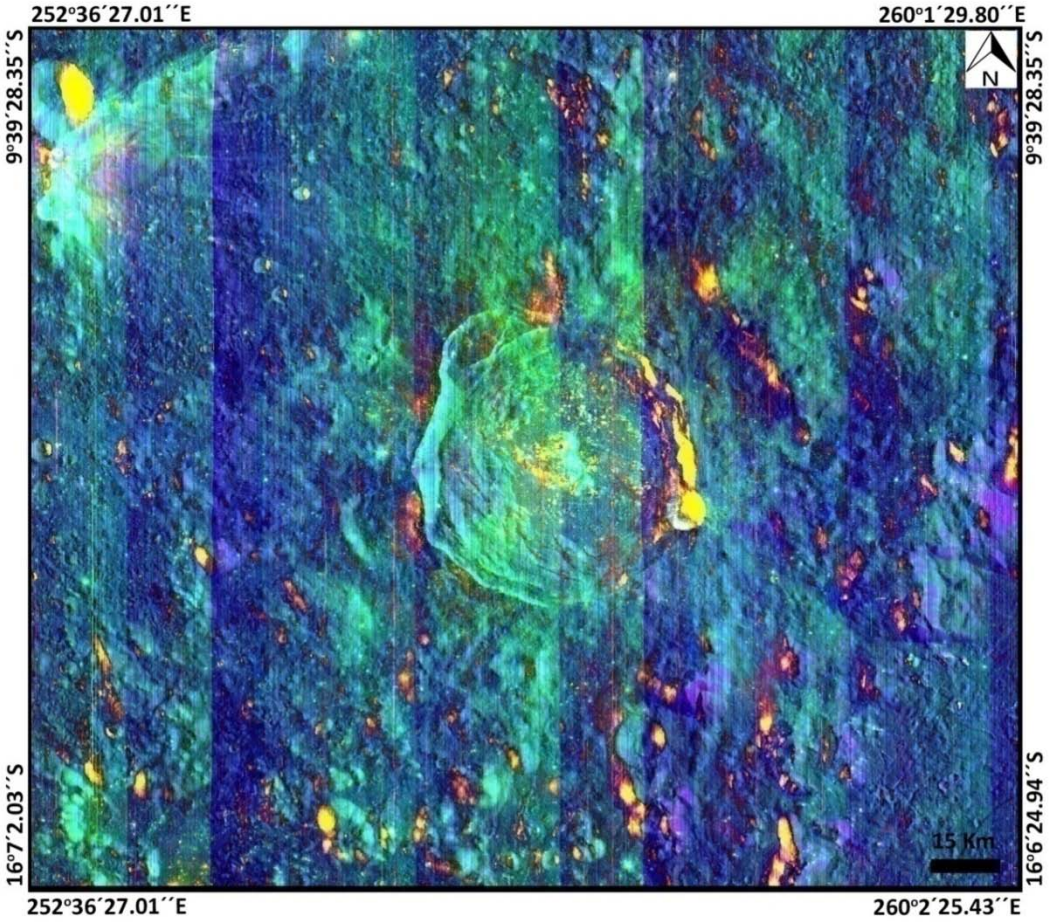

Figure 6.6 M^3 derived FCC of the Lowell crater region prepared according to IBD based scheme proposed by Cheek et al., 2011 [Red: IBD 1000, Green: IBD 2000, and Blue: R_{1547}. Here, yellow/green/orange tones: mafic regions with different degrees of maturity and blue/purple: feldspathic terrains and/or areas with high degree of space weathering. Note: The shadowed regions have also appeared as red/orange/yellow.

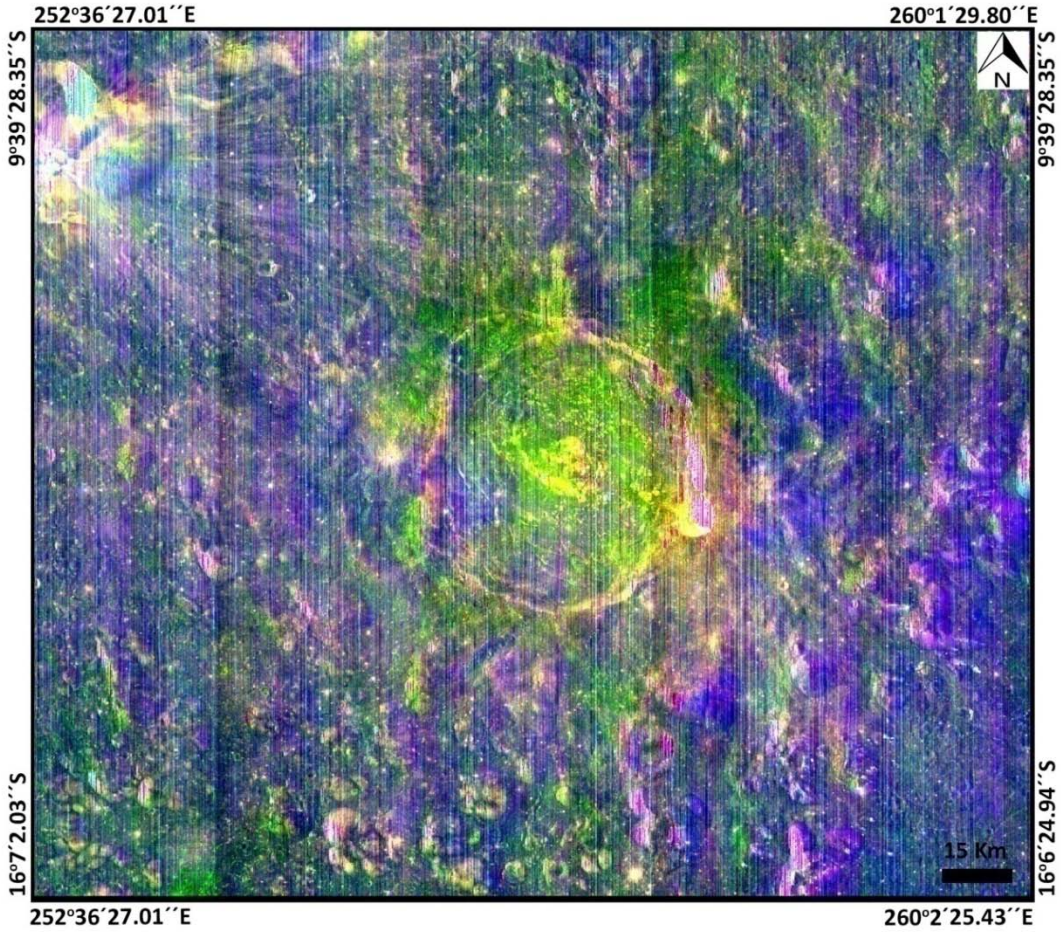

Figure 6.7 M^3 derived FCC of the Lowell crater region prepared according to band ratio based scheme proposed by Dhingra et al., 2011 [Red: R_{1209}/R_{1818} (Band 30/Band 54), Green: R_{730}/R_{930} (Band 6/Band 16) and Blue: R_{1000}/R_{1250} (Band 30/Band 32)]. Here, greenish/yellowish regions: pyroxene dominated, bluish areas: anorthositic, and magenta/soft pink : Mg-spinel anorthosite.

Mg-spinel ejecta is indicated by its largely greenish tinge, reflecting stronger 2 µm absorption feature compared to the 1 µm absorption band. Further, cyanish appearance of certain areas such as the eastern portions of the central peak and few locations on the western rim etc., indicate possibility of presence of exposures of Mg-spinel anorthosites. The yellow and red hued areas in the FCC, such as, most of the floor irregularities should in principle be pyroxene dominated areas, however, the interpretation is largely limited due to deep shadows in the scene, which also occur in shades of yellow and red.

The band ratio based FCC (Fig. 6.7) show spectral variations consistent with IBD based color composite. A large number of units inside Lowell crater and in the adjoining areas also show soft pink to magenta hue suggesting possibility of extensive exposures of spinel anorthosites in the region (Srivastava and Gupta 2012, 2013). Most of the massifs on the eastern side show dark blue color indicating presence of un-shocked plagioclase in them. In this classification, the deeply shadowed regions are easily demarcated due to their anomalously textured (dotted) appearance.

An alternate MNF based scheme has been worked out here because both the popularly used FCCs (i.e. the IBD based and band ratio based) do not efficiently capture spectral variations in the area. Though mafic nature of the ejecta is easily discernible in both the schemes, distinction between orthopyroxene and clinopyroxene dominated areas is not possible. Further, both these schemes do not provide distinct information about exposures of un-shocked anorthosites.

Suitable MNF bands have been selected from the output on the basis of eigen values and non-noisy appearance in the display and FCCs have been generated using various permutations and combinations. The spectral diversity in the area is best represented by a FCC prepared by assigning red, blue and green color to the 5^{th}, 6^{th}, and 8^{th} MNF bands respectively (Fig. 6.7). With this scheme of color coding the following relationship between color and composition can be made:

- red/yellow/white: are anorthosites (un-shocked anorthosites occur as bright red)
- black/green: are mostly gabbroic/basaltic rocks
- blue: are norites/bronzites
- pink/magenta/purple: are dominantly Mg-spinel anorthosites

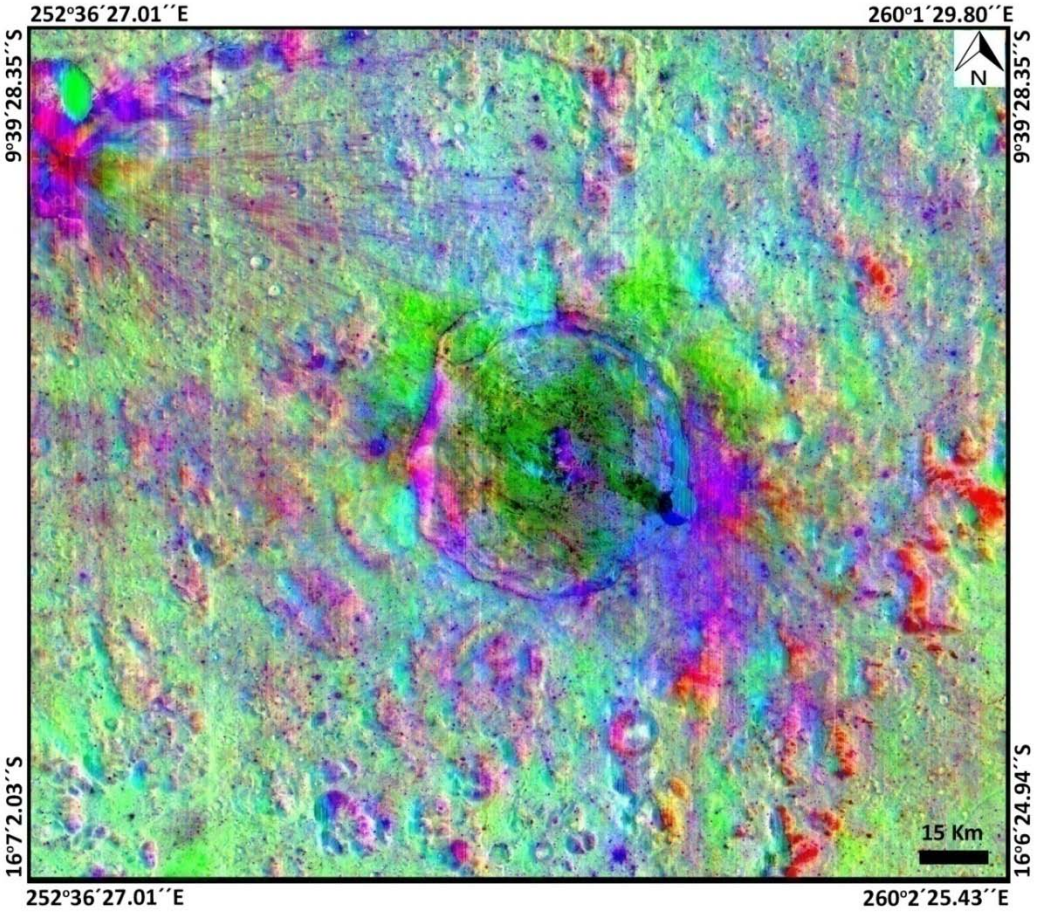

Figure 6.8 M^3 derived MNF based FCC of the Lowell crater region, prepared by assigning red, green and, blue colors to 5^{th}, 6^{th}, and 8^{th} MNF bands respectively. Here, regions appearing as red/yellow/white indicate dominance of anorthosites (most of the un-shocked anorthosites occur bright red in color); black/green: gabbroic/basaltic rocks (occasionally black areas could be troctolite + Mg-spinel / olivine rich gabbro/basalt); blue: norites / bronzites; and pink/magenta/purple: Mg-spinel anorthosites.

In this scheme, the Rook massifs in the southeast quadrant of the study region appear strikingly bright red indicating presence of un-shocked anorthosite exposures of regional dimension. The basalts of a portion of the Lacus Veris pond present in the southeast corner of the study region appear green in color**.** The Lowell crater also shows abundant green areas, indicating possibility of occurrence gabbroic/basaltic areas. A detailed analysis of the spectral variability in various geologic units of the Lowell crater has been provided in the sub-sections 6.5.2 – 6.5.6.

The steep slopes and fresh craters on the string of uplands north of Lowell crater mostly show pink/magenta color indicating possible presence of Mg-spinel anorthosites. Also, at certain locations within these uplands exposures of un-shocked anorthosite have been noticed. In fact, most of the uplands between the Rook Mountains and the Cordillera ring show shades of pink/magenta suggesting possibility of exposures of Mg dominant rocks in them. Isolated exposures of un-shocked anorthosites have also been noticed in this Orientale basin ejecta facie**.** The scarps of Cordillera ring in the northwest quadrant shows exposures of un-shocked anorthosite in red, norite/bronzite in blue and Mg-spinel anorthosites in magenta. Though this MNF based approach has captured major spectral variations in the area relatively well, the pyroclastic deposits (section 6.5.2) could not be mapped in a particular color.

6.5.2 Ejecta blanket

The representative sites (E1-E4) for with spectra have been derived are marked in Fig. 6.9a and the corresponding normal and continuum removed spectra are plotted in Fig. 6.10. Fig. 6.9b shows spectral variability in the equivalent view derived from Fig. 6.8. The ejecta blanket of Lowell crater pose interesting spectral variations. A distinct bifurcated low albedo ejecta sheet is visible on the northern side up to ~2 crater radii from the Lowell crater rim (Fig. 6.4). Only a small portion of these, extending from the walls to the immediate vicinity of the Lowell crater shows yellowish green color (Fig. 6.8 and Fig. 6.9b) suggesting presence of clinopyroxenes (e.g. E1) as the dominant mafic content in the largely anorthositic ejecta (e.g. E2).

Rest of the part of the ejecta blanket, including those in the immediate proximity and the distant ones up to ~2 crater radii from the rim, do not show distinct contrast with the background soils. Thus, it can be inferred that the clinopyroxene bearing rocks, either gabbro or crypto-mare, would have been present at depth in the pre-impact target rock sequence.

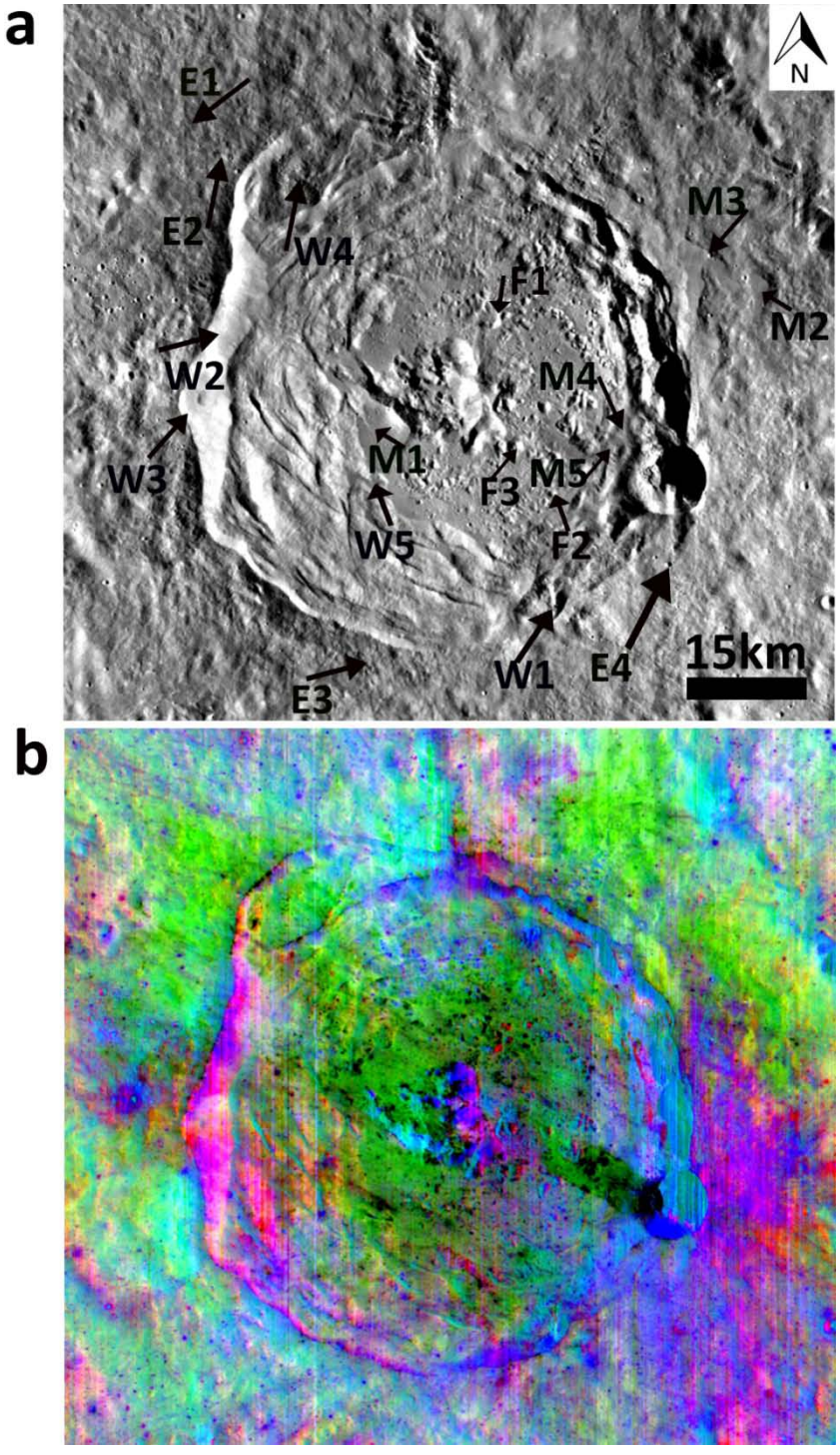

Figure 6.9 a) A blown-up view of the Lowell crater from M^3 750 nm data showing sites for which spectra have been plotted in Fig. 6.9- 6.11; b) Corresponding MNF based FCC.

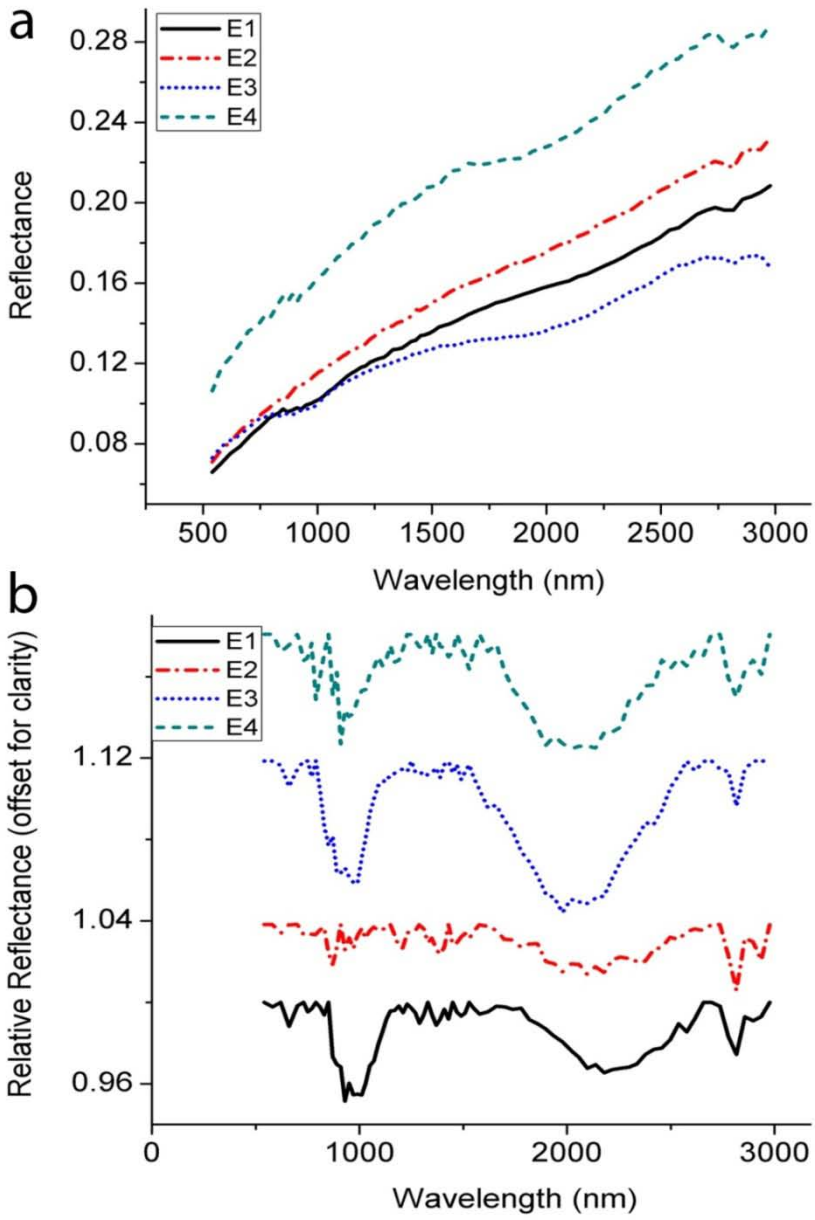

Figure 6.10 Spectral diversity in the ejecta of Lowell crater and Crater S. a) 4 pixel average spectra for sites E1 – E4 marked in Fig. 6.8a; b) corresponding continuum removed spectra. These locales show signatures of clinopyroxene (E1), anorthite (E2), and orthopyroxene (E3, E4).

On the southwestern side, the ejecta material is almost indistinguishable from the background soils. It is interesting to note that tiny fresh craters on the ejecta, both on northern (e.g E3) and on the southern side (about quarter radii from the rim) (e.g. E4) show

Mg rich signatures (norites and/or Mg-spinel anorthosites). On the southeastern side, Lowell crater ejecta, if at all present must be buried under the anorthositic-noritic-Mg-spinel bearing ejecta blanket of Crater S (e.g. E5) which appears in shades of magenta, pink and blue.

6.5.3 Crater wall

The representative sites (W1-W5) for which spectra have been derived are marked in Fig. 6.9a and the corresponding normal and continuum removed spectra are plotted in Fig. 6.11. The Lowell crater wall is largely composed of orthopyroxene dominated rocks (e.g. W1) appearing as blue in Fig. 6.9b. Anorthosites intervene them at number of locations. Both Mg-spinel anorthosites (e.g. W2) and un-shocked anorthosites (e.g. W3) are present, especially on the western side, as revealed by their pink and red appearance respectively.

In the northwestern and northeastern quadrants, material with clinopyroxene as the major mafic content is present which appear in yellowish green colour (e.g. W4). Their continuity with the external gabbroic/basaltic ejecta implies that they also represent ejecta material from Lowell impact event. Few iron rich pyroxene dominant spots have been spotted in the walls (e.g. W5) as minor facie. They occur as dark black spots. Boulders have been noticed in these locations in the TC data with higher spatial resolution.

6.5.4 Floor irregularities

These are leftover blocks that stabilized on the floor of Lowell crater. The representative sites (F1-F3) for which spectra have been derived is marked in Fig. 6.9a and their respective spectra (both normal and continuum removed) are plotted in Fig. 6.12. Most of these appear black/green in the MNF based FCC (Fig. 6.9b) indicating dominance of clinopyroxenes (e.g. F1). Contrary to these, a population of pink/magenta colored blocks occurs in the southeastern quadrant, suggesting their Mg rich composition (e.g. F2).

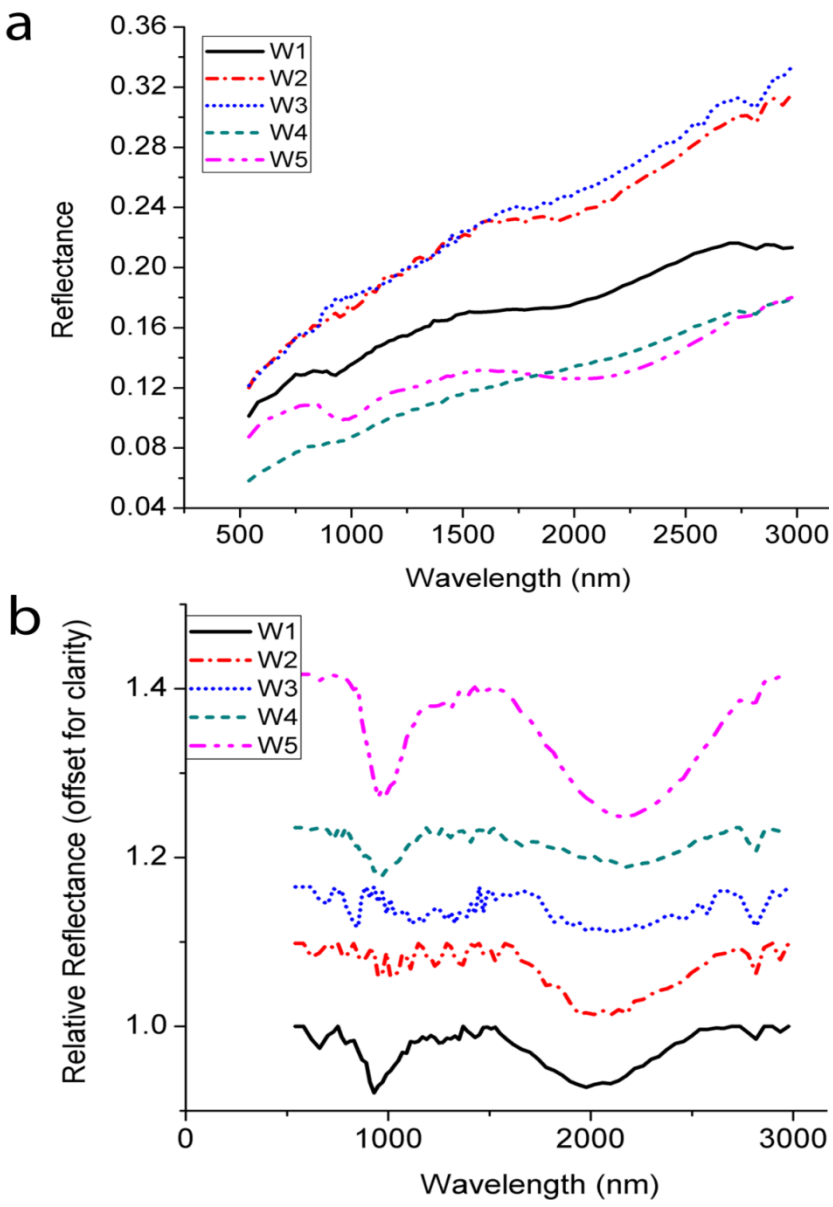

Figure 6.11 Spectral diversity in Lowell crater walls. a) 4 pixel average spectra for sites W1 – W5 marked in Fig. 6.8a; b) corresponding continuum removed spectra. These locales show signatures of low-Ca pyroxene (W1), Mg-spinel (W2), unshocked anorthite (W3), and high-Ca pyroxene (W4, W5).

A few of the floor irregularities (e.g. F3) show bright red color suggesting presence of exposures of un-shocked anorthosites. Interestingly, the southern face of the block marked as F1 show signatures of un-shocked anorthosite whereas rest of the block is dominantly clinopyroxene bearing. Similarly, spectral signature of the block marked as F3

possibly show co-occurrence of Mg-spinel and un-shocked anorthosite. In addition to these, surprisingly, noritic rocks are rare in the floor irregularities. These observations have implications to the compositional make-up of the target rocks (at depth) that were shattered by the Lowell impact event.

6.5.5 Melts

Melts confined to four distinct geologic settings have been identified in the study area. These include those exterior to the Lowell crater, the ones on the Lowell crater floor, melts diverging from Crater S on to the floor of Lowell crater, and the rectilinear recent resurfacing. Representative sample sites (M1- M5) for which spectra have been derived are marked in Fig. 6.9a and their normal and continuum removed spectra are shown in Fig. 6.13.

It is apparent from pervasively greenish to mildly yellowish green appearance of the melts on the floor of the Lowell crater in the MNF based FCC (Fig. 6.9b) that largely clinopyroxene is present in them as a major mafic constituent (e.g. M1). This suggests that gabbroic/basaltic melts were produced during Lowell impact event. However, an exception to this is the southeast quadrant of the Lowell crater floor where melts (present in relatively less quantities) largely appear in mild shades of pink and blue indicating anorthositic-noritic-Mg-spinel bearing composition. Thus, the floor irregularities (section 6.5.4) and the melts in the southeastern quadrant of the Lowell crater bear compositional similarity.

The external melts which are mostly concentrated on the northeastern side of the Lowell crater (Fig. 6.9a) exhibits mixed nature; however, it is largely composed of anorthosites (e.g. M2). A fresh crater in one of the pools shows prominent Mg-spinel anorthosite signature (e.g. M3). Here, it is important to mention that there could be some contamination from the ejecta of the later formed Crater S that formed on the eastern wall of Lowell crater (Fig. 5.1).

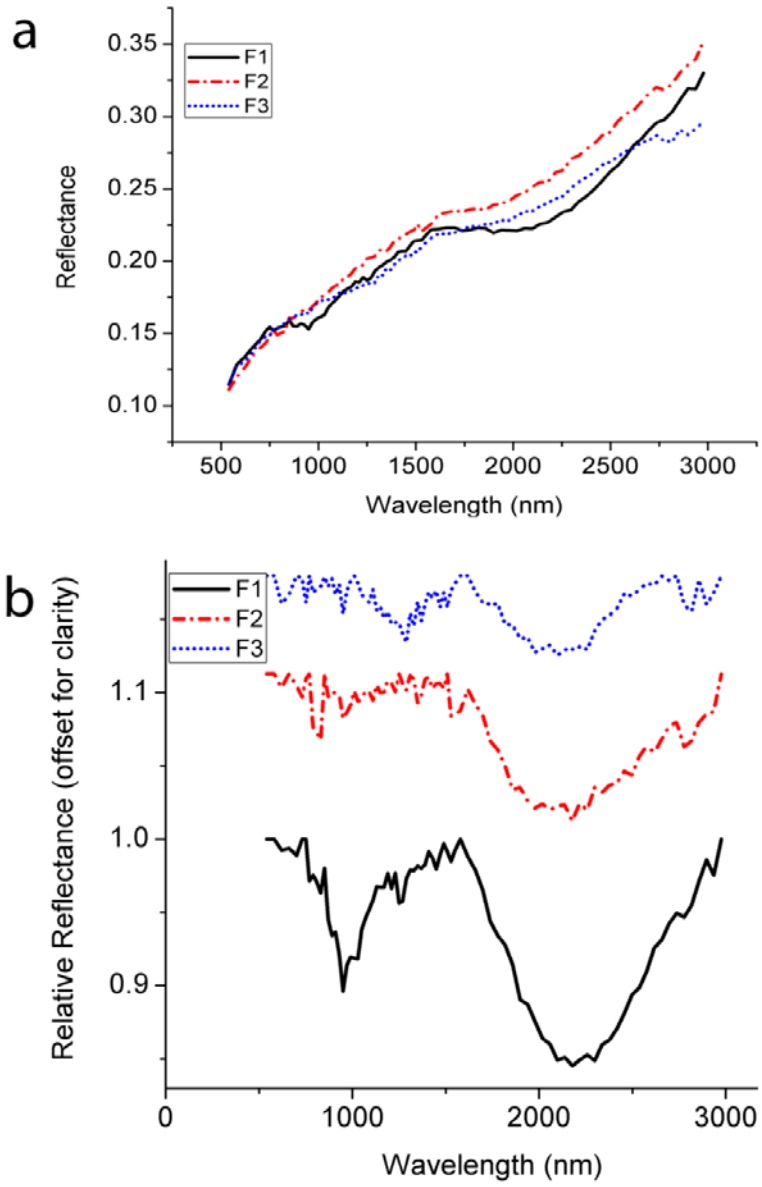

Figure 6.12: Spectral diversity in the floor irregularities. a) 4 pixel average spectra for sites F1 – F3 marked in Fig. 6.9a; b) Corresponding continuum removed spectra. Site F1 shows dominantly gabbroic/basaltic composition, F2 is largely Mg-spinel anorthosite and possibly F3 represents co-existence of un-shocked anorthosite and Mg-spinel.

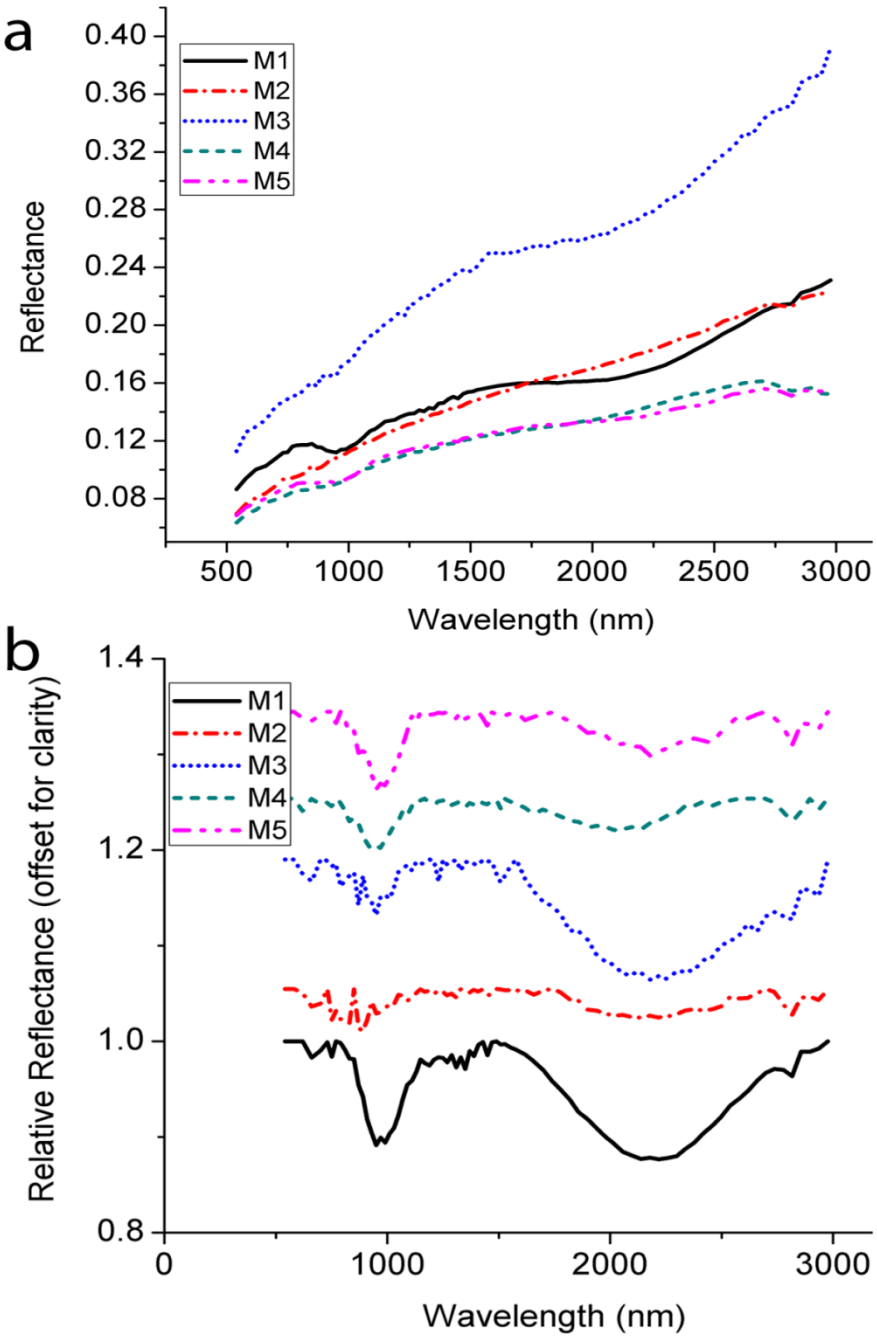

Figure 6.13 Spectral diversity in the melt deposits of Lowell crater. a) 4 pixel average spectra for sites M1 – M5 marked in Fig. 6.8a; b) corresponding continuum removed spectra. These locales show signatures of high-Ca pyroxene (M1, M5), anorthite (M2), Mg-spinel (M3), low-Ca pyroxene (M4).

The impact melts emanating and diverging from Crater S (Fig. 5.7 and Fig. 5.8) appears blue in color in the MNF based FCC (Fig. 6.9b) suggesting dominance of orthopyroxenes as the major mafic constituent (e.g. M4**)**. In contrast, the rectilinear fresh flows (Fig. 5.7 and Fig. 5.8) appear in shades of green and black (Fig. 6.9b) indicating conspicuous presence of clinopyroxenes in them (e.g. M5). This relationship between the Crater S impact melts and the fresh flows has implications to origin of the recent resurfacing (discussed in section 8.2). Further, parts of the Crater S impact melts (referred to as older flows in Fig. 5.8) show signatures of glass (e.g. S7 in Fig. 6.4 and Fig. 6.5) characterized by a broad absorption feature centered beyond ~1 µm (~1.016 µm; Table 6.1) and a distinct high at ~750 µm. Similar criteria have been used to identify glasses in the Aristarchus region (Mustard et al., 2011). A prominent OH/H_2O absorption band is present beyond ~2.8 µm, which suggests that these could be pyroclastic glasses (Srivastava et al., 2013**)**. Strong hydration signatures compared to the surrounding areas have been observed at several well-known pyroclastic deposits across the Moon (Li and Milliken, 2013; Bhattacharya et al., 2013).

6.5.6 Central peak area

As described in section 5.3.2, central peak area would have exposed rocks from maximum depth in the Lowell crater. Therefore, peak lithologies reflect compositional diversity at maximum depth (around the centre of the Lowell crater region) prior to the impact event that formed Lowell crater. However, it is to be noted that certain portions of the central peak area could also be composed of impact melts that were produced during the impact event.

The spectral diversity of the central peak region is revealed in Fig. 6.14 and Fig. 6.15. Fig 6.14a and 6.14b shows blown-up views of the central peak from M^3 750 nm image (shown in Fig. 6.4) and MNF based FCC depicted in Fig. 6.8, respectively. The regions (P1-P5) marked over Fig. 6.14a corresponds to those sites on the central peak for which 4 pixel average spectra have been derived and plotted in Fig. 6.15.

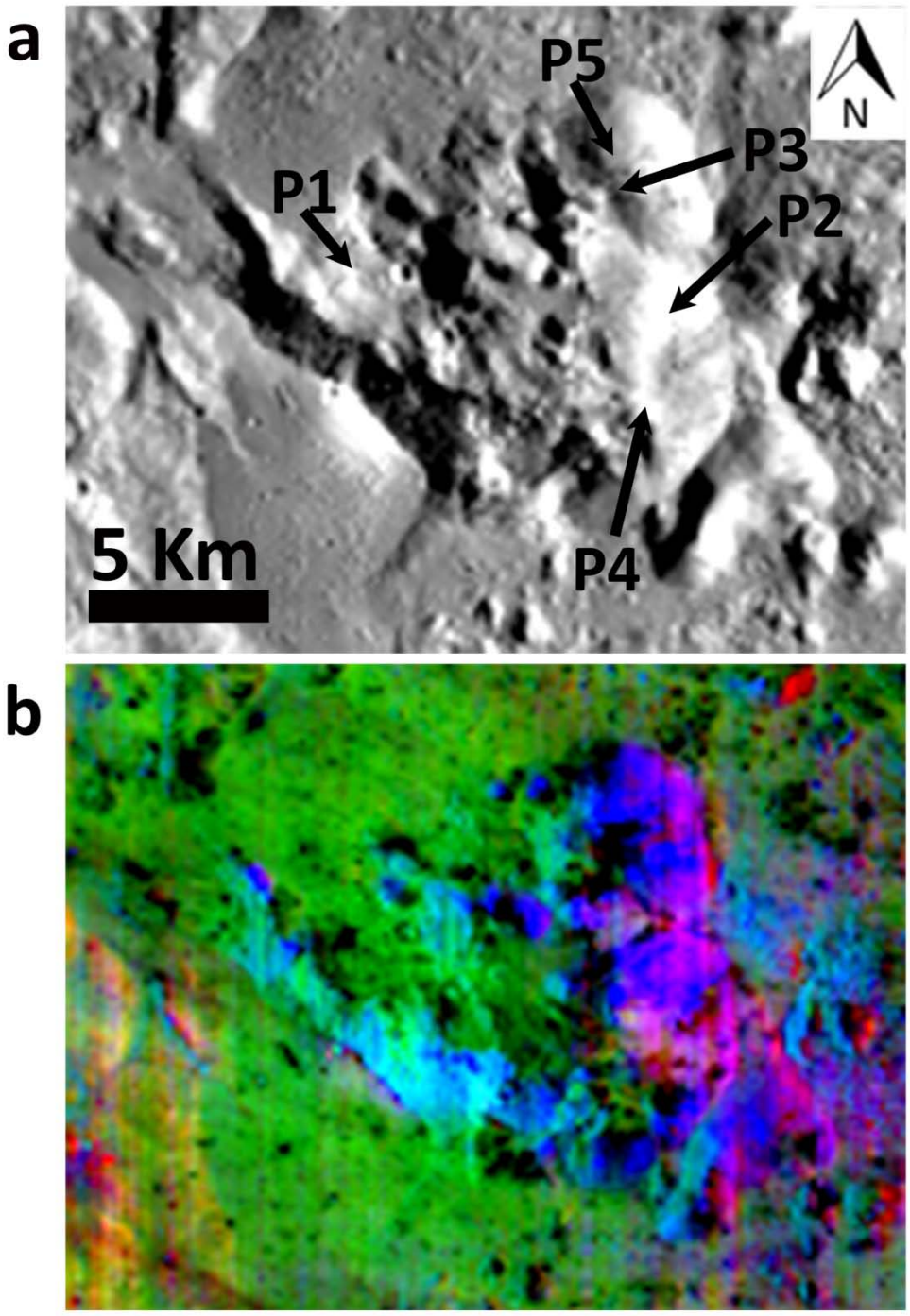

Figure 6.14 a) A blown-up view of the central peak from 750 nm M^3 data showing sites for which spectra have been plotted in Fig. 6.12; b) Corresponding MNF based FCC. Here, P3 represent areas covered with boulders, which mostly appear as conspicuously dark (black) regions.

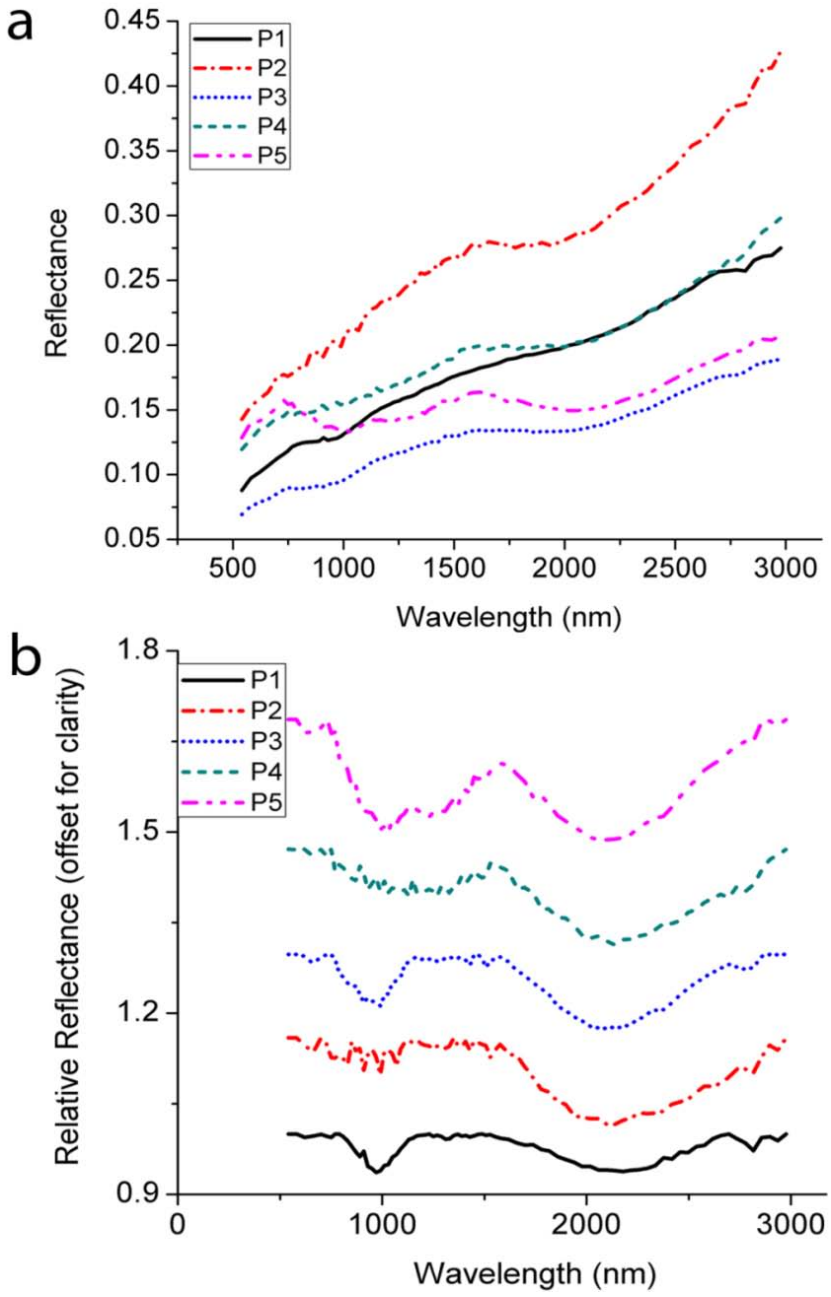

Figure 6.15 Spectral diversity of the Lowell crater central peak. a) 4 pixel average spectra for sites P1 – P5 marked in Fig.6.11; b) corresponding continuum removed spectra. These locales show signatures of high-Ca pyroxene (P1), Mg-spinel (P2), pyroxene (P3) , un-shocked anorthite along with Mg-spinel (P4), olivine alongwith Mg-spinel / pyroxene with high Fe^{+2} at M1 site / coexistence of mafic rocks (P5) and un-shocked anorthite (P6).

As evident from Fig. 6.14b, the central peak of Lowell crater shows distinct W-E color asymmetry suggesting distinct differences in composition. The western side largely appears in shades of green (e.g. P1) indicating presence of gabbroic/basaltic rocks. However, the eastern side (a part of which is comprised of distinct slumping) occurs in shades of pink/magenta, blue and red suggesting presence of Mg-spinel anorthosite exposures (e.g. P2), orthopyroxene (e.g. P3) and un-shocked anorthosite (e.g. P4).

Several dark (black) patches are also present on the central peak both on the western and on the eastern side (e.g. sites S3 in Fig. 6.4 and P5 in Fig. 6.14). Most of these areas show strong 1 µm and 2 µm bands and a distinct and deep curved inflexion beyond ~1 µm region of the spectra. Zoomed view of these locations in the TC data (Fig. 5.5) has revealed that most of these areas correspond to patches of boulders on to the central peak. Their spectra appear to be analogous to spectra of some of the young (~1 Ga) olivine rich basalts on the western nearside (Staid et al., 2011; Varatharajan et al., 2014). Therefore, either these exposures represent similar rock types or they represent signatures of Mg-spinel troctolites. The other possibilities could be that they represent iron rich pyroxenes with Fe^{+2} at the M1 site or co-existence of iron rich pyroxenes and un-shocked anorthosites.

Thus, cumulatively the central peak shows spectral signatures of clinopyroxene, orthopyroxene, Mg-spinel, olivine and un-shocked anorthosite. The assemblage is consistent with minerals expected in a differentiated mafic pluton; possibly, of Mg-suite variety. Therefore, the Lowell crater would have excavated and exhumed a mafic pluton possibly of Mg-suite nature. The origin and emplacement of boulders on the central peak is the key to understand the exact nature of this mafic pluton.

Table 6.1 Location of the sites in the Lowell crater region for which 4 pixel average spectra have been derived in the study. S1-S8: Sites marked in Fig. 6.4 for which spectra are plotted in Fig. 6.5; E1-E4, W1-W5, F1-F3, and M1-M5 (respective sites in ejecta, walls, floor irregularities, and melt ponds of the Lowell crater) are marked in Fig. 6.9 and their corresponding spectra are marked in Figures 6.10 – 6.13; P1-P5, the central peak sites marked in Fig. 6.14 and their respective spectra are shown in Fig. 6.15.

Site	**Location**		**Band centre (~1000 nm)**		**Band centre (~2000 nm)**	
			Estimated	**Anticipated**	**Estimated**	**Anticipated**
S1	16°6′43.49′′ S	253°38′52.82′′ E	992.2	970	2128	2137.8
S2	13°22′55.38′′ S	257°31′54.69′′ E	955.5	930.1	2023.4	2018.0
S3	13°5′18.39′′ S	252°58′42.15′′ E	982.6/1101.8	950.1	2097.3	2097.9
S4	14°46′3.61′′ S	257°48′36.05′′ E	1265.9	1269.4	X	x
S5	12°54′29.37′′ S	256°41′32.09′′ E	X	x	X	x
S6	13°4′22.76′′ S	256°37′31.02′′ E	X	x	2055.3	2097.9
S7	13°8′23.83′′ S	257°26′58.00′′ E	1016.3	1049.9	1967.6	1858.3
S8	13°22′55.38′′ S	253°4′34.48′′ E	X	x	X	x
E1	11°48′2.49′′ S	255°31′4.15′′ E	975.4	990	2195.5	2177.7
E2	11°56′41.71′′ S	255°38′29.19′′ E	X	x	X	X
E3	14°2′10.41′′ S	256°14′20.25′′ E	943	990	2051.6	2097.9
E4	13°38′41.10′′ S	257°30′40.52′′ E	957.3	950.1	2031.7	2018.0
W1	13°51′39.93′′ S	257°0′41.79′′ E	938.5	930.1	2036.6	1978.1
W2	12°38′6.56′′ S	255°38′29.19′′ E	X	x	2052.2	2097.9
W3	13°0′58.78′′ S	255°30′27.06′′ E	1218.1	1329.3	X	x
W4	12°1′56.95′′ S	256°1′2.88′′ E	981.3	970.0	2169.2	2177.7
W5	13°18′17.22′′ S	256°18′21.32′′ E	998.4	990.0	2104.8	2097.9
F1	12°36′15.29′′ S	256°48′38.59′′ E	983.2	950.1	2101.2	2097.9
F2	13°20′27.03′′ S	257°3′10.14′′ E	X	x	2060.3	2058.0
F3	13°8′23.83′′ S	256°53′16.74′′ E	1267	1289.4	2053.2	2097.9
M1	13°5′18.39′′ S	256°18′2.77′′ E	988.7	990.0	2118.3	2137.8
M2	12°27′36.07′′ S	257°54′28.38′′ E	X	x	X	x
M3	12°20′48.11′′ S	257°42′6.63′′ E	X	x	2079.0	2058.0
M4	13°4′4.22′′ S	257°22′1.30′′ E	957.5	930.1	2023.6	2018.0
M5	13°10′52.18′′ S	257°18′37.32′′ E	971.5	950.1	2144.3	2177.7
P1	12°52′1.020′′ S	256°23′18.02′′ E	979.8	970.0	2122.7	2177.7
P2	12°52′56.65′′ S	256°41′32.09′′ E	X	X	2064.0	2097.9
P3	12°48′37.04′′ S	256°38′26.65′′ E	953.4	990.0	2083.3	2057.9
P4	12°57′34.80′′ S	256°42′9.180′′ E	1139.4	1129.7	2064.0	x
P5	12°46′27.23′′ S	256°37′49.56′′ E	1003/1079.4	1029.9	2084.7	2058.0

6.6 Mg-spinel distribution in Orientale basin

Plausible spectral signatures of Mg-spinel exposures with little or no mafic silicates have been found in every non-mare geological setting inside the Orientale basin. These include exposures in the Hevelius formation (HF), Montes Rook Formation (MRF), Cordillera Ring (CR), Outer Rook Ring (ORR), and Inner Rook Ring (IRR). However, the number of exposures and specific rock associations vary from one setting to the other.

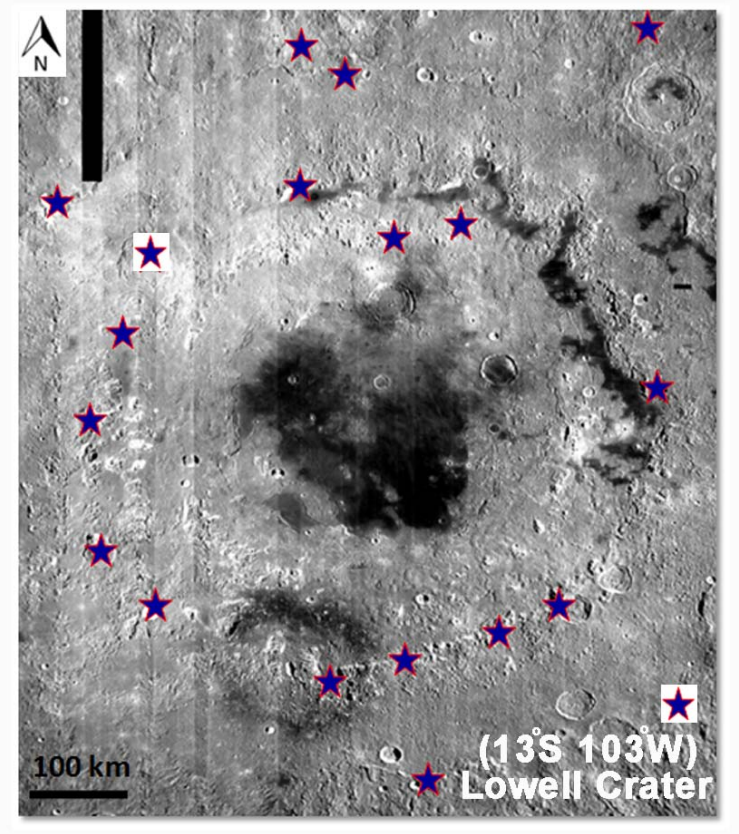

Figure 6.16 M^3 750 nm image mosaic showing distribution of plausible Mg-spinel anorthosite exposures in the non mare units of Orientale basin.

In the HF unit, discrete areas on the walls and floor of some of the fresh craters show Mg-spinel signatures. The accompanying rocks in the adjacent areas are rich in pyroxene. Prominent Mg-spinel signatures have been observed in important geological units of MRF such as in the Lowell crater (Srivastava and Gupta, 2012, 2013; Sun et al., 2013). The accompanying rocks generally show signatures of orthopyroxene.

Among the rings, the Cordillera Ring (CR) shows only few Mg-spinel rich zones. The accompanying rock is generally anorthosite with few exposures of orthopyroxene in some areas. The Outer Rook Ring (ORR) shows numerous discrete Mg-spinel dominant zones with pyroxene dominant rock types in the adjacent areas. Interestingly, contrary to the expectations, the Inner Rook Ring (IRR) is largely devoid of Mg-spinel. It is mostly anorthositic in composition and shows signatures of both shocked and unshocked varieties. Only two Mg-spinel exposures have been observed in the IRR and these are also found to be associated with un-shocked anorthosites. These findings have implications to the plausible origin of recently discovered Mg spinel anorthosites on the Moon (discussed in section 8.3).

6.7 Summary

Spectral diversity in the Lowell crater region has been worked out using representative average spectral reflectance curves, popularly used FCC's (based on integrated band depth and band ratios), and a MNF based color coding scheme. The MNF based FCC effectively capture the spectral variability in the Lowell crater region. The areas surrounding Lowell crater, which are the best approximates for the surface lithology of the Lowell target, largely show presence of massifs of un-shocked anorthosites, anorthosites, Mg-spinel anorthoisites, basalts (of Lacus Veris), and mature soils.

The Lowell crater wall is largely composed of norite to anorthositic norite with intermittent anorthosite and Mg-spinel rich areas. The floor of the Lowell crater is largely occupied with gabbroic/basaltic melts and the floor irregularities also show conspicuous clinopyroxene signatures. A part of the proximal ejecta, which is nearest to the Lowell crater in the northwestern and northeastern quadrants also show presence of clinopyroxene. The central peak shows distinct compositional asymmetry. The rocks on the western side of the peak shows gabbroic/basaltic signature, whereas the ones on the eastern side (mostly coinciding with the slumped zone) are largely Mg-rich (low-Ca pyroxene and Mg-spinel bearing rocks).

Anomalous spectral signatures showing prominent curved inflexion ~1.25 μm (along with prominent 1 μm and 2 μm absorption feature) have been noticed at several

spots on the central peak and at certain sites in the walls. Most of these correspond with the areas showing presence of boulders and could relate to presence of Mg-spinel troctolites or co-association of pyroxene and un-shocked anorthosite, or the 1.25 μm could be due to Fe^{+2} at the M1 site of pyroxene.

These observations from the Lowell crater indicate that the Lowell impact event would have excavated a deep seated mafic pluton in addition to the Orientale basin ejecta of anorthositic to anorthositic norite composition. The origin of the boulders on the central peak may provide clues to decipher exact nature of the mafic pluton. .

A search for Mg-spinel anorthosite exposures in the other non-mare areas of the Orientale basin have revealed that they occur in each of them (i.e. in the CR, HF, ORR and IRR); however, a distinct scarcity exists in the IRR, which is supposed to have exhumed rocks from deeper levels in the Orientale region. Further, in most of the observed occurrences, noritic rocks are present in the adjacent areas. The rock association in the IRR is only un-shocked plagioclase.

The composition of the recently produced resurfacing is gabbroic/basaltic. However, the older flows (i.e. the impact melts from Crater S) largely show noritic signatures consistent with the composition of the wall of Crater S, emphasizing further that all these flows may not be co-genetic and that the fresh gabbroic/basaltic flows could have an alternate origin possibly volcanic (?). Few signatures of pyroclasts have also been noticed in the area supporting the volcanic preposition.

Chapter 7

Crater count analysis

7.1 Introduction

The age of Lowell crater has been debated in the past. According to McEwen et al. (1993), initially the Lowell crater was mapped as Imbrian by Scott et al. (1977) but observations from Galileo multi-spectral data indicated that it could be Copernican in age. However it was maintained that the Lowell's Copernican status is doubtful due to superposition of rays from Crater S - the superposed Copernican crater on its eastern wall (Fig. 5.1). The newly available high spatial resolution image data for the region has enabled resolving this uncertainty and assigning a specific age to the Lowell crater using popularly used crater chronology technique.

Besides dating Lowell crater, crater density of the recent resurfacing on its eastern side (Fig. 5.8) has been used to assess plausible time of formation for this distinct geological unit inside Lowell crater. Surface topography, morphology and spectrally derived composition for this recent resurfacing have been discussed in Chapters 5 and 6.

7.2 Crater chronology

How do we know, how old a feature on the Moon or on Mars is? In absence of rock samples from these distant locations (except for very few Apollo and Luna sample return sites on the Moon), these questions are largely answered on the basis of crater chronology, which involves relative age dating of planetary surfaces by determining impact crater density (Neukum et al., 1975; Neukum and Köing, 1976). For using impact crater density as a chronological tool, it is essential to understand beforehand the origin of the impactors and the variation in their flux since birth of our solar system.

Our solar system evolved from dust and gas which condensed to form small mm sized bodies. These small bodies collided to give rise to meter-kilometer sized planetesimals by a process known as accretionary growth wherein the particles collide and coalesce with each other to form a larger planetary body. These kilometer sized bodies continued to collide with each other resulting in formation of larger planets (e.g. Lynden-Bell and Pringle, 1974; Hartmann, 1999; Montmerle et al., 2006). Therefore, it is apparent that the population of impactors was enormous during the early phase of the development of our solar system and the flux reduced with time (Fig. 7.1).

The issue is whether the decay was uniformly exponential (as shown by solid line in Fig. 7.1) or there was a spike in the impact mass flux around ~3.9 Ga, as suggested by clustering of the radiometric ages of lunar basins (derived from lunar samples) around that time. This inferred spike in the impactor population is traditionally termed as Cataclysm or Late Heavy Bombardment (LHB) and is shown by dashed line in the Fig. 7.1. Though this idea of cataclysm or LHB is still debated (Hartmann, 2003; Spudis et al., 2011), it is generally largely accepted.

It is understood that most of the impactors causing LHB were derived from the asteroid belt ~ 3.9 - 4 Ga (e.g. Ivanov, 2001; Ivanov et al., 2002; Morbidelli et al., 2001).

At the time of the formation of our solar system ~4.5 Ga ago, the various planetary bodies conformed to orbits quite different from their present ones. It is possible that due to the gravitational forces in the young solar system, the objects might have migrated to their current position ~4 Ga, triggering the LHB event.

Thus, a major phase of impact cratering event in our solar system was possibly driven by the LHB event. Thereafter, flux of impactor has remained almost constant (Fig. 7.1). Accordingly, we have broadly two populations of impactors, one that visited during the period of LHB and the other that came thereafter.

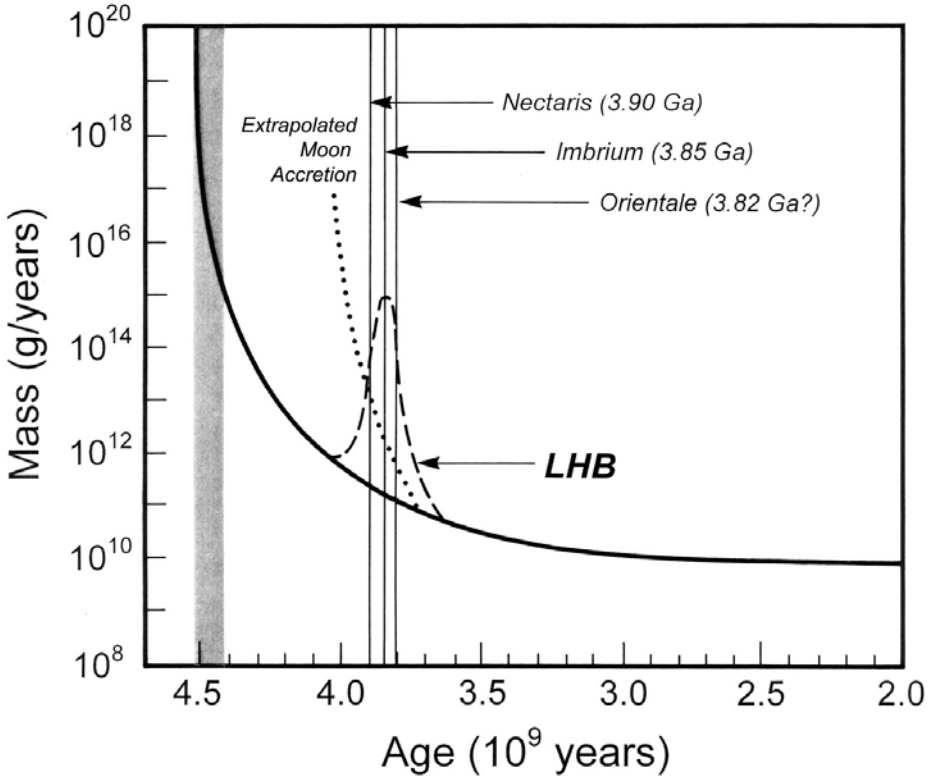

Figure 7.1 Terrestrial impact fluxes showing exponential decay (solid line). The late heavy bombardment (LHB) or the cataclysm is represented by dashed curve. Radiometric ages of few selected impact basins on the Moon are marked [Source: Koeberl, (2006)]**.**

Relative age dating of planetary surfaces in contact with each other is basically dependent on 'Law of order of superposition'. Where the contact is missing or for non-contacting surfaces relative crater density and in some cases, preservation of morphology

of the surface features is commonly used criterion for determining the sequence of their formation. The fresh surfaces show sharp and well preserved morphological features and low crater density. In contrast, the old surfaces show subdued and degraded morphologies and the crater density is also higher. For example, the smooth lunar mare plains are relatively younger compared to the intensely cratered highlands in the adjacent areas (Fig. 7.2).

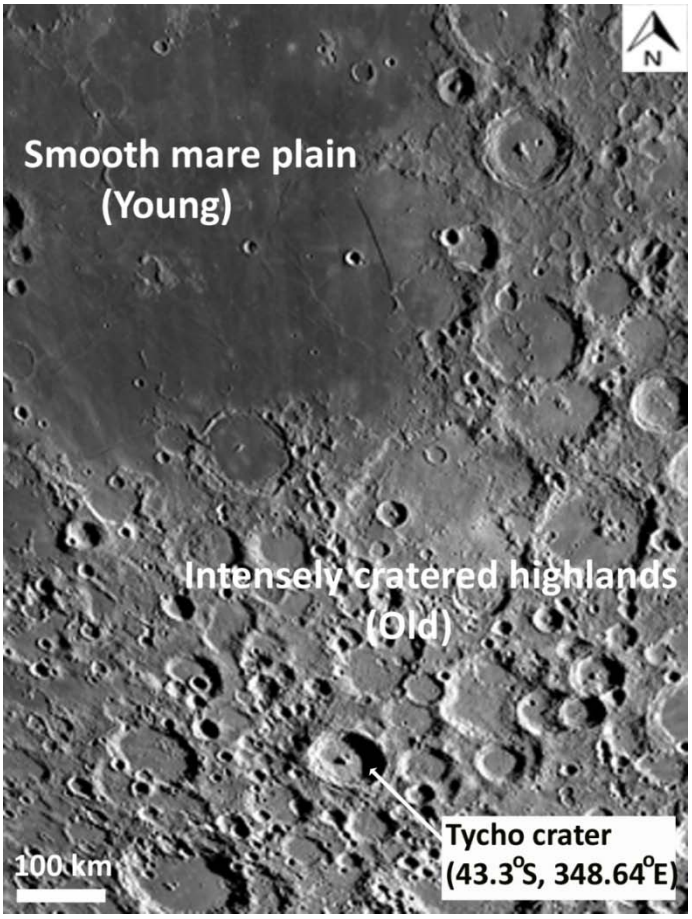

Figure 7.2 LROC-WAC mosaic of a part of the Moon on the southern nearside showing smooth and young lava plains adjacent to relatively older cratered highlands. [Image source: modified after spectacular view of near side of the Moon at lroc.sese.asu.edu]

Further, to assign absolute age to an unknown surface, a calibration between radiometric ages of the Apollo and Luna rock samples from known provenances of the Moon and the corresponding crater density in the area has been established (e.g. Jessberger et al., 1977; Hartmann et al., 1981; Neukum, 1983; Deutsch and Stöffler, 1987; Neukum

and Ivanov, 1994; Stöffler and Ryder, 2001). Although crater chronology technique was developed for the Earth's Moon, it has been extrapolated with suitable assumptions and theoretical considerations to derive surface ages of other planetary bodies in the solar system as well (e.g., Ivanov et al., 2002; Stöffler et al., 2006).

At present high resolution satellite images of the planetary surfaces such as TMC (Chandrayaan-1), TC (Kaguya) and LROC-NAC (LRO) for the Moon and HiRISE (MRO) from Mars etc. are available. In order to facilitate precise crater counting and to find the absolute age of a surface, many image processing and GIS based techniques are being regularly developed (e.g. Michael and Neukum., 2008, 2010; Kneissl et al., 2011).

Crater chronology involves fitting the observed crater size-frequency distribution (CSFD) of a surface unit to a known production function, and to use the crater frequency for certain crater sizes together with a calibrating chronology function to obtain an absolute age (e,g, Neukum and Ivanov 1994; Hartmann et al., 2000; Ivanov et al., 1999; Neukum et al., 2001; Michael and Neukum, 2010).

The methodology used is expressed in a flowchart (Fig. 7.3). The cumulative crater frequency normalized to a unit area is plotted against the crater size and the production function is shifted until it fits the data points, thus, enabling a read out of the cumulative frequency at a standard crater diameter. This cumulative frequency value, say for crater of D = 1 km, is used to obtain model age from the chronology function.

Therefore summarily, the crater chronology technique for an area is executed in the following sequence: a) Determination of CSFD; b) Fitting production function; and c) Estimating age from chronology function.

7.2.1 Basic assumptions

There are three fundamental assumptions for carrying out crater chronology studies. These include the following: a) The particle flux is constant over the entire lunar surface; b) the frequency of craters produced by impactors can be measured with respect to size of the craters; and c) the area of interest to be dated is a homogenous unit (e.g. Hartmann et al., 2000; Neukum et al., 2001; Hiesinger et al., 2003; Stoffler et al., 2006)

7.2.2 CSFD determination

The CSFD quantifies the number of craters per unit area as a function of crater size. The size of the crater (generally diameter) and the frequency of the crater distribution (number of craters per unit area) on the surface are the two basic parameters that control the crater density of a particular surface. In order to establish a CSFD plot, the craters on the surface are counted taking account of the above mentioned assumptions and cumulative crater frequency is plotted against the crater diameter in logarithmic scale. The craters are counted manually or automatically (using crater detection algorithms) on digital images using image processing / GIS softwares. The ArcMap toolbar "CraterTools" is a popular tool commonly used for carrying out crater chronology studies.

The minimum size of the crater which can be mapped on a surface depends upon the type of the geological features, quality of the image (high angle/low angle and its spatial resolution) and also the processes modifying the crater population in different size ranges. Various endogenic and exogenic factors affect crater counting and thereby affecting crater size frequency distribution on the surface of a planetary body (e.g. Neukum, 1983; Hartmann and Neukum, 2001; Stoffler et al., 2006; Arya et al., 2012; McEwen and Bierhaus, 2006) . The major ones include: a) magma flooding and presence of volcanic craters; b) ejecta blanketing; c) secondary cratering; d) superposition of impact craters; and e) mass wasting.

The lava flows superposed over a surface can obliterate small craters, partially bury craters of intermediate sizes, and can have least effect on the larger craters. Thus, a count of large craters in an area might give relative age of the older basement rocks and the small craters may give exposure age of the present basaltic surface. Due to this affect, the CSFD shows irregularity when a major magmatic flooding has occurred in an area. Further, volcanic craters also occur in the mare areas along with impact craters. Compared to the impact craters they are generally non-circular in shape, show subdued appearance, and exhibit broken rim. Such craters are identified and are not included in the crater counting.

When a fresh crater is formed, it radially throws material outward from the point of impact, forming huge ejecta blanket. The nature of the ejecta blanket depends upon

velocity of the impactor, direction and angle of impact, and target characteristics. These ejecta material can blanket their surroundings up to hundreds of meters (in height) depending on the distance from the crater formed. Thus, they could bury previously formed craters resulting into anomalous CSFD behavior.

Further, on fall back, larger chunks of the ejected material form their own craters, which are called “secondary craters” since they were formed as a consequence of the formation of primary crater. The secondary craters are mostly small, shallow, elongated in shape, and they form crater chain or clusters. During crater counting, these are identified and are not included in determination of CSFD. The smaller crater population in an area is most prone to contaminations from secondary craters (McEwen and Bierhaus, 2006).

Superposition of craters and landslide activity on slopes (mostly due to formation of craters in an adjacent area) are common processes of surface degradation on the Moon. If the size of the superposed crater is greater than the crater population underneath it will completely destroy the details of the earlier formed craters. However, if the size is comparatively small it will result in abrasion of the larger pre-existing crater (or any other feature on the Moon, such as a lava flow lobe).

The superposition mostly affects the smaller sized craters and the crater size distribution approaches a state of equilibrium. Similarly, small craters that form on slopes degrade quickly due to land slide activity; therefore, areas with steep slopes, such as those commonly found on the crater walls and central peak should be avoided.

Another major factor which has drawn the attention during recent times is the dependence of crater density on the target rock characteristics (e.g. van der Bogert et al., 2013). For example, a surface composed of hard rock surface show higher crater density compared to the harder impact melts even though they formed during similar time frame. Similarly, crater density for similar aged surfaces comprising of hard rock and loose regolith is also different causing uncertainty in the age estimation from crater chronology technique.

7.2.3 Production function

Numerous studies of the cratering records in the solar system have been carried out till date to understand the actual form of the CSFD of impact craters formed on a fresh geologic surface but a precise form still eludes, at least partly due to scarcity of sufficient large sized freshly produced/uniform surfaces (Neukum, 1983; Neukum and Ivanov, 1994; Hartmann et al., 2000; Neukum et al., 2001; Stoffler et al., 2006;). The planets have complex cratering history where crater production and degradation occur simultaneously. However, Neukum (1983) and Neukum et al. (2001)**,** with generalized outcomes developed a production function known as Neukum Production Function (NPF), which describes formation of number of craters of a particular size in relation to the number of craters of any other size.

Neukum et al. (2001) worked out a polynomial fit to the cumulative number of craters, N per sq. km. with diameters larger than a particular diameter D. For the time period of 1 Ga, N(D) may be expressed as:

$$\log_{10}(N) = a_0 + \sum_{n=1}^{11} a_n [\log_{10}(D)]^n$$

Here, D is in km and N is the number of craters with diameters >D per km^2 per Ga. This equation is valid for D = 0.01 km - 300 km.

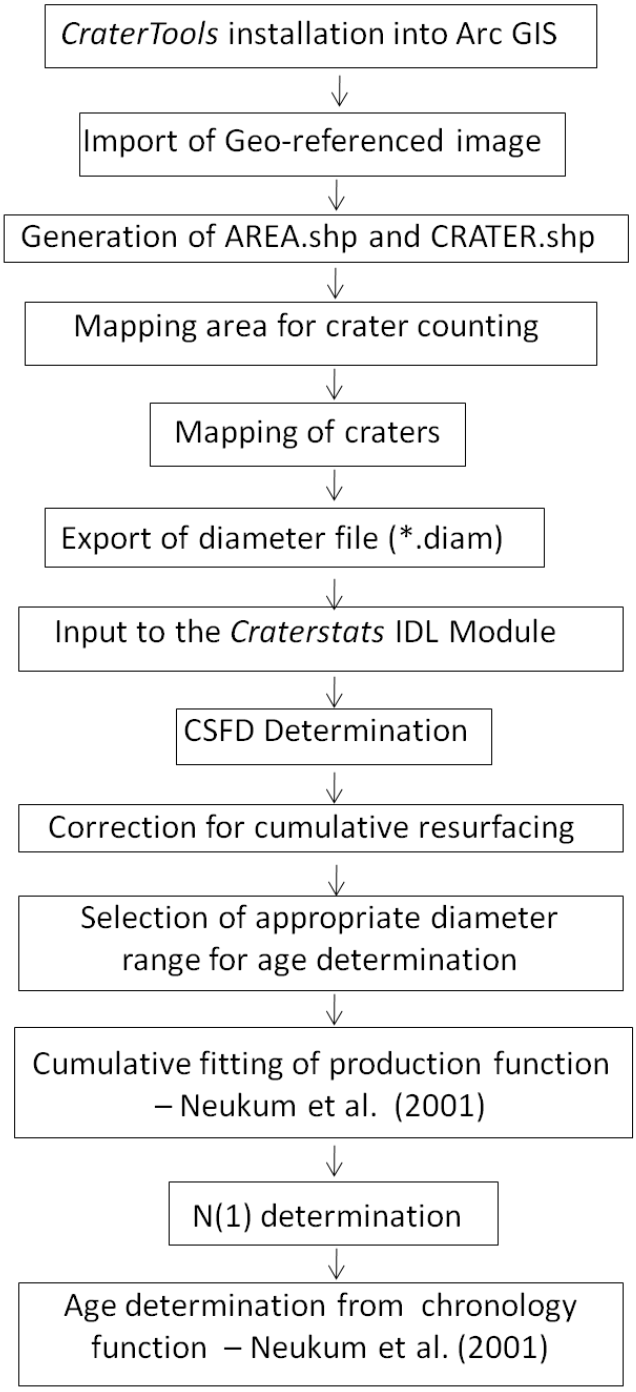

Figure 7.3 Methodology flow-chart for deriving surface age using crater chronology

7.2.4 Chronology function

Neukum (1983) and Neukum et al. (2001) derived a chronology function using CSFD of the various sites on the Moon for which inferred/or radiometric age estimates are available (Fig. 7.4).

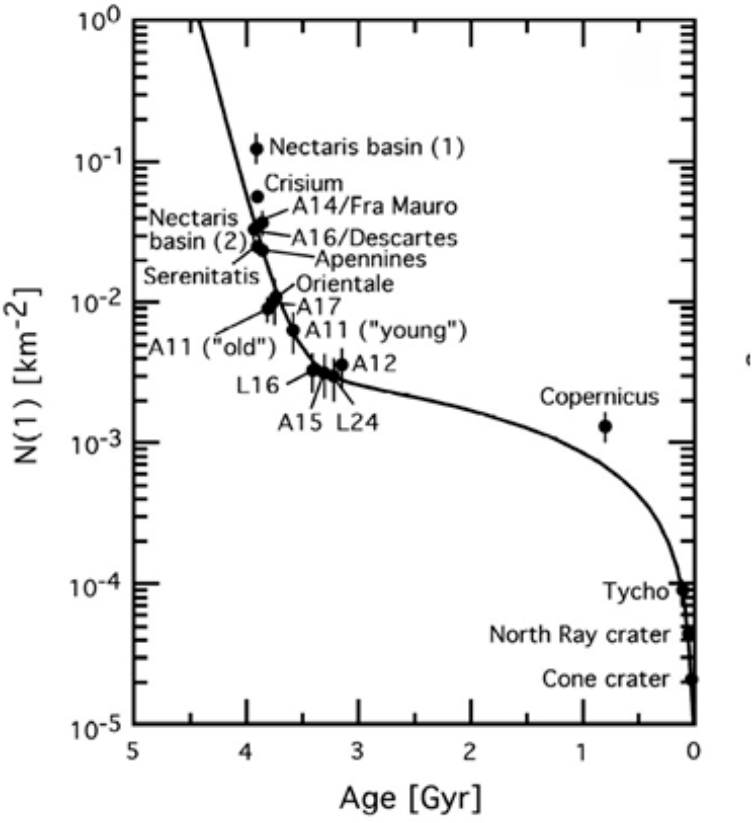

Figure 7.4 The chronology function – A graphical representation. [Source: Neukum et al., 2001]

Analytically, the chronology function is expressed as:

$$N(1) = 5.44\text{x}10^{-14}[\exp(6.93T) - 1] + 8.38\text{x}10^{-4}T$$

Subsequent to fitting of the production function, the CSFD value for 1 km diameter crater is derived and the value is substituted in the equation to calculate age of the surface mapped. Here, N(1) is the cumulative crater frequency per km^2 at D=1 km and T is the crater accumulation time (crater retention age) in Ga.

7.3 Age estimates in the study area

7.3.1 Lowell Crater

A flat surface devoid of any resurfacing and/or any ghost crater is ideal for applying crater chronology technique. However, availability of such an ideal surface for age dating of the Lowell crater is a difficult preposition, since it has formed over a hilly terrain "the Montes Rook", and major part of its ejecta blanket on the eastern side (if at all present) would have been buried under the ejecta of Crater S – the superposed crater (Fig. 5.1 and Fig. 5.17). To add to the woes, the Lowell crater floor is covered with mostly impact melts and/or some possible volcanic flows (?), and there are numerous floor irregularities.

Therefore, in order to narrow down to the most suitable area for crater counting, information gathered from topographical, morphological and compositional studies discussed in chapters 5 and 6 have been used. Especially, the MNF based FCC depicting compositional variations in the Lowell crater region (Fig. 6.8) helped to limit the coverage of the area chosen for crater counting. Mostly parts of the proximal ejecta appearing yellowish green in the color composite have been selected.

Two separate areas have been selected for crater counting in the Terrain Camera (TC) image mosaic of the Lowell crater. These areas are situated in the NW and NE quadrants of the scene and are referred here as A1 and A2 sites respectively (Fig. 7.5). The area and the craters therein have been mapped using CraterTools extension of Arc- GIS. The areal coverage of A1 and A2 are ~782.6 km^2 and ~696.2 km^2 respectively and the diameter range of the crater mapped is 30 m – 600 m. Total number of craters counted in sites A1 and A2 are 982 and 2729 respectively. Separately age computations have been made for A1 and A2 and finally, a single age estimate has been derived for the Lowell crater based on the cumulative data for both the sites (i.e., A1+A2).

Chronology function and production function defined by Neukum et al. (2001) for the Moon is used to determine the age in this study. The production curve is initially fitted for larger craters and thereafter smaller craters are added until the fit deviates. 75 craters in A1 and 89 craters in A2 in the size range 200 m - 600 m have been used to fit the

production function. The data plot for A1 is shown in Fig. 7.4, for site A2 in Fig. 7.5, and for cumulative area (A1 + A2) in Fig. 7.6. The age estimates for Lowell crater from sites A1 and A2 are 364±41 Ma (Fig. 7.4) and 396±41 Ma (Fig. 7.5) respectively. The cumulative crater count gives an age of 374±28 Ma to the Lowell crater (Fig. 7.6).

7.3.2 Recent resurfacing

The recent resurfacing possibly confined to a graben (Fig. 5.8 and Fig. 5.9) shows conspicuous scarcity of impact craters (Fig. 5.11 and Fig. 5.12) (Srivastava et al., 2011, 2013). Except for a single crater on the low viscosity flow (marked as Flow 1 in Fig. 5.11), not even a single crater has been observed in the other part of the flows that can be confidently classed as a primary impact crater based on their morphology. In contrast, the older surfaces in adjoining areas comprising of impact melts from Crater S and parts of Lowell original crater floor (Fig. 5.7, Fig. 5.11 and Fig. 5.12) show presence of numerous impact craters. Therefore, the flows are quite fresh compared the Lowell crater and even to the Crater S.

Only three likely impact craters >30 m in diameter are in present in ~5.5 km^2 area occupied by the youngest lobed flows showing levees and channels (Fig. 5.10). This frequency of impact craters is comparable to that described for ~2-10 m.y. old Ina feature where a crater density of 2-7 plausible craters >30 m (in diameter) was observed in an 8 km^2 area (Schultz et al., 2006). Therefore, drawing similarity in crater density of these two regions, the youngest flows (i.e. flow 3) could be ~2-10 Ma old.

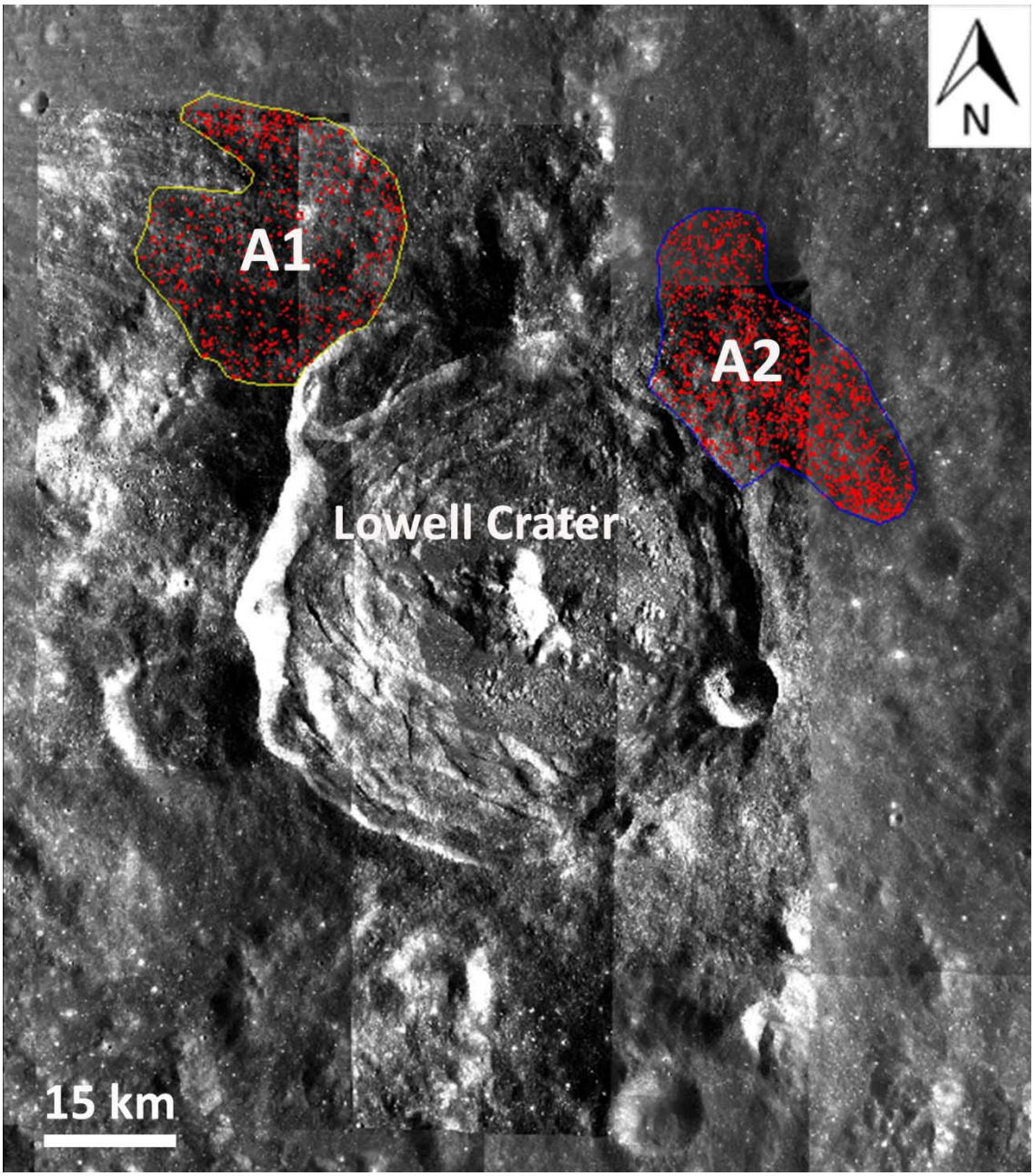

Figure 7.5 TC mosaic of the Lowell crater showing areas (A1 and A2) selected for crater counting (on the proximal ejecta blanket of the Lowell crater) and the craters mapped in them. The areal extent of A1 and A2 is ~782.6 km^2 and ~696.2 km^2 respectively.

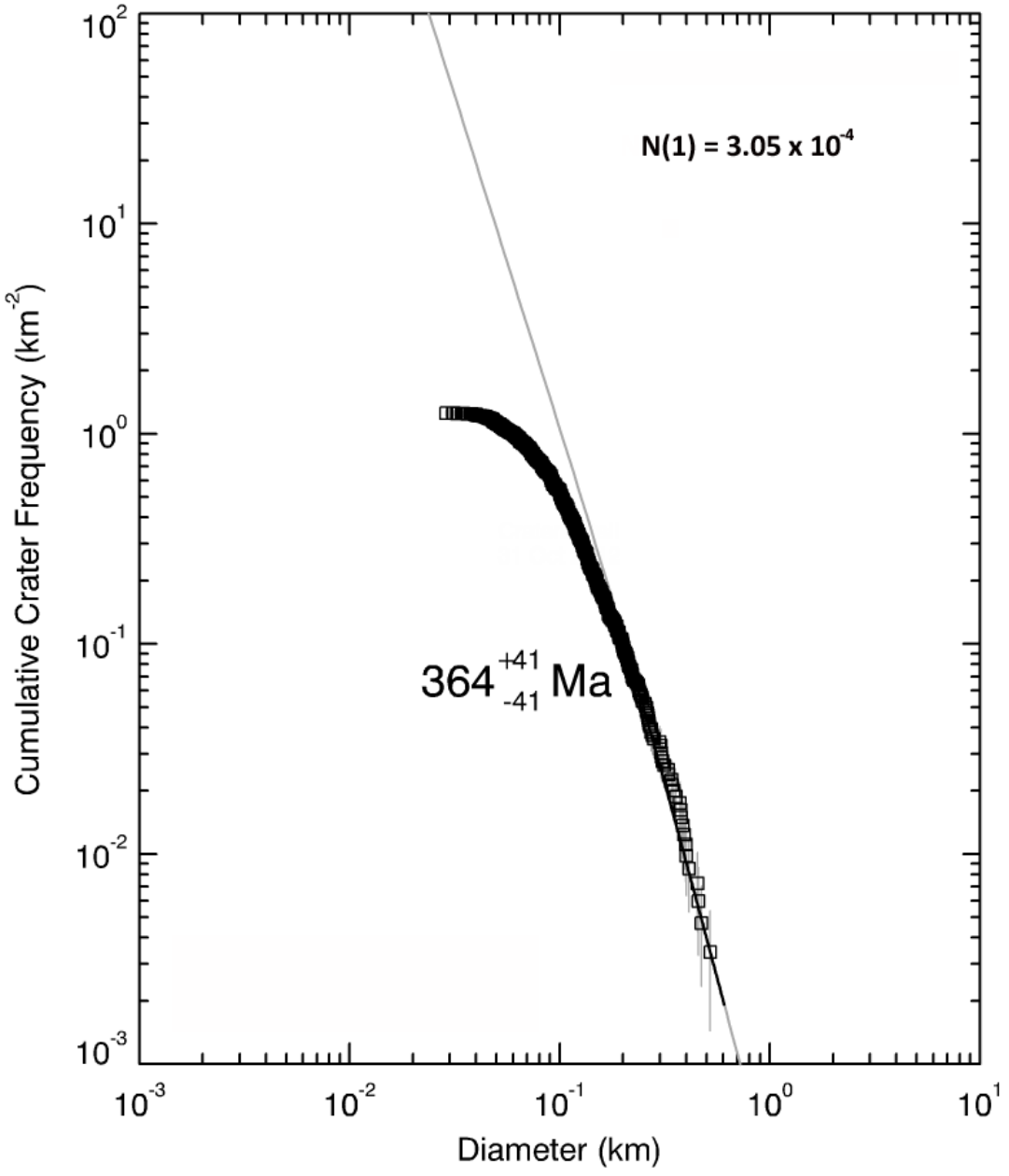

Figure 7.6 CSFD plot with fitted production function for craters counted in area A1 marked in figure 7.4. Here, the production function and chronology function of Neukum et al. (2001) has been used to derive age. 75 craters have been used in curve fitting and the estimated age is 364±28 Ma.

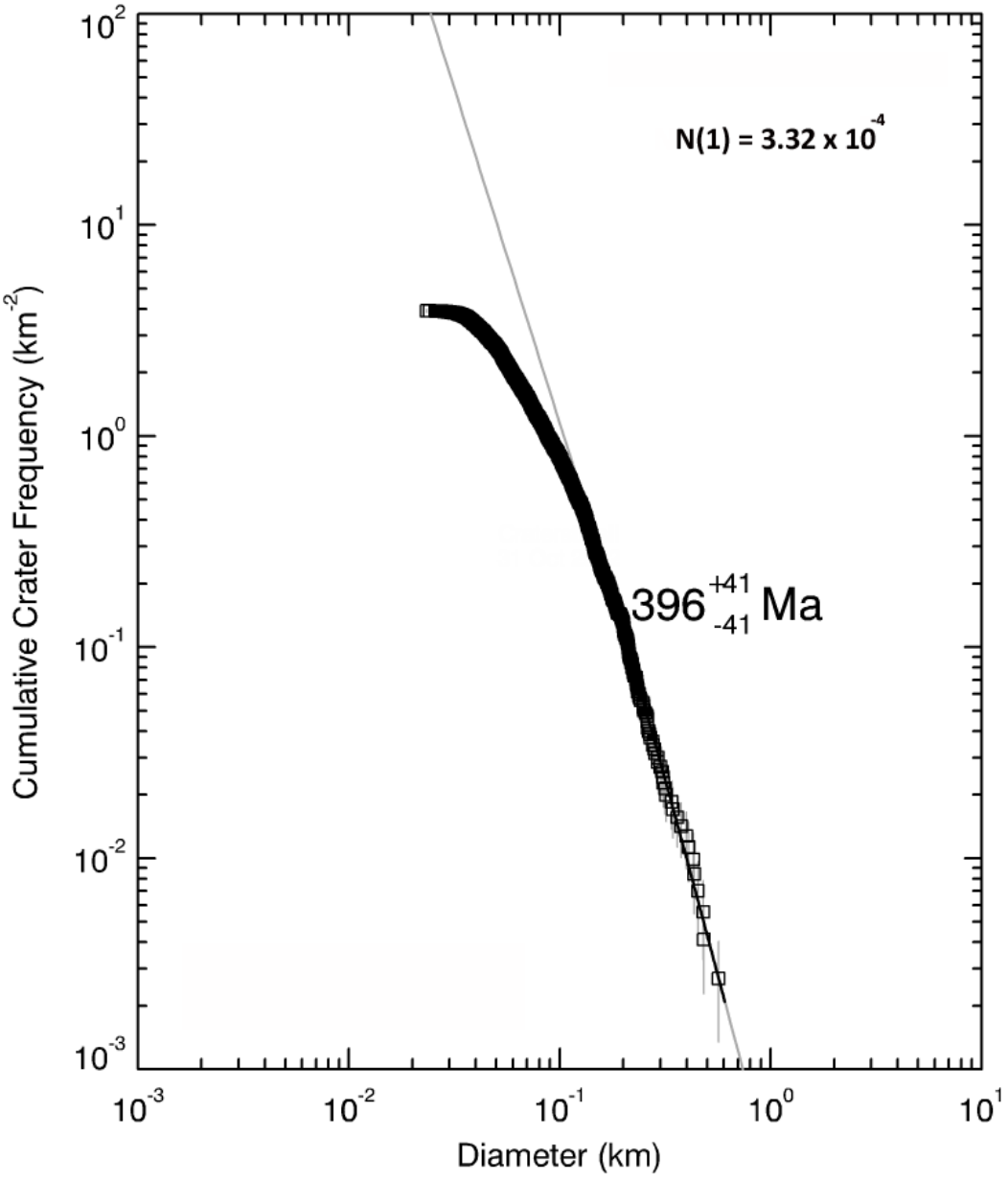

Figure 7.7 CSFD plot with fitted production function for craters counted in area A1 marked in figure 7.4. Here, the production function and chronology function of Neukum et al. (2001) has been used to derive age. 89 craters have been used in curve fitting and the estimated age is 396±41 Ma.

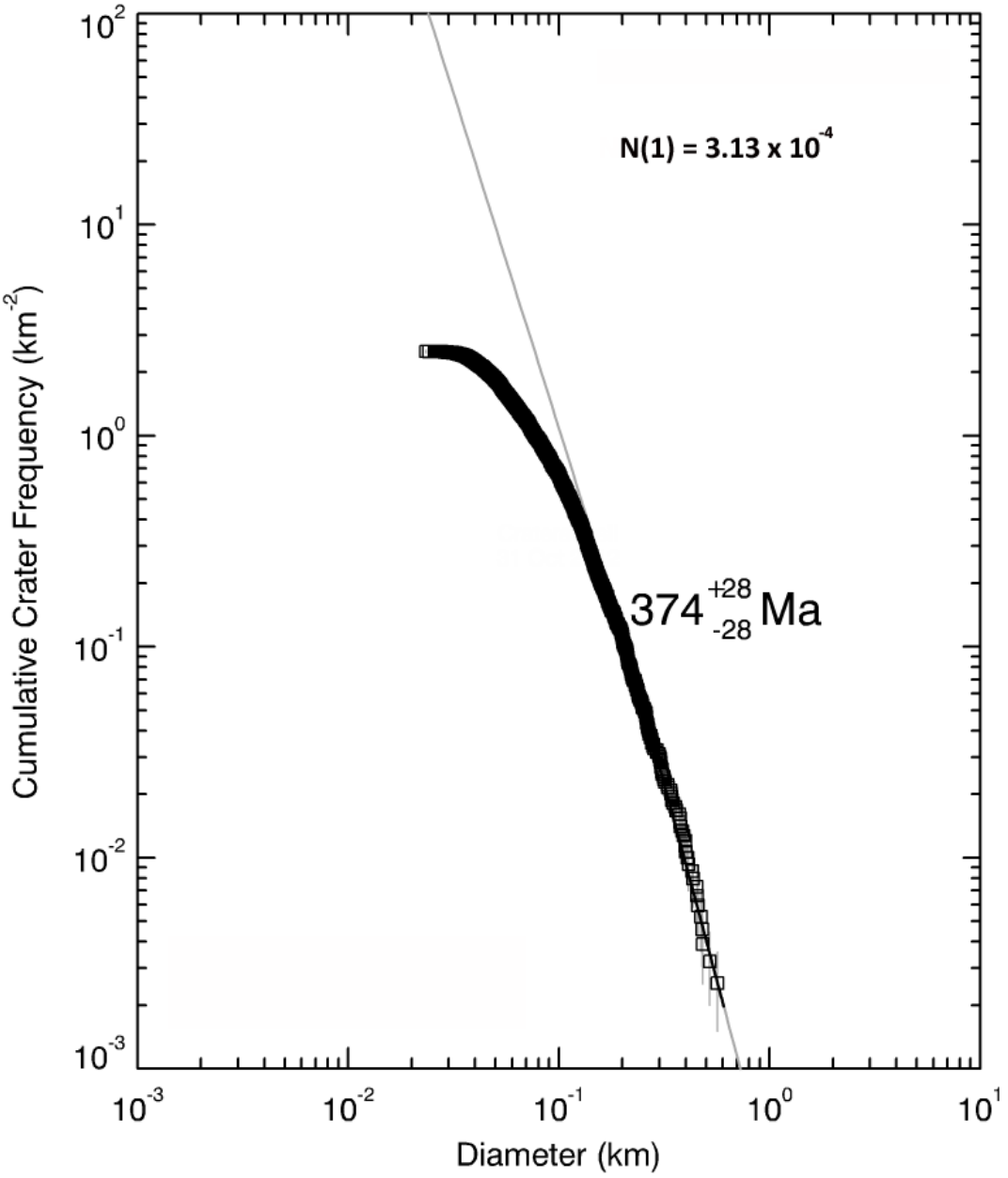

Figure 7.8 CSFD plot with fitted production function for craters counted in cumulative area (A1+A2) marked in figure 7.4. Here, the production function and chronology function of Neukum et al. (2001) has been used to derive age. 164 craters have been used in curve fitting and the estimated age is 374±28 Ma.

7.4 Summary

Dating of planetary surfaces is a difficult preposition since usually samples are not available for them (except for few known provenances on the Moon). The crater chronology technique (with a few assumptions) enables us to find out absolute ages of planetary surfaces of the solar system. The technique involves CSFD determination, fitting of a production curve and age determination using a chronology function. Using this technique, the Lowell crater has been found to be 374±28 Ma old. Therefore, it is Copernican in age consistent with the possibility put forward by McEwen et al. (1993) based on Galileo spectral reflectance data (to check).

The Lowell crater is anomalous in the population of other contemporaneous Copernican craters such as Aristarchus, King, and Tycho, since prominent visible rays are not manifested in the Lowell crater. This could be due to lack of contrast between the mafic materials (gabbroic/basaltic/noritic) ejected from Lowell impact event and the low albedo mature surroundings mostly composed of anorthosites to anorthositic norite.

The recent resurfacing on the eastern wall of Lowell crater could have formed much after the formation of the Lowell crater. Parts of the resurfacing could be barely ~2-10 Ma old.

Chapter 8

Synthesis and conclusions

The interpretations derived from morphological, spectral, and crater count analyses (chapters 5 - 7) of the Lowell crater region have been synthesized here. The main aim is to throw light on the nature and characteristics of the Lowell impact event, origin of the recent resurfacing, source of Mg-spinel anorthosites exposures in the Orientale basin and working out geological evolution of the Lowell crater region. Finally, the results obtained in this work are summarized.

8.1 Nature and characteristics of Lowell impact event

The ejecta distribution (including exterior impact melts) and variations in the rim and wall topography of a crater are the key indicators of the angle and direction of impact

event that led to the formation of the crater (Melosh, 1989; Pierazzo and Melosh, 2000; Krüger et al., 2013). Among the ejected materials, distribution of the exterior impact melt deposits provides clues to the direction of the impact since in most of the cases they are emplaced in the downrange direction. Further, slumping and terracing on the crater walls is generally less, and rims have higher elevation in the downrange direction. The angle of impact is mostly determined based on circularity of the crater; ejecta symmetry and slope of the walls. If the impactor hits the target at angles $\geq 15^{o}$, the crater formed is largely circular; for angles $< 30^{o}$ the crater wall on the uprange direction is steeper compared to the walls on the downrange direction; and, at angles $<45^{o}$ the ejecta deposits show asymmetric ejecta distribution (Gault and Wedikind, 1978; Pierazzo and Melosh, 2000).

In the case of the Lowell crater (Fig. 5.17) most of the ejecta is concentrated in the northern areas, and exterior melt pools are concentrated in the northeastern direction. The western walls especially the southwestern part show pronounced slumping and terracing much higher compared to the eastern walls, and the rim on the eastern side is generally slightly lower compared to the western parts. Except for the variations in rim elevation, all these observations indicate that the Lowell crater must have formed due to an oblique hit from the S-SW direction.

Further, the Lowell crater is largely circular, its walls in the downrange direction are steeper compared to the walls in the uprange direction, and the ejecta distribution is asymmetric suggesting that the angle of impact could be ~30^{o}-45^{o}. Therefore, the impactor forming the Lowell crater would have approached the surface at an angle of about 30^{o} - 45^{o} from the S-SW direction.

The uncertainties in the precise assessment of the impacting conditions of the Lowell crater are largely due to the pre-existing topography of the area and the effect of later formed Crater S. As evident from regional topography of the region (Fig. 5.1 and Fig. 5.2), the general direction of topographic slope in the Lowell crater region is from west to east. Such a setting would promote slumping on the east facing slopes and would also result in the observed lower topographic elevations of the eastern side rim. In addition, the ejecta blanket of the subsequently formed Crater S would have covered parts of ejecta from

the Lowell impact event, which may cause error in estimation of Lowell's original ejecta distribution.

8.2 Origin of the recent resurfacing

A recently formed distinct rectilinear resurfaced unit has been located on the eastern side of the Lowell crater (Fig. 5.6 - Fig. 5.16). The unit is ~3-5 km wide and extends to ~17 km from the floor of Crater S (the superposed crater on the Lowell crater), terminating approximately half way to the central peak of the Lowell crater. The resurfacing shows marked scarcity of impact craters therefore it is quite fresh. It shows morphological features (such as superposed lobed flows, possible volcanic vents etc.) characteristic of a volcanic terrain indicating that they could have formed due to recent volcanic activity. However, on the Moon impact melts associated with Copernican craters also show features analogous to those commonly observed in volcanic terrains (e.g., Bray et al., 2010; Denevi et al., 2012). Therefore, deciphering their explicit origin is a difficult task and the issue has been aptly debated (Storm and Fielder, 1968, 1970; Heather and Dunkin, 2003; Chauhan et al., 2012).

Volcanic theory cites crater count differences between the resurfacings and the host crater surface as the key evidence for post impact volcanic modifications of these recently formed craters. However, evidences such as (a) lack of unambiguous melt sources, (b) proximity in distribution between melt and ejecta, and (c) the conventionally accepted idea of cessation of volcanic activity on the Moon prior to ~1 Ga, have been cited in support of an impact melt origin for various resurfacing flows with a fresh appearance (Howard and Wilshire, 1975; Hawke and Head, 1977; Denevi, et al., 2012).

In this case i.e. for the recent resurfacing under consideration, a close association of the rectilinear resurfacing with Crater S makes a strong case for it being composed of impact melts from Crater S. However, here these channelized flows (possibly confined to a pre-existing graben) have been found to superpose relatively older melts emanating and spreading from the Crater S (Fig. 5.7 and Fig. 5.8). There is a significant crater density contrast between the melts emanating and spreading from Crater S and the fresh

superposed flows confined to the channel; therefore, all of these flows may not be co-genetic.

Further, it is commonly understood that impact melt exhibits composition similar to their source rock. However, in this case it is interesting to note that the older flows emanating and diverging from Crater S show noritic composition consistent with the composition of the walls of Crater S; whereas, the fresh superposed flows confined to the rectilinear channel is largely gabbroic/basaltic in composition. Therefore, in the MNF based FCC (Fig. 6.9) the older melts occur in shades of blue whereas the fresh flows appear in shades of black and green. The basaltic/gabbroic composition for the fresh resurfacing can be explained in one of the following ways:

- Melting of a pre-existing gabbroic/basaltic melt pond on the Lowell crater wall that formed during Lowell impact event
- The target site for Crater S had a gabbroic pluton emplaced within the Lowell crater wall similar to the ones shown by El-Baz, (1970) for the King crater
- The target site experienced late stage mare intrusions from one or more sources with plausible assistance from Lowell and Crater S impact events

A necessary requirement for all the three scenarios is the presence of a gabbroic/basaltic body in the pre-impact target base of the Lowell crater. This is quite plausible, as discrete exposures of gabbros/basalts have also been spotted elsewhere inside the Lowell crater, which indicate that the Lowell crater might have been formed by impact on a basaltic unit (existing in continuation of the adjoining Lacus Veris) and/or on a gabbroic pluton of the highland unit. However, the chances for the fresh resurfacing being completely derived from melting of a pre-existing gabbroic pond in the Lowell crater wall or from a gabbroic pluton is minimal since the ejecta blanket of Crater S and the older melts are largely devoid of gabbroic/basaltic signatures. Therefore, only the third preposition advocating late stage mare intrusion seems feasible.

In addition to these, parts of the older flows show signature of pyroclastic glasses characterized by a noisy spectra, broad absorption feature centered beyond 1 μm, and a distinct high at ~750 μm (S7 in Fig. 6.4 and Fig. 6.5). Similar criteria have been used to

identify glasses in the Aristarchus and other regions on the Moon (Mustard et al., 2011; Besse et al., 2014). A prominent OH/H_2O absorption band is also present beyond 2.8 μm, suggesting that these could be pyroclastic glasses. Strong hydration signatures compared to the surrounding areas have been observed at several well-known pyroclastic deposits across the Moon (Li and Milliken, 2013). Further, the freshly built channelized resurfaced unit being studied here appears as a unique dark patch in the 9th MNF derivative (Fig. 8.1)**,** indicating its distinct spectral character in the region.

It may be worthwhile to re-iterate that not even a single crater has been identified on the fresh resurfacing that can be confidently considered as a primary crater. Therefore, the fresh viscous surfaces could be unusually young. Only 3 probable impact craters > ~30 m in diameter have been identified in ~5.5 km^2 area occupied by the youngest lobed flows descending down the Lowell crater walls (Fig. 5.10). This is comparable to that of the Ina feature, where 2 – 7 plausible craters >30 m in diameter were observed in 8 km^2 area (Schultz et al., 2006); therefore, the youngest flows in this recently built formation could be contemporaneous to the age of Ina i.e. they could be barely ~2-10 Ma old.

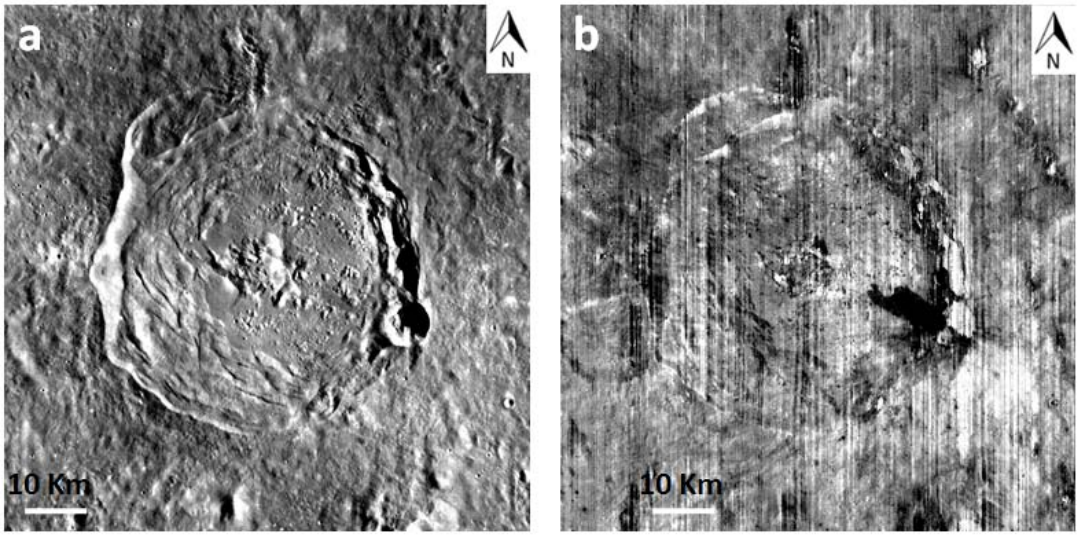

Figure 8.1 a) 750 nm image mosaic of the Lowell crater; b) MNF 9 derivative of M^3 data showing the recent formation as a unique dark patch in the region.

A reasonable hypothesis based on the observed surface topography, morphology, spectral reflectance characteristics, and crater density (Fig. 5.7 - Fig. 5.17) would be that,

the freshly produced superposed flows confined only to the proposed graben could have formed due to recent effusive basaltic eruptions from single or multiple sources following an explosive phase producing the pyroclasts (Srivastava et al., 2013). These flows might have got emplaced much after the formation and emplacement of the melts from Crater S. However, studies on thermal modelling, mechanism for ascent of magma and geochemical characteristics are further suggested for greater understanding in this regard.

It may also be noted that the Lowell crater and Crater S lie in an extensional regime, in the Rook Mountains where faults and dykes are likely to be present (Head, 1974; Whitten et al., 2011). Further, many small mare ponds have been recently reported to occur along the rings of the Orientale basin, in addition to the known ones in Lacus Veris and Lacus Autumni, and some of them are as young as the youngest basalts in Oceanus Procellarum (Whitten et al., 2011; Cho et al., 2012). To account for their occurrence outside Procellarum KREEP Terrain (PKT), it has been proposed that possibly the mantle beneath Orientale basin may be enriched in heat producing elements and/or hotter conditions prevailed in the initial mantle (Cho et al., 2012). Thus, recent igneous activity associated with active lunar interior might be possible theoretically in the Orientale basin especially along the rings. It is interesting to note that the Apollo 15 orbital mass spectrometer detected a rapid burst of volatiles NW of Mare Orientale (Hodges et al., 1973; Crotts, 2008) that may be related to volcanism/extrusion from the lunar interior.

8.3 Origin of Mg-spinel in Orientale basin

Mg-spinel dominant rock exposures showing absence of mafic minerals, olivine and/or pyroxenes, have been reported from certain areas on the Moon using data from NASA's Moon Mineral Mapper (M^3) onboard Chandrayaan-1, India's first mission to the Moon. They were discovered on the far-side of the Moon along the ring of Moscoviense basin (Pieters et al., 2011). Since then, possible exposures have been reported from several other sites on the Moon such as central peaks of Theophilus crater and Tycho crater, region around Endymion crater, floor irregularity of Copernicus crater and in most of the geologic units of Lowell crater (Dhingra et al., 2011; Dhingra and Pieters, 2011; Lal et al., 2012;

Bhattacharya et al., 2012; Kaur et al., 2012; Srivastava and Gupta 2012; Sun et al., 2013; Srivastava et al., 2013).

The mode of formation of this newly discovered rock type on the Moon is not clearly understood in the current perspective about the evolution of the Moon. Most of these exposures have been reported from similar geologic settings, i.e., along the rings of basins and large craters. Hence, it is envisaged that plausibly most of these rock exposures constitute previously deep-seated rocks which have been exhumed on to the surface due to impacts. Finding similar exposures at other locations on the Moon is essential to test this hypothesis, to constrain the extent of these rocks in the lunar crust and to understand the petrographic conditions for its formation (Dhingra et al., 2011; Bhattacharya et al., 2012; Srivastava and Gupta, 2012).

The finding of plausible exposures of Mg-spinel anorthosites in the Lowell crater prompted a search for similar exposures in other highland units of the multi-ring Orientale basin. These regions were investigated to decipher the geologic settings in which Mg-spinel dominant rocks occur and to find out association of mineral assemblages in their adjacent areas.

Possible Mg-spinel dominant rock exposures along with pervasive mafic co-occurrence of pyroxene rich rocks (mostly orthopyroxene) in the adjacent areas have been noticed in the HF, MRF and ORR, which would have sampled rocks from different depths (Srivastava and Gupta, 2013). There distribution of Mg-spinel anorthosite exposures in the Orientale basin is shown in Fig. 6.16. The maximum number of Mg-spinel exposures have been noticed in the ORR; however, Mg-spinel exposures are scarce the IRR, which is supposed to have sampled rocks from deeper level indicating that a uniform Mg-spinel rich pervasive layer may not be present in the region.

Further, Mg-spinel must have been present alongside pyroxene dominated rocks at a comparatively shallower depth (compared to the depth sampled by IRR). This scenario could be possible in case most of the Mg-spinels were produced apriori, due to melt - wall rock reaction (Prissel et al., 2012, 2013) during ancient pre-Orientale magmatism. A possible scenario depicting the formation and distribution of Mg-spinel exposures in the Orientale basin is schematically shown in Fig. 8.1.

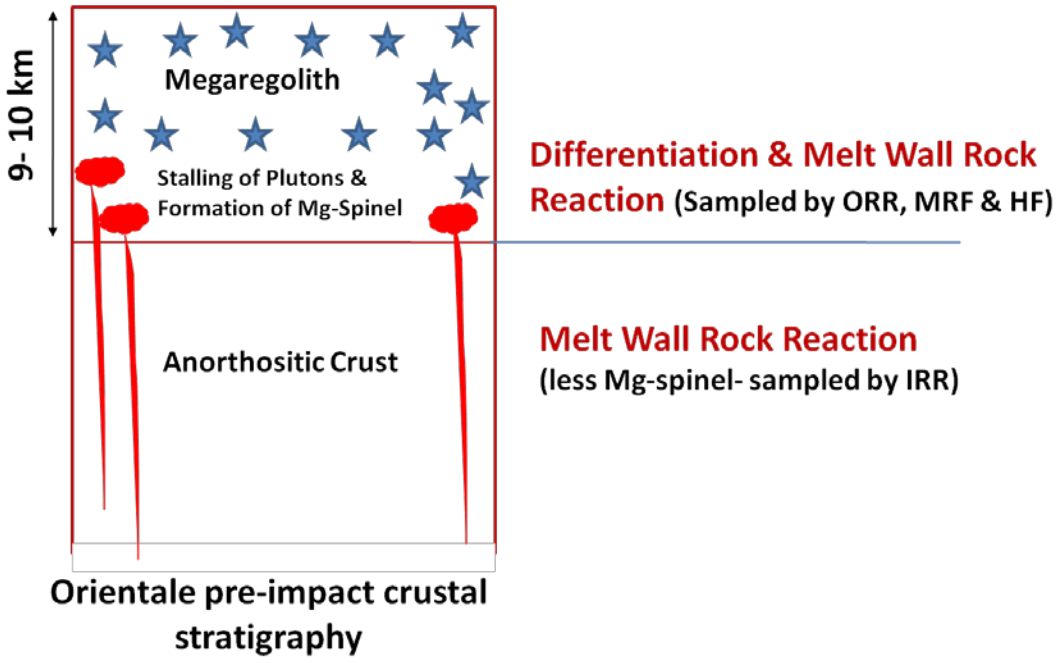

Figure 8.2 A schematic depicting a plausible scenario for the formation and distribution of Mg-spinel exposures in the Orientale basin.

8.4 Geological evolution of the Lowell crater region

The Lowell crater has formed inside Orientale basin just outside (or intersecting) the popularly accepted limit of the Orientale transient cavity. Therefore, Lowell crater is expected to excavate ~3 km thick Orientale basin ejecta (Fassett et al., 2011) composed of anorthosites, anorthositic norites and norites (Spudis et al., 1984), and also possibly some Mg-spinel bearing lithologies**.** Spectral signatures of these rock-types have been pre-dominantly noticed in the walls of the Lowell crater and in the ejecta; therefore, they could be composed of ejecta of the Orientale basin. In contrast, the central peak, floor irregularities, melt pools, and parts of the ejecta blanket (in the immediate viscinity of the Lowell crater on the northwestern and northeastern side) show largely gabbroic/basaltic composition. There could be three possibilities for the origin of these basaltic/gabbroic rocks exposed in the Lowell crater. These are as follows:

- magmatic intrusion/extrusion during ancient volcanism, prior to the LHB

- a deep seated pluton that stalled in the thick megaregolith (already present in the area) before the formation of the Orientale basin
- a post-Orientale magmatic intrusion (and also possibly some extrusions contemporaneous to the basalts of Lacus Veris)

Among these, the possibility for the basaltic/gabbroic rock exposures of the Lowell crater being derived from ancient volcanism is least since the Lowell crater could not have excavated more than ~6.6 km. Here the possibility of stratigraphic uplift has not been considered due to uncertainties in the understanding of the formation of multi-ring basins (Melosh and Ivanov, 1999). The other two scenarios are quite possible.

Based on the discussion above, the morphological analysis and crater count analysis, sequence of major events that would have led to the formation of the present day Lowell crater region can be depicted into seven stages. These are as follows from older to younger sequence:

Stage 1: Formation of ~34-43 km thick largely anorthositic crust (Wieczorek et al., 2013), ~4.4 Ga ago and the formation of the global lunar grid (e.g. Fielder, 1961; Strom, 1964; Casella, 1976), possibly responsible for some of the lineaments observed in the Lowell crater region.

Stage 2: Ancient magmatism and formation and accumulation of ~10 km thick megaregolith in the region ~4.3 - 3.9 Ga (e.g. Jolliff et al., 2000; Jaumann et al., 2012)

Stage 3: Orientale impact event ~3.8 Ga, resulting in the formation of various older units of the study area such as parts of Cordillera Ring (CR), Maunder Formation (MF), massifs of Outer Rook Ring (ORR) and Inner Rook Ring (IRR), and the ejecta facie between Cordillera and the ORR, the Montes Rook Formation (MRF) (Fig 5.1)**.** Further, the Orientale impact event would have resulted in structural and stratigraphic disturbances in the region. Some of the lineaments observed in the region, especially those radial to the Orientale basin could be related to the formation of Orientale basin.

Stage 4: Late stage basaltic volcanism along the ORR ~2.5 – 1.5 Ga ago, resulting in the formation of Lacus Veris unit present in the southwest corner of the study region (Cho, 2012; Whitten et al., 2011; Varatharajan, 2014).

Stage 5: Lowell impact event occurred from the S-SW direction ~374 Ma ago at an angle of ~30^{o} – 45^{o}; excavating parts of Orientale ejecta and the mega-regolith layer containing a stalled pre/post Orientale pluton. Since Lowell crater formed along the ORR, it is quite possible that it would have impacted and shattered a pre-existing Lacus Veris basalt unit at its target site.

Stage 6: Formation of small (~9-15 km diameter) post Lowell prominent rayed craters - Crater S on the eastern side rim of the Lowell crater and Crater A on the CR (Fig 5.1). Crater S could be older than ~10 Ma and show impact melts emanating and diverging from its topographically lower eastern side of rim.

Stage 7: A fresh resurfaced unit with fresh viscous superposed flows of basaltic/gabbroic composition formed ~2-10 Ma ago. The unit is confined to a possible graben and shows three possible volcanic source regions. Therefore, the unit might be volcanic (?) in origin.

8.5 Concluding remarks

Geological investigations of the Lowell crater region (a ~198x198 km^2 area in the northwestern quadrant of Orientale basin) have revealed morphological and spectral diversity of the region and age of selected units in the area. The observations and analyses have been used to assess a) pre - Lowell impact conditions such as target column characteristics; b) the nature and time of Lowell impact event; and, c) the geological modifications of the region thereafter. Finally, these inferences have been synthesized with general geology of Orientale basin (the host mega structure) and the Moon to derive evolutionary stages of the Lowell crater region. Some of the noteworthy findings from the study presented in this thesis are summarized as follows:

- The Lowell crater is polygonal in shape with rim-rim diameter of ~67.8 km (derived from topographic cross-sections in the WE, NW-SE and SE-NW

directions). It is ~3 km deep and shows a distinct central peak, which is ~1.5 km high. The appearance of the Lowell crater is an integrated effect of the pre-impact topography of the region, pre-existing structural and impact features, target composition, the impact characteristics, formation of a prominent superposed asymmetric rayed crater (~9 km in diameter) and a possible volcanic eruption during recent times (?).

- The crater formed due to an oblique impact (~30^{o} -45^{o}) in the Montes Rook from the S-SW direction ~374 Ma ago, as indicated by the pronounced asymmetry in the ejecta distribution, the rim-wall morphology and topography, and crater density in selected parts of the proximal ejecta blanket. A total of 3711 craters in the size range 30 – 600 m have been counted in ~1479 km^2 area of the proximal ejecta to derive the CSFD.

- MNF based spectral reflectance studies have been found to be useful in capturing most of the spectral diversity of the region using M^3 data. The Lowell crater region shows presence of gabbroic/basaltic rocks, noritic rocks, various varieties of anorthosites (shocked, un-shocked and Mg-spinel bearing), pyroclastics and, possibly Mg-spinel bearing troctolites.

- The ejecta in the immediate proximity of the Lowell crater, impact melts and western part of the central peak largely shows gabbroic/basaltic composition. In contrast, the Lowell crater wall is mostly noritic – anorthositic norite and at places Mg-spinel bearing. Further, eastern part of the central peak shows dominantly Mg-spinel anorthosites with intermittent un-shocked plagioclase, and possible exposures of low Ca pyroxene dominated rocks. The boulder lined areas on the central peak show strong curved inflexion ~1.25, which could be due to presence of olivine (as one of the possibilities) in them along with pyroxene and/or Mg-spinel.

- These lithological assemblages of the components of the Lowell crater indicate that the Lowell crater would have excavated a deep-seated pre-existing (pre/ post Orientale) mafic pluton. It is possible that the sampled pluton was emplaced in the megareolith layer beneath thick layer of Orientale ejecta in the Montes Rook

region. There are indications that this magmatic intrusion could be Mg rich however further studies (especially concerning the composition and origin of the boulders on the central peak) would be required to discern the exact nature of the pluton.

- A uniquely carved basaltic/gabbroic resurfacing (~2-10 Ma old) occur inside the Lowell crater. The resurfacing shows multiple generations of fresh viscous flows confined to a possible graben and some potential source regions. There are indications that these could be volcanic in origin (?). However, in this case there is a direct association with Crater S – an impact crater; therefore impact melt scenario cannot be completely ruled out for their formation. Further investigations involving additional datasets such as hyperspectral data with higher spatial resolution, NAC DTM, and geochemical data with commensurate spatial resolution coupled with adequate thermal modeling would be required to resolve this issue and reach further understanding in this regard.

Thus, the study has showcased Lowell crater region as an important site to understand impact cratering and magmatism. The findings have demonstrated scope of the high resolution data available from state-of-the art payloads aboard recent remote sensing missions to the Moon such as Chandrayaan-1, Kaguya and LRO.

References

Adams, J. B., 1974. Visible and near-infrared diffuse reflectance spectra of pyroxenes as applied to remote sensing of solid objects in the solar system. *Journal of Geophysical Research*, 79, 4829–4836.

Adams, J. B., et al., 1981. Remote sensing of basalts in the solar system. In: *Basaltic Volcanism on the Terrestrial Planets*, Pergamon, New York, pp. 438–490.

Adams, J. B., Goullaud, L. H., 1978. Plagioclase feldspars: visible and near infrared diffuse reflectance spectra as applied to remote sensing. In: *Proceedings of 9th Lunar and Planetary Science Conference*, 2901-2909.

Adams, J. B., Hörz, F., Gibbons, R. V., 1979. Effects of shock loading on the reflectance spectra of plagioclase, pyroxene, and glass. In: *Proceedings of* 10th *Lunar and Planetary Science Conference*, Abstract #1001.

Arya, A. S, et al., 2012. Lunar surface age determination using Chandrayaan-1 TMC data. *Current Science*, 102, 5, 783.

Ashley, J. W., Robinson, M. S., Hawke, B. R., van der Bogert, C. H., 2012. Geology of the King crater region: New insights into impact melt dynamics on the Moon. *Journal of Geophysical Research*, 117, E00H29, 13PP, doi: 10.1029/2011JE003990.

Basilevsky, A. T., 1993. Age of rifting and associated volcanism in Alta Region, Venus. *Geophysical Research Letters*, 20, 10, 883-886.

Basilevsky, A. T., 1994. Factors controlling volcanism and tectonism in solar system solid bodies. *Earth, Moon, and Planets*, 67, 1-3, 47-49.

Basilevsky, A. T., Head, J. W., 1995. Geologic exploration of the Lunar Maria: Present problems and Lunokhod experience, EGS Meeting.

Bell, J. F., Hawke, B. R., 1984. Lunar dark-haloed impact craters: Origin and implications for early mare volcanism. *Journal of Geophysical Research*, 89, 1899-1910.

Bell, P. M., Mao, H. K., 1973. Optical and chemical analysis of iron in Luna 20 plagioclase. *Geochimica et Cosmochimica Acta*, 37, 755–759.

Belton, M. J. S., et al., 1992. Lunar impact basins and crustal heterogeneity: New western limb and far Side data from Galileo. *Science*, 255, 570-576.

Besse, S., et al., 2013. One moon, many measurements 2: Photometric corrections, *Icarus*, 226, 127-139, doi: 10.1016/j.icarus.2013.05.009.

Besse, S., Sunshine, J.M., Gaddis, L.R., 2014. Volcanic glass signatures in spectroscopic survey of newly proposed lunar pyroclastic deposits. *Journal of Geophysical Research: Planets*, 119, 355–372, doi:10.1002/2013JE004537.

Bhandari, N., Adimurthy, V., Banerjee, D., Srivastava, N., Dhingra, D., 2004. Chandrayaan-1 Lunar Polar Orbiter: *Science* goals and Payloads. In: *Proceedingsof International Lunar Conference 2003/ ILEWG 5*, Hawaii, American Astronautical Society, 33-42.

Bhattacharya, S., Chauhan, P., Ajai, 2012. Discovery of orthopyroxene–olivine–spinel assemblage from the lunar nearside using Chandrayaan-1 Moon Mineralogy Mapper data. *Current Science*, 103, 1, 21 – 23.

Bhattacharya, S., et al., 2013. Endogenic water on the Moon associated with non-mare silicic volcanism: implications for hydrated lunar interior. *Current Science*, 105, 5, 685 – 691.

Binder, A. B., 1982. Post imbrium global tectonism: Evidence for an initially totally molten Moon. *Moon and Planets*, 26, 117.

Binder, A. B., 1998. Lunar Prospector: Overview. *Science*, 281, No. 5382, 1475-1476.

Boardman, J. W., et al., 2011. Measuring moonlight: An overview of the spatial properties, lunar coverage, selenolocation, and related Level 1B products of the Moon Mineralogy Mapper. *Journal of Geophysical Research*, 116, E00G14.

Boardman, J. W., Kruse, F. A., 1994. Automated spectral analysis:a geological example using AVIRIS data, north Grapevine Mountains, Nevada: in *Proceedings, ERIM Tenth Thematic Conference on Geologic Remote Sensing*, Environmental Research Institute of Michigan, Ann Arbor, MI, I-407- I-418.

Bray, V. J., et al., 2010. New insight into lunar impact melt mobility from the LRO camera. *Geophysical Research Letters*, 37, L21202, doi:10.1029/2010GL044666.

Bruckenthal, E. A., Pieters, C. M., 1984. Spectral effects of natural shock on plagioclase feldspar. In: *Proceedings of 15th Lunar and Planetary Science Conference*, pp. 96-97.

Burns, R. G., 1993. *Mineralogical Applications of Crystal Field Theory, 2nd ed*., Cambridge University Press, New York, doi:10.1017/ CBO9780511524899.

Bussey, D.B.J., Spudis, P., 1997. Compositional Analysis of the Orientale Basin using full resolution Clementine data: Some Preliminary Results. *Geophysical Research Letters*, 24, 4, 445-448.

Bussey, D. B. J., Spudis, P., 2000. Compositional Studies of the Orientale, Humorum, Nectaris and Crisium lunar basins. *Journal of Geophysical Research*, 105, E2, 4235 – 4243.

Cameron, A. G. W., Ward, W. R., 1976. The origin of the Moon. *Lunar Science*, 7, 120-122.

Casella, C. J., 1976. Evolution of the lunar fracture network. *Geological Society of America Bulletin*, 87, 2, 226-234, doi: 10.1130/0016-7606.

Chandra, U., Parthasarathy, G., 2009. Magnitude of Precambrian impact experienced by native iron sample through high-pressure Mössbauer spectroscopy. *Geochimica et Cosmochimica Acta*, 73, A208.

Chauhan, P., et al., 2011. Studies of lunar dark halo craters in northwestern mare Nectaris using high resolution Chandrayaan-1 data. In: *Proceedings of 42nd Lunar and Planetary Science Conference*, Abstract# 1338.

Chauhan, P., et al., 2012. Compositional and Morphological analysis of high resolution remote sensing data over central peak of Tycho crater on the Moon: Implications for understanding lunar interior. *Current Science*, 102, 7, 1041- 1046.

Cheek, L.C., Donaldson Hanna, K.L., Pieters, C.M., Head, J.W., Whitten, J.L., 2013. The distribution and purity of anorthosite across the Orientale basin: new perspectives from moon mineralogy mapper data. *Journal of Geophysical Research*, doi: 10.1002/jgre.20126.

Cheek, L.C., et al., 2011. Goldschmidt crater and the Moon's north polar region: Results from the Moon Mineralogy Mapper (M3). *Journal of Geophysical Research*, 116, E00G02.

Cho, Y., et al., 2012. Young mare volcanism in the Orientale region contemporary with the Procellarum KREEP Terrane (PKT) volcanism peak period 2 b. y. ago. *Geophysical Research. Letters*, 39, L11203.

Clark, R. N., 1999. Chapter 1: Spectroscopy of Rocks and Minerals and Principles of Spectroscopy. In: Rencz, A. N. (Ed.), *Manual of Remote Sensing*, John Wiley and Sons, New York, pp. 3-58.

Clark, R.N., King, T.V.V., Gorelick, N.S., 1987. Automatic Continuum Analysis of Reflectance Spectra. *Proceedings of the Third Airborne Imaging Spectrometer Data Analysis Workshop*, JPL Publication 87-30, 138-14.

Clark, R. N., Pieters, C. M., Green, R. O., Boardman, J. W., Petro, N. E., 2011. Thermal removal from near-infrared imaging spectroscopy data of the Moon. *Journal of Geophysical Research*, 16, E00G16.

Clark, R. N., Roush, T. L., 1984. Reflectance spectroscopy: Quantitative analysis techniques for remote sensing applications. *Journal of Geophysical Research*, 89, B7, 6329-6340

Cloutis, E. A., Gaffey, M. J., 1991. Pyroxene spectroscopy revisited: Spectral-compositional correlations and relationship to geo-thermometry. *Journal of Geophysical Research*, 96, 22, 809–22,826.

Colaprete, A., et al., 2010. Detection of water in LCROSS ejecta plume. *Science* 22, 330, 6003, 463-468.

Croft, S.K., 1985. The scaling of complex craters. *Journal of Geophysical Research*,90, C828-C842.

Crotts, A., 2008. Lunar outgassing, transient phenomena and the return to the Moon, I: Existing data. *The Astrophysical Journal*, 687: 692-705.

Crotts, A., 2012. Water on the Moon, III, Volatiles & activity. *Astronomical Review*, 7, 53-94.

Crotts, A., et al., 2007. Probing lunar volatiles: Initial ground-based results. In: *Proceedings of 38th Lunar and Planet Science Conference*, Abstract# 2294.

Denevi, B. W., et al., 2012. Physical constraints on impact melt properties from Lunar Reconnaissance Orbiter Camera images. *Icarus*, 219, 665-675.

Denevi, B. W., Lucey, P. G., Hochberg, E. J., Steutel, D., 2007. Near- infrared optical constants of pyroxene as a function of iron and calcium content. *Journal of Geophysical Research*, 112, E05009, doi:10.1029/2006JE002802.

Deutsch, A., Stöffler, D., 1987. Rb-Sr analyses of Apollo 16 melt rocks and a new age estimate for the Imbrium basin: Lunar basin chronology and the early heavy bombardment of the Moon. *Geochimica et Cosmochimica Acta*, 51, 1951-1964.

Dhingra, D., et al., 2011.. Compositional diversity at Theophilus Crater: Understanding the geological context of Mg-spinel bearing central peaks. *Geophysical Research Letters*, 38, L11201, doi: 10.1029/2011G L047314.

Dhingra, D., Pieters, C.M., 2011. Mg-spinel rich lithology at crater Copernicus. *Annual Meeting of the Lunar Exploration Analysis Group*, Abstract # 2024.

Donaldson Hanna, K. L., et al., 2011. Thermal infrared emissivity measurements under a simulated lunar environment: Application to the Diviner Lunar Radiometer Experiment, *Journal of Geophysical Research*, doi:10.1029/2011JE003862.

El-Baz, F., 1970. Lunar igneous intrusions. *Science*, 167, 49-50.

Elkins-Tanton, L.T., Burgess, S., Yin, Q.-Z., 2011. The lunar magma ocean: Reconciling the solidification process with lunar petrology and geochronology. *Earth and Planetary Science Letters*, 304, 326-336.

Fassett, C.I., Head, J.W., Smith, D.E., Zuber, M.T., Neumann, G.A., 2011. Thickness of proximal ejecta from the Orientale basin from Lunar Orbiter Laser Altimeter (LOLA) data:Implications for multi-ring basin formation. *Geophysical Research Letters*, 38, L17201, http://dx.doi.org/10.1029/2011GL048502.

Feldman, W.C. et al., 1998. Fluxes of Fast and Epithermal Neutrons from Lunar Prospector: Evidence for Water Ice at the Lunar Poles. *Science* 281, 5382, 1496-1500.

Fielder, G., 1961. Structure of the Moon's surface, Pergamon Press, New York, pp. 266.

Gaddis, L., Pieters, C. M. and Hawke, B.R., 1985. Remote Sensing of Lunar Pyroclastic Mantling Deposits. *Icarus*, 61, 461-489.

Gaffey, M. J., Cloutis E. A., Kelley M. S., Reed K. L., 2002. Mineralogy of asteroids. In: *Asteroids III*, The University of Arizona Press, Tuskon, pp. 183–204.

Gary, W. B. et al., 2012. The origin of Ina: Evidence for inflated lava flows on the Moon. *Journal of Geophysical Research*, 117, E00H31, doi:10.1029/2011JE0039

Gillis, J. J., Jolliff, B. L., Korotev, R. L., 2004. Lunar surface geochemistry: Global concentrations of Th, K, and FeO as derived from Lunar Prospector and Clementine data. *Geochimica et Cosmochimica Acta*, 68, 3791-3805.

Glotch, T.D. et al., 2011. The Mairan domes: Silicic volcanic constructs on the Moon. *Geophysical Research Letters*, 38, 8, L21204, doi:10.1029/2011GL049548.

Goswami, J. N., 1998. Short-lived nuclides in the early solar system. In: *Proceedings of the Indian Academy of Sciences - Earth and Planetary Sciences*, 107, 4, 401-411.

Goswami, J. N., Annadurai, M., 2009. Chandrayaan-1: India's first planetary Science mission to the Moon. *Current Science*, 96(4), 486–491.

Greeley, R., et al., 1993. Galileo imaging observations of lunar maria and related deposits. *Journal of Geophysical Research*, 98, 17183-17205.

Green, A. A., Berman, M., Switzer, P., Craig, M. D., 1988. A transformation for ordering multispectral data in terms of image quality with implications for noise removal: *IEEE Transactions on Geoscience and Remote Sensing*, 26, 1, 65-74.

Green, R. O., et al., 2011. The Moon Mineralogy Mapper (M3) imaging spectrometer for lunar science: Instrumentation, calibration, and on-orbit measurement performance. *Journal of Geophysical Research*, 116, E00G19.

Grieve, R. A. F., 2005. Economic natural resource deposits at terrestrial impact structures. In: McDonald, I., Boyce, A.J., Butler, I.B., Herrington, R.J., Polya, D.A. (Eds.), *Mineral Deposits and Earth Evolution*, Geological Society, London, Special Publications, 248, pp. 1–29.

Gupta, G., Sahijpal, S., 2010. Differentiation of Vesta and the parent bodies of other achondrites. *Journal of Geophysical Research,* 115, E08001, pp. 15.

Gupta, R. P. 2003. Remote Sensing Geology, Springer, Hiedelberg, Germany.

Gupta, R. P., Tiwari, R. K., Saini, V., Srivastava. N, 2013. A simplified approach for interpreting Principle Component Images. *Advances in Remote Sensing*, 2, 111 – 119.

Hapke, B., 2001. Space weathering from Mercury to the asteroid belt. *Journal of Geophysical Res*earch, 106, 10039-10073, doi:10.1029/2000JE001338.

Hapke, B., Wells, E., 1981. Bidirectional reflectance spectroscopy: 2. Experiments and observations. *Journal of Geophysical Research*, 86, B4, 3055–3060**.**

Hartmann W. K., 1999. Moons and Planets. *4TH EDS Wadsworth Publishing Company.*

Hartmann,W. K., 2003. Megaregolith evolution and cratering cataclysm models – Lunar cataclysm as a misconception (28 years later). *Meteoritics and Planetary Science,* 38, 579-593.

Hartmann, W. K., Davis, D. R., 1975. Satellite-sized planetesimals and lunar origin. *Icarus*, 24, 504–514.

Hartmann, W. K., et al., 1981. Chronology of planetary volcanism by comparative studies of planetary craters. *In*: *Basaltic Volcanism on the Terrestrial Planets*. Pergamon Press, pp. 1049-1128.

Hartmann, W. K., Kuiper, G. P., 1962. Concentric structures surrounding lunar basins. *Communications of the Lunar and Planetary Laboratory*, 12, 1, 51-66.

Hartmann, W. K., Neukum, G., 2001. Cratering chronology and the evolution of Mars. *Space Science Reviews,* 96, 165 – 194, doi:10.1023/A:1011945222010.

Hartmann, W. K., Phillips, R. J., Taylor, G. J., 1986. The Origin of the Moon. Lunar and Planetary Institute, Houston.

Hartmann, W. K., Ryder, G., Dones, L., Grinspoon, D.H., 2000. The time-dependent intense bombardment of the primordial Earth-Moon system. *In*: Righter, R. M, Canup, R. (Eds.), *Origin of the Earth and Moon*. University of Arizona Press, pp. 493-512.

Haruyama, J., et al., 2008. Global lunar-surface mapping experiment using the LunarImager/ Spectrometer on SELENE. *Earth Planets Space*, 60, 243–255.

Haruyama, J, et al., 2009. Long-lived volcanism on the lunar farside revealed by SELENE Terrain Camera. *Science*, 323, 905-908.

Haruyama, J., et al., 2012. Lunar global digital terrain model dataset produced from SELENE (KAGUYA) Terrain camera stereo observations. In: *Proceedings of 43rd Lunar and Planet Science Conference*,1200.pdf

Hawke, B. R., et al., 1991. Remote sensing studies of the Orientale region of the Moon: A pre-Galileo view. *Geophysical Research Letters*, 18, 11, 2141-2144.

Hawke, B. R., Head, J. W., 1977. Impact melt on lunar crater rims. In: Roddy, D. J., Pepin, R. O., Merrill, R. B. (Eds.), *Impact and Explosion Cratering*, Pergamon, NY, pp.815–841.

Head, J. W., 1974. Orientale multi-ringed basin interior and implications for the petrogenesis of lunar highland samples. *The Moon*, 11, 327–356.

Head, J. W., 1976. Lunar volcanism in space and time. *Reviews of Geophysics and Space Physics*, 14, 265-300.

Head, J. W., et al., 1993. Lunar impact basins: New data for the western limb and far side (Orientale and South Pole-Aitken basins) from the first Galileo flyby. *Journal of Geophysical Research*, 98, 17149-17181.

Head, J. W., Wilson, L., 1992. Lunar Mare Volcanism: Stratigraphy, eruption conditions, and the evolution of secondary crusts. *Geochimica et Cosmochimica Acta*, 56, 2155 – 2175.

Head, J. W., Wilson, L., and Weitz, C.M., 2002. Dark ring in southwestern Orientale Basin: Origin as a single pyroclastic eruption. *Journal of Geophysical Research: Planets*, 107, E1, 1.1-1.17, doi: 10.1029/2000JE001438.

Heather, D. J., Dunkin, S. K., 2003. Geology and Stratigraphy of King crater, lunar far-side. *Icarus*, 163, 307-329.

Heiken, G., Vaniman, D., French, B. M., 1991. Lunar Sourcebook: A User's Guide to the Moon. Cambridge University Press, New York.

Hiesinger, H., Head III, J.W., 2006. New views of Lunar geoscience: An introduction and overview. *Reviews in Mineralogy and Geochemistry,* 60, 1–81.

Hiesinger, H., Head III, J. W., Wolf, U., Jaumann, R., Neukum, G., 2003. Ages and stratigraphy of mare basalts in Oceanus Procellarum, Mare Nubium, Mare Cognitum, and Mare Insularum. *Journal of Geophysical Research,* 108, 5065.

Hodges, R. R., Hoffman (Jr.), J. H., Johnsonand, F. S., Evans, D. E., 1973. Composition and dynamics of lunar atmosphere. In: *Proceedings of 4th Lunar and Planetary Science Conference*, pp. 374.

Howard, K. A., Wilshire, H. G., 1975. Flows of impact melt at lunar craters. *Journal of Research of the U. S. Geological Survey,* 3, 237–251.

Ivanov, B. A., 2001. Mars/moon cratering rate ratio estimates. *In:* Kallenbach, R., Geiss, J., Hartmann, W. K. (Eds.), *Chronology and Evolution of Mars*. Kluwer Dordrecht, pp. 87-104.

Ivanov, B. A., Neukum, G., Bottke, W., Hartmann, W. K., 2002. The comparison of size-frequency distributions of impact craters and asteroids and the planetary cratering rate. *In*: Bottke, W., Cellino, A., Paolicchi, P., Binzel, R. P. (Eds.), *Asteroids III*. University Arizona Press, pp. 89-101.

Ivanov, B. A., Neukum, G., Wagner, R., 1999. Impact craters NEA and Main Belt asteroids Size-frequency distribution. In: *Proceedings of 30th Lunar and Planetary Science Conference, Abstract#* 1583.

Jaumann, R., et al., 2012. Geology, geochemistry, and geophysics of the Moon: Status of current understanding. *Planetary and Space Science*, 74, 15-41.

Jeffery, P. M., Reynolds, J. H., 1961. Origin of excess Xe129 in stone meteorites. *Journal of Geophysical Research,* 66, 3582–3583.

Jessberger, E. K., Kirsten, T., Staudacher, T., 1977. One rock and many ages - further data on consortium breccia 73215. In: *Proceedings of Lunar and Planetary Science Conference*, 8, 2567-2580.

Jolliff, B. L., et al., 2011. Non-mare silicic volcanism on the lunar far side at Compton Belkovich. *Nature GeoScience*, doi: 10.1038/NGEO1212.

Jolliff, B. L., Gillis, J. J., Haskin, L. A., Korotev, R. L., Wieczorek, M. A., 2000. Major lunar crustal terranes: Surface expressions and crust‐mantle origins. *Journal of Geophysical Research*, 105, E2, 4197–4216.

Kato, M., et al., 2010. The Kaguya mission overview. *Space Science Reviews*, 154, 3-19.

Kaur, P, Bhattacharya, S., Chauhan, P., Ajai, Kiran Kumar A.S., 2013. Mineralogy of Mare Serenitatis on the near side of the Moon based on Chandrayaan-1 Moon Mineralogy Mapper (M3) observations. *Icarus* 222, 137–148.

Kaur, P., Chauhan, P., Bhattacharya, S., Ajai and Kiran Kumar, A.S., 2012. Compositional diversity at Tycho crater: Mg-spinel exposures detected from moon mineralogical mapper (M3) data. In: *Proceedings of 43rd Lunar & Planetary Science Conference*, 1434.

Klima, R. L., Cahill, J., Hagerty, J., Lawrence, D., 2013. Remote detection of magmatic water in Bullialdus Crater on the Moon. *Nature Geoscience*, 6, 737-741, doi:10.1038/ngeo1909

Klima, R. L., Dyar, M. D., Pieters, C. M., 2011. Near-infrared spectra of clinopyroxenes: Effects of calcium content and crystal structure. *Meteoritics and Planetary Science*, 46, 379–395.

Klima, R. L., Pieters, C. M., Dyar, M. D., 2007. Spectroscopy of synthetic Mg-Fe pyroxenes I: Spin-allowed and spin-forbidden crystal field bands in the visible and near-infrared. *Meteoritics and Planetary Science*, 42, 235-253.

Kneissl, T., van Gasselt, S., Neukum, G., 2011. Map-projection-independent crater size-frequency determination in GIS environments — New software tool for ArcGIS. *Planetary and Space Science*, 59, 11–12, 1243–1254.

Koeberl, C., 2006. Impact processes on the early Earth. *Elements*, 2, 211-216.

Krüger, T., van der Bogert C. H., Hiesinger, H., 2013. New high-resolution melt distribution map and topograpic analysis of tycho crater. In: *Proceedings of 44th Lunar and Planetary Science Conference*, Abstract #2152.

Kumar, P. S., et al., 2011. Chandrayaan-1 observation of distant secondary craters of Copernicus exhibiting central mound morphology: Evidence for low velocity clustered impacts on the Moon. *Planetary and Space Science*, 59, 9, 870 - 879.

Lal, D., et al., 2012. Detection of Mg spinel lithologies on central peak of crater Theophilus using Moon Mineralogy Mapper (M^3) data from Chandrayaan-1. *Journal of Earth System Science*, 121, 3, 847-853.

Lawrence, D. J., et al., 1998. Global Elemental Maps of the Moon: The Lunar Prospector Gamma-Ray Spectrometer. *Science*, 281, 5382, 1484–1489.

Levinson, A. A., Taylor, S. R., 1971. Moon rocks and minerals; scientific results of the study of the Apollo 11 lunar samples with preliminary data on Apollo 12 samples. New York: Pergamon Press.

Li, S., Milliken, R. E., 2013. Quantitative mapping of lunar surface hydration with Moon Mineralogy Mapper (M3) data. In: *Proceedings of* 44th *Lunar & Planetary Science Conference*, Abstract #1337.

Lodders, K. and Fegley, B. Jr., 1998. The planetary scientists companion Publication Oxford university press.

Lucey, P. G., 2004. Mineral maps of the Moon. 31, L08701, doi:10.1029/2003GL019406.

Lucey, P. G., Blewett, D. T., Hawke., B. R., 1998. Mapping the FeO and TiO_2 content of the lunar surface with multispectral imagery. *Journal of Geophysical Research*, 103 (E2), 3679–3699.

Lucey, P.G., Blewett, D.T., Jolliff, B.L., 2000. Lunar iron and titanium abundance algorithms based on final processing of Clementine ultraviolet–visible images. *Journal of Geophysical Research*, 106, E8, 20297–20305.

Lynden-Bell, D., Pringle, J. E., 1974. The evolution of viscous discs and the origin of the nebular variables. Monthly Notices of the Royal Astronomical Society (MNRAS), 168, 603 – 637

McCord, T. B., et al.,1981. Moon: Near-infrared spectral reflectance, a first good look. *Journal of Geophysical Research*, 86, 10, 883-10,892.

McEwen, A. S., Bierhaus, E. B., 2006. The importance of secondary cratering to age constraints on planetary surfaces. *Annual Review of Earth and Planetary Sciences*, 34, 535 – 567, doi:10.1146/annurev.earth.34.031405.125018.

McEwen, A. S., et al., 1993. Galileo observations of post Imbrium lunar craters during the first earth-moon flyby. *Journal of Geophysical Research*, 98, E9, 17, 207 - 17,231.

Melosh, H. J., 1989. Impact Cratering: A Geologic Process, Oxford Univ. Press, pp. 245.

Melosh, H. J., 2011. Planetary surface processes, Cambridge university press.

Melosh, H. J., et al., 2013. The Origin of Lunar Mascon Basins. *Science*, 340, 1552-1555. doi: 10.1126/science.1235768

Melosh H. J., Ivanov, B.A., 1999. Impact crater collapse. *Annual Review of Earth and Planetary Sciences*, 27, 385-415.

Melosh, H. J., Mckinnon, W. K., 1978. The mechanics of ringed basin formation. *Geophysical Research Letters*, 5, 985 – 988.

Menzel, D. H., Minnaert, M., Levin, B., Dollfus, A., Bell, B., 1971. Report on lunar nomenclature by the working group of commission 17 of the IAU. *Space Science Reviews*, 12, 2, 136-186.

Michael, G., Neukum, G., 2008. Surface dating: software tool for analysing crater size-frequency distributions including those showing partial resurfacing events. In: *Proceedings of Lunar and Planetary Institute Science Conference*, 39, 1780.

Michael, G., Neukum, G., 2010. Planetary surface dating from crater size–frequency distribution measurements: Partial resurfacing events and statistical age uncertainty. *Earth and Planetary Science Letters*, 294, 3–4, 223-229, http://dx.doi.org/10.1016/j.epsl.2009.12.041.

Montmerle, T., Augereau, J. C., Chaussidon, M., 2006. Solar System Formation and Early Evolution: the First 100 Million Years. *Earth, Moon, and Planets*, 98, 1–4, 39–95.

Morbidelli, A., Petit, J. M., Gladman, B., Chambers, J., 2001. A plausible cause of the late heavy bombardment. *Meteoritics & Planetary Science*, 36, 371–380.

Moriarty III, D. P., Pieters, C. M., Isaacson, P. J., 2013. Compositional heterogeneity of central peaks within the South Pole-Aitken Basin. *Journal of Geophysical Research*, 118, 2310-2322, doi: 10.1002/2013JE004376.

Morgan, J.V., et al., 1997. Size and morphology of the Chicxulub impact crater. *Nature*, 390, 472 - 476.

Murty, S. V. S., Goswami, J. N., Shukolyukov, Y. A., 1997. Excess Ar-36 in the Efremovka meteorite: a strong hint for the presence of Cl-36 in the early solar system. *The Astrophysical Journal*, 475, L65–L68.

Mustard, J.F., et al., 2011. Compositional diversity and geologic insights of the Aristarchus crater from Moon Mineralogy Mapper data. *Journal of Geophysical Research*, 116, E00G12, doi:10.1029/2010JE003726.

Mustard, J.F., Pieters, C.M., 1989. Photometric phase functions of common geologic minerals and applications to quantitative analysis of mineral mixture reflectance spectra. *Journal of Geophysical Research,* 94, 13619-13634.

Nakamura, Y., et al., 1974. Deep lunar interior inferred from recent seismic data. *Geophysical Research Letters*, 1, 137–140.

Neukum, G., 1983. Meteoritenbombardement und Datierung planetarer Oberflächen. *Habilitation Dissertation for Faculty Membership Ludwig-Maximilians-University Munich,* 186.

Neukum, G., Ivanov, B. A., 1994. Crater size distribution and impact probabilities on Earth from lunar terrestrial-planet and asteroid cratering data. In: Gehrels, T. (Ed.), *Hazards Due to Comets and Asteroids,* University of Arizona Press, pp. 359-41.

Neukum, G., Ivanov, B., Hartmann, W. K., 2001. Cratering records in the inner solar system. In: Kallenbach, R., Geiss, J., Hartmann, W. K. (Eds), *Chronology and Evolution of Mars*, Kluwer, pp. 55-86

Neukum, G., König, B., 1976. Dating of individual lunar craters. In: *Proceedings of 7th Lunar Science Conference*, 2, 867-2,881.

Neukum, G., König, B., Arkani-Hamed, J., 1975. A study of lunar impact crater size distributions. *The Moon*, 12, 201-229.

Nordgren, T., 2010. Stars Above, Earth Below: A Guide to Astronomy in the National Parks, Springer.

Nozette, S., et al., 1994. The Clementine mission to the Moon: Scientific overview. *Science*, 266, 5192, 1835-1839.

Ohtake, M., et al., 2008. Scientific objectives and specification of the SELENE Multiband Imager. *Advances in Space Research,* 42, 301–304.

Ohtake, M., et al., 2009. The global distribution of pure anorthosite on the Moon. *Nature*, 461, 236– 240.

Osinski, G. R., Tornabene, L. L., Grieve, R. A. F., 2011. Impact ejecta emplacement on terrestrial planets. *Earth and Planetary Science Letters,* 310, 167–181.

Papike, J., Taylor, L., Simon, S., 1991. Lunar Minersls. In: Heiken, G., Vaniman, D., French, B. M. (Eds.), *Lunar Sourcebook: A User's Guide to the Moon,* Cambridge University Press, New York.

Parker, M. V. K., et al., 2012. Neutral buoyancy of titanium-rich melts in the deep lunar interior. *Nature GeoScience*, 5, 186-189, doi:10.1038/ngeo1402.

Parthasarathy, G., Bhandari, N., Vairamani, M., Kunwar, A. C., 2008. High-pressure phase of natural fullerene C60 in iridium-rich Cretaceous–Tertiary boundary layers of Deccan intertrappean deposits, Anjar, India. *Geochimica et Cosmochimica Acta*, 72, 978-987.

Pati, J. K., et al., 2010. First SHRIMP U-Pb and 40Ar /39Ar chronolgical results from impact melt breccia from the Paleopoterozoic Dhala impact structure, India. *The Geological Society of America*, Special Paper 465, 571–591, doi: 10.1130/2010.2465(27).

Pati, J. K., Reimold, W.U., 2007. Impact cratering: Fundamental process in geoscience and planetary science. *Journal of Earth System Sciences*, 116, 2, 81-98. 2007.

Pati, J. K., Reimold, W. U., Koeberl, C., Pati, P., 2008. The Dhala Structure, Bundelkhand, Central India--Eroded remnant of a large Paleoproterozoic impact structure. *Meteoritics and Planetary Science*, 43, 1383-1398.

Pierazzo, E., Melosh, H. J., 2000. Melt production in oblique impacts. *Icarus*, 145, 252 – 261.

Pieters, C. M., 1986. Composition of the lunar highland crust from near-infrared spectroscopy. *Reviews of Geophysics*, 24, 3, 557-578.

Pieters, C. M., 1991. The probable continuum between emplacement of plutons and mare volcanism in lunar crustal evolution. *LPI Technical Report 91-03*, p. 43.

Pieters, C. M., Englert, P. A. J., 1993. Remote Geochemical Analysis: Elemental and Mineralogical Composition, Cambridge University Press.

Pieters, C. M., et al., 2009a. The Moon Mineralogy Mapper (M^3) on Chandrayaan-1. *Current Science*, 96, 500 – 505.

Pieters, C. M., et al., 2009b. Character and spatial distribution of Possible OH/H2O on the surface of the Moon seen by M3 on Chandrayaan-1. *Science*, 326, doi:10.1126/*Science*.1178658.

Pieters, C. M., et al., 2011. Mg spinel lithology: A new lunar rock type on the lunar far side. *Journal of Geophysical Research*, 116, E00G08, doi:10.1029/2010JE003727.

Pieters, C. M., Head III, J. W., Gaddis, L., Jolliff, B., Duke, M., 2001. Rock Types of South Pole Aitken Basin and extent of basaltic volcanism. *Journal of Geophysical Research*, 106, E11, 28,001 - 28,022.

Pieters, C. M., Tompkins, S., 1999. Tsiolkovsky crater: A window into crustal processes on the lunar far-side. *Journal of Geophysical Research*, 104, E9, 21,935-21,949.

Pike, R. J., 1973. Crater studies: Part A: lunar crater morphometry. *Apollo 17 preliminary science report (NASA SP-330)*, 32(1)-32(7).

Pike, R. J., 1974. Depth/diameter relations of fresh lunar craters: Revision from spacecraft data. *Geophysical Research Letters*, 1, 7, 291- 294.

Pike, R. J., 1977a. Size-dependence in the shape of fresh impact craters on the Moon. In: Roddy, D. J., Pepin, R. O., Merrill, R. B. (Eds.), *Impact and Exp-losion Cratering*. Pergamon Press, pp. 489-510.

Pike, R. J., 1977b. Apparent depth/apparent diameter relations for lunar craters. In: *Proceedings of 8th Lunar Science Conference*, 3, 427-3,436.

Pike, R. J., 1980. Geometric Interpretation of Lunar Craters. *US Geological Survey Professional Paper*, 1046-C, US Govt. Printing Office.

Pike, R. J., 1985. Some morphologic systematics of complex impact structures. *Meteoritics and Planetary Science*, 20, 49-68.

Plescia, J. B., Cintala, M. J., 2012. Impact melt in small lunar highland craters. *Journal of Geophysical Research*, 117, E00H12, doi:10.1029/2011JE003941.

Prissel, T. C., et al., 2012. Melt-wallrock reactions on the moon: Experimental constraints on the formation of newly discovered mg-spinel anorthosites. In: *Proceedings of 43rd Lunar & Planetary Science Conference*, Abstract # 2743.

Prissel, T. C., et al., 2013. An "Uncollected" Member of the Mg-Suite: Mg-Al Pink Spinel Anorthosites and their Place on the Moon. In: *Proceedings of* 44th *Lunar and Planetary Science Conference,* Abstract # 3066.

Reddy, V., et al., 2012a. Color and albedo heterogeneity of Vesta from Dawn. *Science,* 336, 700-704.

Reddy, V., Gaffey, M. J., Hardersen, P. S., 2012b. Constraining albedo, diameter and composition of near-Earth asteroid via near-IR spectroscopy. *Icarus,* 219, 382-392.

Reddy, V., et al., 2011.Compositional heterogeneity of Asteroid 4 Vesta's Southern Hemisphere: Implications for the DAWN Mission. *Icarus,* 210, 2, 693-706.

Robinson, M. S., et al., 2010. Lunar Reconnaisance Orbiter Camera (LROC) instrument overview. *Space Sciience Reviews*, 150, 81-124, doi: 10.1007/S11214-010-9634-2.

Robinson, M., Riner, M., 2005. Advances in lunar science from the Clementine mission: A decadal perspective. *Journal of Earth System Science*, 114, 6, 669-686.

Saal, A. E., et al., 2008. Volatile content of lunar volcanic glasses and the presence of water in the Moon's interior. *Nature*, 454, 192–195.

Saal, A. E., Hauri, E. H., Van Orman, J. A., Rutherford, M. J., 2013. Hydrogen Isotopes in Lunar Volcanic Glasses and Melt Inclusions Reveal a Carbonaceous Chondrite Heritage. *Science*, 340, 6138, 1317-1320.

Sasaki, S., Kurahashi, E., Yamanaka, C., Nakamura, K., 2003. Laboratory simulation of space weathering: Changes of optical properties and TEM/ESR confirmation of nanophase metallic iron. *Advances in Space Research*, 31, 12, 2537-2542(6).

Sahijpal, S., Goswami, J. N., Davis, A.M., Grossman, L., Lewis, R.S., 1998. A stellar origin for the short-lived nuclides in the early Solar System. *Nature*, 391**,** 559-561.

Sahijpal, S., Gupta G., 2009. The plausible source(s) of ^{26}Al in the early solar system: A massive star or the X-wind irradiation scenario? *Meteoritics and Planetary Science*, 44, 879-890.

Sahijpal, S., Soni, P., Gupta, G., 2007. Numerical simulations of the planetary differentiation of accreting planetesimals with ^{26}Al and ^{60}Fe as the heat sources. *Meteoritics and Planetary Science*, 42, 1529-1549.

Schultz, P.H., 1976. Moon Morphology, University of Texas Press.

Schultz, P. H., Spudis P. D., 1978. The dark ring of Orientale: implications for pre-basin mare volcanism and a clue to the identification of the transient cavity rim. In: *Proceedings of* 9th *Lunar and Planetary Science Conference*, 1033-1035.

Schultz, P. H., Staid, M. I., and Pieters, C. M. 2006. Lunar activity from recent gas release, Nature, 444, 184–186, doi:10.1038/nature05303.

Scott, D. H., McCauley, J. F., and West, M. N., 1977. Geologic map of the west side of the Moon. *U.S. Geological Survey Map*, 1-1034.

Senft, L. E., Stewart, S. T., 2007. Modeling impact cratering in layered surfaces. *Journal of Geophysical Research*, 112, E11002, doi: 10.1029/2007JE002894.

Shoemaker, E. M., 1962. Interpretation of lunar craters. In: Kopal, Z. (Ed.), *Physics and Astronomy of the Moon*, Academic San Diego, California, pp. 283-359.

Shoemaker, E. M., Hackmann, R. J., 1962. Stratigraphic basis for a lunar time scale. *In:* Kopal, Z., Mikhailov, Z. K. (Eds.), *The Moon*, Academic Press, pp. 289-300.

Singer, R. B., Roush, T. L., 1985. Effects of temperature on remotely sensed mineral absorption features. *Journal of Geophysical Research*, 90(B14), 12434-12444, doi: 10.1029/JB090iB14p12434.

Spudis, P. D., 1993. The Geology of Multi-ring Basins: The Moon and Other Planets. Cambridge University Press, New York and Cambridge, pp. 263.

Spudis, P. D., 1999. Volcanism on the Moon. In: Sigurdsson, H. (Ed.), *Encyclopedia of Volcanoes*, Academic Press, New York, pp. 697-708.

Spudis, P. D., Hawke, B. R., Lucey, P. G., 1984. Composition of Orientale Basin deposits and implications for the lunar basin-forming process. In: *Proceedings of 15th Lunar and Planetary Science Conference*, Part 1, *Journal of Geophysical Research*, 89, suppl., C197–C210.

Spudis, P. D., McGovern, P. J., Kiefer, W. S., 2013. Large shield volcanoes on the Moon. *Journal of Geophysical Research: Planets*, 118, 1–19, doi:10.1002/jgre.20059.

Spudis, P. D., Wilhelms, D. E., Robinson, M. S., 2011. The sculptured hills of the Taurus highlands: Implications for the relative age of Serenitatis, basin chronologies and the cratering history of the Moon. *Journal of Geophysical Research*, 116, E00H03, doi:10.1029/2011JE003903.

Sridharan, R., et al. 2010a. The Sunlit Lunar Atmosphere: a Comprehensive Study by CHACE on the Moon Impact Probe of Chandrayaan-1. *Planetary and Space Science*, 58, 12, 1567–1577, http://dx.doi.org/10.1016/j.pss.2010.07.027

Sridharan, R., et al., 2010b. 'Direct' evidence for water (H_2O) in the sunlit lunar ambience. *Planetary and Space Science*, 58, 947–950.

Srivastava, N., 2008. Titanium estimates of the central peaks of lunar craters: Implications for sub surface lithology of moon. *Advances in Space Research*, 42/2, 28-284.

Srivastava, N., Kumar, D., Gupta, R. P., 2011. Is the moon still active? In: *Proceedings of Conference on Planetary Sciences and Exploration*, PRL, Ahmedabad, India, pp. 97 – 98.

Srivastava, N., Kumar, D., Gupta, R. P., 2013. Young viscous flows in the Lowell crater of Orientale basin, Moon: Impact melts or volcanic eruptions? *Planetary and Space Science*, 87, 37-45.

Srivastava, N., Gupta R. P., 2012. Compositional diversity inside Lowell crater, Orientale Basin: Evidences for extensive spinel rich deposits. In: *Proceedings of 2nd Conference on Lunar Highland Crust,* Abstract # 9016.

Srivastava, N., Gupta, R. P., 2013. Spatial distribution of spinel in the Orientale Basin, new insights fro-m M3 data. In: *Proceedings of 44th Lunar & Planetary Science Conference*, Abstract *#1509.*

Staid, M. I., et al., 2011. The mineralogy of last-stage lunar volcanism as observed by the Moon mineralogy Mapper on Chandrayaan-1. *Journal of Geophysical Research,* 106, 27,877–27,900.

Stöffler, D., et al., 2006. Cratering history and lunar chronology. In: Joliff, B. L:, Wieczorek, M. A., Shearer, C. K., Neal, C. R. (Eds.), *New Views of the Moon, Reviews in Mineralogy and Geochemistry,* 60, Mineralogical Society of America and Geochemical Society, The Mineralogical Society of America, Chantilly, Virginia, USA, pp. 519-596.

Stöffler, D., Knöll, H. D., Marvin, U. B., Simonds, C. H., Warren, P. H., 1980. Recommended classification and nomenclature of lunar highland rocks—a committee report. In: *Proceedings of the Conference on the Lunar Highlands Crust* (J. J. Papike and R. B. Merrill, eds.), 51–70. Pergamon, New York.

Stöffler, D., Ryder, G., 2001. Stratigraphy and isotope ages of lunar geologic units: Chronological standard for the inner solar system. In: Kallenbach, R., Geiss, J., Hartmann, W. K., (Eds.), *Chronology and Evolution of Mars*, Kluwer, 9-54.

Strom, R. G., 1964. Analysis of lunar lineaments: I — Tectonic maps of the Moon. *Communications of Lunar and Planetary Laboratory,* Arizona University, 2, 39, 205-221.

Strom, R. G., Fielder, G., 1968. Multiphase development of Lunar crater Tycho. *Nature*, 217, 611 - 615.

Strom, R. G., Fielder, G., 1970. Multiphase eruptions associated with Tycho and Aristarchus. *Communications of Lunar & Planetary Laboratory,* 8, 235–288, Arizona University.

Sun, Y., Li, L., Zhang, Y. Z., 2013. Detection of Mg-spinel bearing central peaks using M3images. In: *Proceedings of 44th Lunar and Planetary Science Conference,* Abstract #1393.

Sunshine, J. M., et al., 2010. Hidden in Plain Sight: Spinel-Rich Deposits on the Nearside of the Moon as Revealed by Moon Mineralogy Mapper (M3). In: *Proceedings of 41st Lunar and Planetary Science Conference*, Abstract # 1508.

Sunshine, J., Pieters, C. M., 1998. Determining the composition of olivine from reflectance spectroscopy. *Journal of Geophysical Research*, 103, E6, 13,675-13,688.

Taylor, G. J., 1994. The scientific legacy of Apollo. *Scientific American*, 271, p. 40-47.

Taylor, G. J. et al., 1991, Lunar Rocks. In: Heiken, G., Vaniman, D., French, B. M. (Eds.), *Lunar Sourcebook: A User's Guide to the Moon*, Cambridge University Press, New York.

Taylor, S. K, McLennan, S. M., 2009. Planetary Crusts: Their Composition, Origin and Evolution, Cambridge University Press, Cambridge, pp. 378.

Taylor, S. R., 1975. Lunar science: a post-Apollo view; scientific results and insights from the lunar samples, New York: Pergamon Press.

Taylor, S. R., 1982. Planetary Science: A Lunar Perspective. Lunar and Planetary Institute, Houston.

Tera, F., Papanastassiou, D. A., Wasserburg, G. J., 1974, Isotopic evidence for a terminal lunar cataclysm. *Earth and Planetary Science Letters*, 22, 1-21.

Tompkins, S., Hawke, B. R., Pieters, C. M., 1999. Distribution of materials within the large crater Tycho: evidence for large gabbroic bodies in the highlands. In: *Proceedings of 30th Lunar and Planetary Science Conference*, Abstract#1573.

Tompkins, S., Pieters C. M., 1999. Mineralogy of the lunar crusts: results from Clementine. *Metoritics & Planetary Science*, 34, 1, 25 – 41.

Turner, G., Cadogan, P. H., 1975, The history of lunar bombardment inferred from 40Ar-39Ar dating of highland rocks. In: *Proceedings of the 6th Lunar Science Conference*, 1509-1538.

van der Bogert, C. H., Hiesinger, H., Krüger, T., McEwen, A. S., Dundas, C., 2013. New evidence for target property influence on crater size-frequency distributions. *44th Lunar and Planetary Science Conference*, Abstract # 1962.

Varatharajan, I., et al., 2014. Mineralogy of young lunar mare basalts: Assessment of temporal and spatial heterogeneity using M3 data from Chandrayaan-1. *Icarus*, doi: 10.1016/j.icarus.2014.03.045

Vaughan, W.M., Head, J.W., Wilson, L., Hess, P.C., 2013. Geology and petrology of enormous volumes of impact melt on the Moon: A case study of the Orientale basin impact melt sea. *Icarus*, 223, 749–765.

Warren, P. H., 1985. The magma ocean concept and lunar evolution. *Annual Reviews of Earth & Planetary Science*, 13, 201–240.

Warren, P. H., 1990. Lunar anorthosites and the magma – ocean plagioclaseflotation hypothesis: Importance of FeO enrichment in the parent magma. *American Mineralogist*, 75, 46–58.

Watters, T. R., et al., 2010. Evidence of recent thrust faulting on the Moon revealed by the Lunar Recon-naissance Orbiter Camera. *Science*, 329, 936 - 940.

Weber, R. C., Lin, P., Garnero, E. J., Williams, Q., Lognonné, P., 2011. Seismic detection of the lunar core. *Science*, 331, 6015, 309-312.

Whitten, J., et al., 2011. Lunar mare deposits associated with the Orientale impact basin: New insights into mineralogy, history, mode of emplacement, and relation to Orientale Basin evolution from Moon Mineralogy Mapper (M^3) data from Chandrayaan-1. *Journal of Geophysical Research*, 116, E00G09, doi: 10.1029/2010JE003736.

Wieczorek, M. A., et al., 2006. The constitution and structure of the lunar interior. *Reviews in Mineralogy & Geochemistry*, 60, 221–364.

Wieczorek, M. A., et al., 2013. The crust of the Moon as seen by GRAIL. *Science*, 339, 6120, 671-675.

Weitz, C. M., Head III, J. W., Pieters, C. M., 1998. Lunar Regional Dark Mantle Deposits: Geologic, Multispectral, and Modeling Studies. *Journal of Geophysical Research*, 103, 22725-22759.

Wilhelms, D. E., 1987. The Geologic History of the Moon. *U.S. Geological Survey Professional Paper*, 1348. p. 302.

Wood, C. A., 1978. Lunar concentric craters. In: *Proceedings of 9th Lunar and Planetary Science Conference*, 1264-1266.

Wood, J. A., Dickey, J. S., Marvin, U. B., Powell, B. N., 1970. Lunar anorthosites and a geophysical model of the moon. In: *Proceedings of Apollo 11 Lunar Science Conference*, 1, 965–988.

Yamamoto, S., et al., 2010. Possible mantle origin of olivine around lunar impact basins by SELENE, *Nature Geosciences*, 3, 533-536, doi: 10.1038/NGEO897

Yamamoto, S., et al., 2013. Global Distribution of Mg-Spinel on the Moon Revealed by SELENE Spectr-al Profiler. In: *Proceedings of 44th Lunar and Planetary Science Conference*, Abstract #1768.

Zhang, J., Dauphas, N., Davis, A. M., Leya, I., Fedkin, A., 2012. The Proto-Earth as a significant source of Lunar Material. *Nature Geoscience*, 5, 4, 251-255, doi:10.1038/ngeo1429.

Ziethe, R., Seiferlin, K., Hiesinger, H., 2009. Duration and extent of lunar volcanism: Comparison of 3D convection models to mare basalt ages. *Planetary and Space Science*, 57, 784–796.

Website Links

http://www.isro.org/chandrayaan/htmls/mmm_nasa.htm
http://lroc.sese.asu.edu/data/LRO-L-LROC-2-EDR-V1.0/LROLRC_0001/DOCUMENT/LROCSIS.PDF
http://lroc.sese.asu.edu/news/index.php?/archives/790-A-Unique-View-Of-The-Moon.html
http://lroc.sese.asu.edu/news/?archives/341-Nearside-Spectacular!.html
http://sservi.nasa.gov/articles/cygames-selene-ii-a-lunar-construction-game/
http://i.ytimg.com/vi/Jf628Bugy_I/0.jpg
http://www.nasa.gov/mission_pages/LRO/news/vid-tour.html
http://thegalaxytoday.com/wp-content/uploads/2013/12/image-9-300x225.jp
http://thegalaxytoday.com/2013/12/the-first-500-million-years-violence-chaos-and-then-life/
http://www.thelivingmoon.com/43ancients/02files/Moon_Images.html
http://wms.lroc.asu.edu/lroc_browse/view/orientale
http://spaceguard.rm.iasf.cnr.it/NScience/neo/neo-when/crt-char.html
http://phys.org/news/2013-03-lunar-impacts-seas-molten.html
http://nssdc.gsfc.nasa.gov/nmc/spacecraftDisplay.do?id=2007-039A
http://www.brahmand.com/news/Chandrayaan-2-will-be-Indo-Russia-mission-ISRO-lab-director/10624/1/10.html
http://nssdc.gsfc.nasa.gov/nmc/spacecraftDisplay.do?id=2009-031A
http://www.geospatialworld.net/Paper/Cover-Stories/ArticleView.aspx?aid=21846
http://www.exelisvis.com/docs/MinimumNoiseFractionTransform.html
http://www.bbc.com/news/science-environment-19992233
http://www.kaguya.jaxa.jp/en/equipment/tc_e.html